

Development of a Quantitative Ultrasound Method for the
Assessment of Cortical Bone Properties using low frequencies
Ultrasonic Guided Waves

by

Daniel PEREIRA

MANUSCRIPT-BASED THESIS PRESENTED TO ÉCOLE DE
TECHNOLOGIE SUPÉRIEURE
IN PARTIAL FULFILLMENT FOR THE DEGREE OF
DOCTOR OF PHILOSOPHY
Ph.D.

MONTREAL, JANUARY 25, 2019

ÉCOLE DE TECHNOLOGIE SUPÉRIEURE
UNIVERSITÉ DU QUÉBEC



Daniel Pereira, 2019



This Creative Commons license allows readers to download this work and share it with others as long as the author is credited. The content of this work cannot be modified in any way or used commercially.

BOARD OF EXAMINERS

THIS THESIS HAS BEEN EVALUATED

BY THE FOLLOWING BOARD OF EXAMINERS

Mr. Pierre Belanger, Thesis Supervisor
Department of Mechanical Engineering, École de Technologie Supérieure

Mr. Julio Fernandes, Co-supervisor
Department of Surgery, Université de Montréal

Mrs. Catherine Laporte, President of the Board of Examiners
Department of Electrical Engineering, École de Technologie Supérieure

Mr. Yvan Petit, Member of the jury
Department of Mechanical Engineering, École de Technologie Supérieure

Mr. Jean Provost, External Independent Examiner
Department of Engineering Physics, École Polytechnique de Montréal

THIS THESIS WAS PRESENTED AND DEFENDED

IN THE PRESENCE OF A BOARD OF EXAMINERS AND THE PUBLIC

ON DECEMBER 18, 2018

AT ÉCOLE DE TECHNOLOGIE SUPÉRIEURE

FOREWORD

This Ph.D. thesis contains my research work carried out between 2014 and 2018 at École de Technologie Supérieure and Centre de recherche l'Hôpital du Sacré-Coeur, under the supervision of professor Pierre Belanger and co-supervision of Dr. Julio Fernandes. This work was inspired by the desire of collaborating along with an entire research community on the establishment of a new ultrasound technology which I believe has the potential to improve the quality of people's life in the near future. Spending most of the research time at l'Hôpital du Sacré-Coeur de Montréal has provided me with a positive and enriching experience as a professional but also as a human being. Therefore, I would like to thank life for having this opportunity.

ACKNOWLEDGEMENTS

I would like to express my sincere gratitude to Prof. Pierre Belanger and Dr. Julio Fernandes for supervising my work over four years. Special thanks to my previous supervisor back in Brazil, Prof. Thomas Clarke, who trusted my job so that this opportunity would be given to me.

I would like to thank my fellow from PULETS for their feedback, cooperation and friendship. I would particularly like to thank the feedback offered by Guillaume Boivin and Lúcio Corrêa which have helped me in overcoming numerous obstacles I have been facing through my research. In addition I would like to express my gratitude to all the LIO members for providing a very welcoming work atmosphere at the hospital.

I am deeply grateful to my friends and roommates who have always been a major source of support when things would get a bit discouraging. Thanks to all my friends in Canada, special thanks to Olivia Lucarelli and Iara Binta Lima Machado.

Most of all, thanks to my family: my parents and to my brother and his wife who brought me peace, made me smile, and gave me strength all the way through. This work is dedicated to my nephew Luca who brought the spirituality that I need to overcome the most difficult part of this journey.

This work was developed in collaboration with the Centre de recherche l'Hôpital du Sacré-Coeur de Montréal and École de technologie supérieure. I would like to express my gratitude for the grant received from the Fonds d'Internationalisation de la Recherche (FIR) of École de technologie supérieure.

Élaboration d'une méthode quantitative d'évaluation des propriétés de l'os cortical au moyen d'ondes guidées ultrasonores basse fréquences

Daniel PEREIRA

RÉSUMÉ

L'ostéoporose est associée à une réduction de la masse osseuse ainsi qu'à une détérioration osseuse microarchitecturale, entraînant une réduction de la qualité de l'os et une augmentation du risque de fracture. La fracture du radius est l'une des fractures ostéoporotiques les plus fréquentes et peut être considérée comme un site important pour le dépistage précoce de l'ostéoporose et pour la prévention de fractures futures, telles qu'une fracture de la hanche ou de la colonne vertébrale. Dans ce contexte, la technique de transmission axiale utilisant des ondes guidées ultrasonores a été développée pour évaluer la qualité des os dans les os longs tel que le radius. La méthode peut aller au-delà d'une simple estimation de la densité minérale osseuse généralement obtenue avec l'absorptiométrie biphotonique à rayons X (DEXA), cette donnée n'étant pas suffisante pour évaluer le risque de fracture. Les ondes guidées ultrasonores ont le potentiel d'interroger à la fois les propriétés mécaniques et géométriques de l'os cortical. À basses fréquences, la sensibilité aux variations de propriétés de l'os intracortical est améliorée en raison de la profondeur de pénétration accrue obtenue par les différents modes d'ondes guidées. Ceci est particulièrement pertinent afin d'évaluer les stades précoces de l'ostéoporose puisque l'initiation de celle-ci est associée à la résorption endostéale. Par conséquent, les ondes guidées ultrasonores à basse fréquences sont prometteuses en tant que méthode de dépistage rapide, sûre et portable pour l'évaluation de l'ostéoporose précoce en soins primaires. Ainsi, le but de ce projet est de mieux comprendre l'interaction physique entre les ondes guidées ultrasonores à basse fréquences et la structure de l'os cortical. Pour ce faire, un modèle de l'os cortical complet, et efficace en termes de calcul, a été mis en œuvre à l'aide de la méthode des éléments finis semi-analytiques. (SAFE). La méthode permet la simulation d'ondes guidées ultrasonores dans une coupe transversale d'os multicouches, irrégulières, et hétérogènes modélisée au moyen de matériaux anisotropes et viscoélastiques. Le modèle a été appliqué dans le contexte de la transmission axiale pour étudier l'effet des propriétés des os intracorticaux sur la propagation des ultrasons à basse fréquence. Les résultats ont permis d'identifier une configuration de sonde appropriée ainsi qu'une stratégie robuste de traitement du signal permettant d'extraire des caractéristiques significatives des modes ultrasonores. Basé sur ces informations, un prototype de configuration à transmission axiale a été réalisé afin d'évaluer la performance de la méthode sur cinq échantillons de radius *ex-vivo*. Pour ce faire, un modèle SAFE paramétré similaire à un os a été mis en œuvre dans une routine d'optimisation automatique permettant d'inverser le modèle et déterminer les différentes propriétés de l'os cortical. La configuration par transmission axiale à basse fréquence proposée a permis de récupérer des données fiables d'épaisseur et de densité sur les radius testés ainsi que des données géométriques supplémentaires associées à la forme corticale des échantillons. Les propriétés ainsi prédites sont associées à un volume cortical beaucoup plus grand en comparaison à la méthode d'inversion conventionnelle utilisant des fréquences plus élevées. La méthode inverse proposée a le potentiel d'augmenter la détectabilité des stades précoces de l'ostéoporose, ainsi que d'améliorer

l'évaluation du risque de fracture. Les résultats disponibles peuvent maintenant être utilisés pour définir les paramètres et l'instrumentation d'une étude clinique pilote sur la détection de l'ostéoporose.

Mots-clés: Ostéoporose, Technique de transmission axiale, Ondes guidées ultrasonores, Basse fréquence, Os cortical, Os endostéale, Méthode des éléments finis semi-analytiques, Problème d'inversion

Development of a Quantitative Ultrasound Method for the Assessment of Cortical Bone Properties using Low-Frequency Ultrasonic Guided Waves

Daniel PEREIRA

ABSTRACT

Osteoporosis is associated with a reduction of the bone mass and microarchitectural bone deterioration, leading to a reduction in bone quality and to an increase in fracture risk. The radius fracture is one of the most frequent osteoporotic fractures and can be considered an important site for the early detection of osteoporosis and to prevent future fractures, such as hip and spine fractures. In this context, the axial transmission technique using ultrasonic guided waves was developed to assess bone quality in long bones such as the radius. The method can go beyond a simple estimation of the bone mineral density typically achieved with dual-energy x-ray absorptiometry (DEXA), which is not sufficient to assess fracture risk. Ultrasonic guided waves have the potential to interrogate both the mechanical and geometrical properties of cortical bone. When operating at low frequencies, the sensitivity to variations in intracortical bone properties is improved due to the great penetration depth achieved by the ultrasonic guided wave modes. This is particularly relevant to assess early stages of osteoporosis since early osteoporosis is known to be associated with endosteal resorption. Therefore, low-frequency ultrasonic guided waves hold promises as a rapid, safe and portable screening method for assessment of early osteoporosis in a primary care level. Thus, the purpose of this project is to bring a better understanding of the physical interaction between low-frequency ultrasonic guided waves and the cortical bone structure. In order to do so, a comprehensive and computationally efficient cortical bone model was implemented using the semi-analytical finite element (SAFE) method. The method allows the simulation of ultrasonic guided waves in an irregular, multi-layer and heterogeneous bone cross-section modeled with anisotropic and viscoelastic material properties. The model was applied in the context of axial transmission to investigate the effect of intracortical bone properties on the propagation of low-frequency ultrasonic guided wave modes. The results allowed the identification of a suitable probe configuration as well as a robust signal processing strategy to extract significant mode features from ultrasonic responses. With this information, a prototypical axial transmission configuration was built so that the performance of the method could be evaluated on five *ex-vivo* radius samples. To do so, a parametrized bone-like SAFE model was implemented into an autonomous model-based optimization routine to perform the inverse determination of different cortical bone properties. The proposed low-frequency axial transmission configuration was able to retrieve reliable thickness and density values for radius specimens as well as provided additional geometrical information associated with the cortical shape of the samples. The predicted properties found were associated to a much larger cortical volume when compared to the conventional inversion techniques using higher frequency. The proposed inverse method has the potential to increase the detectability of early stages of osteoporosis as well as improve the assessment of risk of fracture. The results available can be now used to define the parameters and instrumentation of a pilot clinical study on the detection of osteoporosis.

Keywords: Osteoporosis, Axial Transmission Technique, Ultrasonic Guided Waves, Low-Frequency, Cortical Bone, Endosteal Bone, Semi-Analytical Finite-Element Method, Inversion Problem

TABLE OF CONTENTS

	Page
INTRODUCTION	1
0.1 Objective	4
CHAPTER 1 LITERATURE REVIEW	7
1.1 Osteoporosis	7
1.1.1 Osteoporotic fractures	7
1.1.2 Radius fracture	8
1.2 X-ray-based techniques for the assessment of osteoporosis	9
1.2.1 Dual-energy x-ray absorptiometry (DEXA)	9
1.2.2 Quantitative computed tomography (QCT)	9
1.2.3 High-resolution peripheral quantitative computed tomography (HR-pQCT)	10
1.3 Quantitative ultrasound (QUS) for the assessment of osteoporosis	10
1.3.1 Through-transmission technique	11
1.3.2 Axial transmission technique	11
1.3.3 Axial transmission using ultrasonic guided waves	12
1.4 Ultrasonic guided waves	13
1.4.1 Ultrasonic guided waves in cylindrical waveguides	13
1.4.1.1 Dispersion curves	15
1.4.1.2 Mode shape	17
1.4.1.3 Modal excitability	18
1.4.2 Semi-analytical finite-elements method (SAFE)	21
1.4.2.1 SAFE in solid waveguide	22
1.5 Chronological arrangement of the manuscripts	23
CHAPTER 2 SIMULATION OF ACOUSTIC GUIDED WAVE PROPAGATION IN CORTICAL BONE USING A SEMI-ANALYTICAL FINITE ELEMENT METHOD	27
2.1 Introduction	28
2.2 Acoustical modeling of wave propagation	30
2.2.1 Semi-analytical finite element method	30
2.2.1.1 Formulation of the semi-analytical finite elements	31
2.2.1.2 Simulation of time domain signal	32
2.2.2 Finite element method	33
2.3 Application to cortical bone	34
2.3.1 Axial transmission configuration	35
2.3.2 Modeling cortical bone	36
2.3.2.1 Cortical bone waveguide	36
2.3.2.2 Heterogeneous distribution of bone properties	37
2.4 Results and discussion	41

2.4.1	Validation of SAFE simulations	41
2.4.2	Dispersion curves of cortical bone	42
2.4.3	Effect of properties on the FAS velocity	44
2.4.4	Limitations of the study	48
2.5	Conclusion	49
CHAPTER 3	EFFECT OF INTRACORTICAL BONE PROPERTIES ON THE PHASE VELOCITY AND CUT-OFF FREQUENCY OF LOW- FREQUENCY GUIDED WAVE MODES (20-85 KHZ)	51
3.1	Introduction	52
3.2	Material and methods	56
3.2.1	Simulating time domain signals	56
3.2.2	Axial transmission configuration	58
3.2.3	Modeling cortical bone	61
3.2.4	Heterogeneous distribution of bone properties	63
3.3	Results and discussion	65
3.3.1	Effect of excitation position	65
3.3.2	Effect of physiopathological conditions	67
3.3.3	Effect of stiffness coefficients and density	69
3.4	Conclusion	69
CHAPTER 4	EX-VIVO ASSESSMENT OF CORTICAL BONE PROPERTIES USING LOW-FREQUENCY ULTRASONIC GUIDED WAVES (<60 KHZ)	73
4.1	Introduction	74
4.2	Material and Methods	77
4.2.1	Experimental measurements	77
4.2.1.1	Ex-vivo samples and reference values	77
4.2.1.2	Axial transmission measurements	79
4.2.2	Forward model	80
4.2.2.1	Semi-analytical finite-element method	80
4.2.2.2	Bone-like model	82
4.2.3	Inversion problem	83
4.2.3.1	Cost function	84
4.2.3.2	Automatic parameter identification	86
4.3	Results and Discussion	87
4.3.1	Dispersion curves fitting	87
4.3.2	Estimated density	90
4.3.3	Estimated thickness	92
4.3.4	Estimated bone-like shape	93
4.4	Conclusions	95
4.5	Originality of the proposed work	96
CONCLUSION AND RECOMMENDATIONS		97

APPENDIX I	AXIAL TRANSMISSION ASSESSMENT OF TRABECULAR BONE AT DISTAL RADIUS USING GUIDED WAVES	101
APPENDIX II	INVERSE CHARACTERIZATION OF ADHESIVE SHEAR MODULUS IN BONDED STIFFENERS USING ULTRASONIC GUIDED WAVES	109
BIBLIOGRAPHY	119

LIST OF TABLES

		Page
Table 1.1	The geometry parameters and material properties of the hollow cylinder.....	16
Table 1.2	Summary of displacement features of each family of mode in a bi-layer cylinder system.	18
Table 2.1	Summary of the properties used to model cortical bone. The real part of the stiffness coefficients was adapted from the experimental results obtained by (Sansalone <i>et al.</i> , 2010). The imaginary part was adapted from the results used by (Naili <i>et al.</i> , 2010), applying equation 2.9.....	40
Table 3.1	Summary of the properties used to model cortical bone. The real parts of the stiffness coefficients were adapted from the experimental results obtained by Sansalone <i>et al.</i> (2010), while the imaginary parts were adapted from the results presented by Naili <i>et al.</i> (2010), using equation 3.7.	62
Table 3.2	Total variation of the phase velocity V_{ph} and cut-off frequency $F_{cut-off}$ for the excitations performed at position "A", "C" and "H".	67
Table 3.3	Percentage variation computed for V_{ph} and $F_{cut-off}$ for each viscoelastic coefficient and density separately.....	70
Table 4.1	Bounds of the model parameters and their respective discretization used to perform the automatic parameter identification.	87

LIST OF FIGURES

		Page
Figure 1.1	Cylindrical coordinates used to represent the bone system	14
Figure 1.2	Displacement field in the radial direction for longitudinal (a) and flexural modes (b-d) for a hollow steel cylinder at frequency of 100 kHz.....	16
Figure 1.3	Phase velocity dispersion curves of ultrasonic guided wave modes in a hollow cylinder in vacuum. The dispersion curves were obtained using the methodology presented in the section 1.4.2.....	17
Figure 1.4	Radial displacement variation with the frequency for L(0,1) mode shape in a bi-layer cylinder. The displacement fields were obtained using the methodology presented in the section 1.4.2	18
Figure 1.5	Displacement along the radial line according to the mode family for: a) radial displacement, b) axial displacement and c) angular displacement. The displacement along the radial line were taken from the displacement field obtained using the methodology presented in the section 1.4.2.....	19
Figure 1.6	Plate analogy of circular Lamb waves and shear horizontal waves generated by out-of-plane and in-plane point excitation in a cylinder.	20
Figure 1.7	SAFE representation system; a) meshed arbitrary cross-section waveguide; b) representation of a waveguide in a multi-layer system (built using COMSOL Multiphysics Graphic User Interface).	22
Figure 2.1	Schematic of the equivalent 3D axial transmission configuration used to perform the SAFE simulations.....	34
Figure 2.2	Cross-section taken from the middle of the radius bone and used for the SAFE analysis. Different regions were defined along the radial direction: periosteal (A-B), middle (B-C) and endosteal (D-E) regions.....	38
Figure 2.3	a) Original and simplified distribution of C_{11} varying from the periosteum to endosteum b) Elastic coefficients and density varying with the distance from the periosteum.	39

Figure 2.4	Nine different heterogeneous distributions defined between the "Healthy" and "Osteoporotic" conditions.	40
Figure 2.5	Time-domain signal obtained at 150 mm of propagation distance using: a) FE simulations; b) SAFE simulations showing the signal containing all modes; c) SAFE simulations showing the signal of each mode separately.....	42
Figure 2.6	Time-domain signal obtained at 150 mm of propagation distance using: a) FE simulations; b) SAFE simulations showing the signal containing all modes; c) SAFE simulations showing the signal of each mode separately.....	42
Figure 2.7	Phase velocity dispersion curves of the simulated modes obtained with "Healthy" and "Osteoporotic" waveguide condition.....	43
Figure 2.8	Dispersion curves obtained for the "Healthy" condition a) Group velocity superposed with the frequency bandwidth of the input signal; b) Attenuation; c) Out-of-plane excitability; d) Time-domain signal obtained for the SAFE simulation, showing each mode separately and all modes together for the "Healthy" condition. The legend in Figure 2.8d is applied to Figure 2.8a, 2.8b, and 2.8c.....	45
Figure 2.9	FAS velocity obtained using the combinations of different modes.	46
Figure 2.10	a) Amplitude contribution of the four main modes separately, varying with the scenarios; b) Group velocity of each of the four modes separately and FAS velocity (simulated considering four of the modes) varying with the scenarios. The circles show the change of the mode with the highest amplitude contribution (from $m=1$ to $m=4$).	47
Figure 3.1	Schematic of the equivalent 3D axial transmission configuration used to perform the SAFE simulations.....	58
Figure 3.2	Cross-section of the middle of the radius bone used for the SAFE analysis. Different regions were defined along the radial direction: periosteal (a-b), middle (b-c) and endosteal (d-e) regions. The letters "A" to "H" show the eight different positions used to perform the excitation on the bone surface.	60
Figure 3.3	a) Simulated time domain signals obtained at each receiving position. b) Typical phase velocity vs. frequency diagram showing the intensity of the excited modes (dB scale) and the measured	

	phase velocity V_{ph} and cut-off frequency $F_{cut-off}$. The white ellipses show the two excited regions in the diagram.	61
Figure 3.4	Simplified distribution of the elastic coefficients C_{11} varying with the distance from the periosteum for the healthy and osteoporotic condition.	64
Figure 3.5	Normalized modal excitability obtained for the excitation performed at eight different positions on the bone surface from 10 kHz to 100 kHz. The letters a) to h) are associated to the excitation position "A" to "H" shown in Figure 2, respectively.	66
Figure 3.6	Out-of-plane displacement field (radial direction r in Figure 3.1) at 40 kHz for: a) fundamental flexural mode F(1,1) on a tubular geometry waveguide and b) mode $m=1$ on a bone-like geometry waveguide. The highlighted regions denote modes segments that have an excitability 10 dB higher than the other modes.	66
Figure 3.7	Power flow in the endosteal region normalized by the total power flow for modes $m=1$, $m=2$, $m=3$, $m=4$, and $m=5$ from 20 kHz to 100 kHz.	68
Figure 4.1	Computed tomography (CT) image taken at the middle 1/3 radius, with the white solid lines showing the ROI of the axial transmission measurements.	78
Figure 4.2	Axial transmission configuration used to perform the measurements on the radius specimens, with the black dashed lines showing the ROI.	79
Figure 4.3	Forward model showing the bone-like geometry described in terms of thickness and outer diameter variables.	81
Figure 4.4	Typical wavenumber-frequency-excitability diagram computed by the forward model using the SAFE method. The color-map shows the excitability of each mode.	83
Figure 4.5	Effective transversally isotropic elastic properties of cortical bone varying with bulk density. The properties were obtained using an anisotropic homogenization theory introduced by Vu & Nguyen-Sy (2018).	84
Figure 4.6	a) Typical solutions of the SAFE model (circles) overlaid onto experimental dispersion curves for frequencies between 5 and 60 kHz. The circles were filled with colors defined based on the	

	modal excitability computed using equation (4.3); b) Amplitude extracted from experimental dispersion curves at 55 kHz along with simulated modes computed with the SAFE model and their respective excitabilities.	85
Figure 4.7	Optimal matching between the experimental dispersion curves and the simulated modes for: a) Sample # 1; b) Sample # 2; c) Sample # 3; d) Sample # 4, and e) Sample # 5.	88
Figure 4.8	Normalized cost function obtained for the first acquisition by sweeping density and thickness while keeping outer diameter and shape factor with the optimal values on: a) Sample # 1; b) Sample # 2; c) Sample # 3; d) Sample # 4, and e) Sample # 5.....	90
Figure 4.9	Normalized cost function grid obtained on: a) Sample # 5, second acquisition and b) Sample # 5, third acquisition.....	91
Figure 4.10	Mean and standard deviation obtained for density (red circles), varying from samples # 1 to # 5, along with the reference average voxel values measured from the CT images (black solid lines).....	92
Figure 4.11	Mean and standard deviation obtained for thickness (red circles) varying from sample # 1 to # 5 along with the reference values measured from the CT images (black solid lines).	93
Figure 4.12	Estimated bone-like shape (white dotted lines), along with cross-sectional CT slice taken from the middle of the VOI for: a) Sample # 1; b) Sample # 2; c) Sample # 3; d) Sample # 4, and e) Sample # 5.....	94

LIST OF ABBREVIATIONS

FIR	Fonds d'Internationalisation de la Recherche
DEXA	Dual-Energy X-ray Absorptiometry
SAFE	Semi-Analytical Finite Element
QUS	Quantitative Ultrasound
FAS	First Arrival Signal
2D	Two Dimensional
FFT	Fast Fourier Transform
CT	Computed Tomography
WHO	World Health Organization
BMD	Bone Mineral Density
QTC	Quantitative Computed Tomography
HR-pQCT	High Resolution Peripheral Quantitative Computed Tomography
TOF	Time of Flight
NDT	Non-Destructive Testing
μ CT	Micro Computed Tomography
3D	Three Dimensional
FEM	Finite Element Method
CAD	Computer Aided Design
ROI	Region of Interest

VOI	Volume of Interest
S-SVD	Sparse Singular Value Decomposition
GA	Genetic Algorithm
JASA	Journal of Acoustical Society of America

LISTE OF SYMBOLS AND UNITS OF MEASUREMENTS

kHz	Kilohertz
m	Meter
λ	Wavelength
V_{ph}	Phase velocity
V_{gr}	Group Velocity
k	Wavenumber
ω	Angular frequency
ϑ	Mode order
T	Period
kg	Kilogram
mm	Milimeter
GPa	Giga pascal
i	Imaginary number
P	Powerflow
E	Excitability
q	Tangential direction
r	Radial direction
z	Axial direction
ϕ	Angular position with respect to the applied force

δ	Derivative term
ρ	Density
$H_0^{(1)}$	First Hankel function of order zero
F	Frequency spectrum
Pa	Pascal
BV	Bone volume
TV	Total volume
A^m	Relative amplitude contribution of each mode
m	Mode number
a^m	Envelope amplitude of the m -th mode
η_c^*	Viscoelastic coefficients
C_c^*	Stiffness coefficients
f	Frequency
t	Time
Gb	Gigabyte
h	Envelope amplitude of the m -th mode
$F_{cut-off}$	Cut-off frequency
dB	Decibel
MPa	Mega pascal
TH	Predicted thickness

OD	Outer diameter
SF	Shape factor
<i>th</i>	Local thickness

INTRODUCTION

Osteoporosis is defined as a disease characterized by a reduction of bone mass and microarchitectural bone deterioration, leading to a severe reduction of the bone strength and, consequently, increasing significantly the risk of future fractures even for low energy traumas (Con, 1991). Despite the financial burden for the government and the high impact of those fractures on the quality of life of the patients, a deficiency in the management of the diagnosis and the treatment of osteoporosis can be found in Canada (Papaioannou *et al.*, 2004) and in different countries around the world (Strom *et al.*, 2011; Giangregorio *et al.*, 2006; Dempster, 2011). In this context, the radius fracture is the most frequent osteoporotic fracture in elderly patients, and several studies showed that radius fractures can be used as a predictor of future fracture at important sites of the body, such as hip and spine (Padegimas & Osei, 2013; Rozental *et al.*, 2013; Muller *et al.*, 2003). Thus, the early identification and treatment of fragility fractures on the radius is a great opportunity to prevent future fractures, and reducing all associated costs.

One particular topic of much interest to the biomedical engineering community is the possibility of using quantitative ultrasound (QUS) to detect and monitor the bone condition. A cost-effective and non-hazardous in-situ system that can be used to obtain the properties of the radius in a non-invasive manner is much desirable in this context. For osteoporosis detection, ultrasonic guided waves have the potential to offer a more complete characterization of the bone properties than the established method of bone densitometry; the Dual-Energy X-ray Absorptiometry (DEXA). DEXA can only provide limited information on the mineralization and geometry of bones whereas QUS would also be sensitive to elastic properties and the presence of defective bone structural features. Moreover, the cost of DEXA in developing countries is prohibitive. Thus, there is much interest in alternative QUS techniques, which will have the advantage of not exposing the patient to ionizing radiation, will be feasible in a primary care setting and for which the equipment will be affordable relative to DEXA.

Bone QUS was initially developed in the context of trabecular bone characterization using transverse transmission devices (Kaufman & Einhorn, 1993). However, the investigation of cortical bone (Rico, 1997) has attracted significant interest since about 80% of the skeleton is made of cortical bone, which supports most of the body load, and is involved in osteoporotic fractures (DG *et al.*, 1991). Cortical bones, such as the radius or the tibia, constitute suitable waveguides for the propagation of ultrasonic guided waves, as shown in various studies, including for instance (Haba *et al.*, 2016; Gluer, 2008, 1997).

The endosteal resorption of cortical bone results in a deterioration of material properties and in a reduction of the cortical bone thickness (Ritzel *et al.*, 1997). Low frequencies (typically below 200 kHz) axial transmission research demonstrated that ultrasonic guided waves are sensitive to mechanical and geometrical variations in the cortical layer (Yeh & Yang, 2011; Rozental *et al.*, 2013; Muller *et al.*, 2005). Operating at low frequencies offers the advantage of a lower attenuation as well as a reduced number of generated modes, which simplifies the signal analysis. In addition, low frequency guided wave modes tend to achieve greater penetration depths (when compared to high-frequency) due to its attenuation characteristics. As a consequence, the sensitivity to variations in intracortical bone properties, which is relevant to assess early stages of osteoporosis, could be improved when using low-frequencies.

The determination of cortical bone properties using ultrasonic guided waves commonly involves the challenge of solving multi-parametric inverse problems. Current multi-mode characterization methods lie in inversion schemes used to match experimental data with the simulated modes obtained from plate and cylinder models (as an approximation of the actual bone geometry) (Minonzio *et al.*, 2015; Xu *et al.*, 2016; Kilappa *et al.*, 2015). Recently, more comprehensive numerical approaches are being increasingly explored aimed at improving the realism of cortical bone models (Bossy *et al.*, 2004; Haiat *et al.*, 2011; Chen & Su, 2014; Moreau *et al.*, 2014). Despite the improvements achieved so far, the physical interaction between low

frequencies guided waves and the cortical bone structure remains unexplored. In this context, the semi-analytical finite-element (SAFE) method has been successfully implemented for modeling waveguides with arbitrary cross-section geometry (Thakare *et al.*, 2017; Nguyen *et al.*, 2017; Tran *et al.*, 2015). The method enables the implementation of multi-layer heterogeneous and viscoelastic materials (Bartoli *et al.*, 2006). All these features combined make the method suitable to model bone as a waveguide in an effective way. However, the method has not been thoroughly explored yet, being mostly used to model plate or cylinder cross-sectional geometries and using homogeneous materials properties. The implementation of a complex geometry along with a heterogeneous distribution of material properties has never been investigated in the literature for bone application. The capability of modeling different features is particularly interesting at low-frequencies, where the cross-sectional curvature of the cortical bone and its particular shape play an important role in the propagation of the excited guided wave modes.

Thus, the core of this thesis lies in the implementation of a more comprehensive but computationally efficient cortical bone model using the SAFE method. A cortical bone model with an irregular, heterogeneous and multi-layered cross-section and using transversally isotropic viscoelastic material properties was implemented. The model was used to study the ultrasonic guided waves propagating in the cortical bone system in different ways. The model was first applied in the context of an axial transmission configuration in order to investigate the feasibility of first arrival signal (FAS) velocity at low frequencies. The FAS velocity is the most commonly used method to evaluate bone quality *in-vivo* and its feasibility at low frequencies has not been completely investigated yet. The obtained FAS velocity was shown to be associated with the velocity of the modes with high excitability. However, due to the interaction between several high excitability modes around the FAS, the FAS velocity was shown to be a poor discriminator of cortical bone properties at low frequencies. To address this limitation, the same SAFE model was used to simulate a multi-element axial transmission configuration, while using a two-dimensional spatio-temporal Fourier transform (2D-FFT) instead of the FAS

velocity. More specifically, the effect of intracortical bone properties on the phase velocity and cut-off frequency of low frequencies ultrasonic guided wave modes was investigated at frequencies between 20 kHz and 85 kHz. The results obtained lead to a more comprehensive understanding of the physical interaction between the cortical bone curvature and the excitability of low frequencies ultrasonic guided wave modes. By selecting an adequate frequency and position of excitation, the proposed axial transmission configuration was found to be very promising in assessing cortical bone properties at low frequencies. Hence, this configuration was then used to perform measurement on five *ex-vivo* radius samples at frequencies between 5 kHz and 60 kHz. From the measured data, the dispersion curves of the propagating modes was computed using a 2D-FFT and systematically compared to the simulated modes obtained with the SAFE model. More specifically, a parameterized bone-like model was implemented to perform the inverse characterization of the cortical bone properties in the middle 1/3 diaphysis. The inversion scheme was able to estimate equivalent bone conditions associated to larger cortical volume, showing remarkable agreement with the values observed in computed tomography (CT) images. Furthermore, the method retrieved additional information associated to the geometrical shape, which may be useful to improve the assessment of the risk of fracture of the cortical bone.

0.1 Objective

The purpose of this thesis is to develop an ultrasonic guided wave method for the assessment of cortical properties at low frequency aiming at early detection of osteoporosis. In order to achieve this goal, the following specific objectives were defined:

- I. Implement a comprehensive and computationally efficient cortical bone model that allows different geometrical features as well as anisotropic and viscoelastic material properties.

- II. Perform a simulation study to identify the most promising axial transmission configuration as well as a suitable signal processing strategy to retrieve reliable cortical bone properties at low frequencies.
- III. Implement an autonomous model-based optimization routine to perform the inverse characterization of the cortical bone properties.
- IV. Investigate the potential of the axial transmission configuration and validate the performance of the inverse method by performing measurements on *ex-vivo* radiuses samples.

CHAPTER 1

LITERATURE REVIEW

1.1 Osteoporosis

According to the World Health Organization (WHO) (WHO, 1994), osteoporosis can be defined as “a disease characterized by low bone mass, microarchitectural deterioration of bone tissue leading to enhanced bone fragility, and a consequent increase in fracture risk”. In Canada (2008), the Public Health Agency estimated that osteoporosis was diagnosed in approximately 1.5 million Canadians aged 40 years and over, mostly in women (80%) (Government of Canada, 2010). Although osteoporosis can be considered more frequent among older women, it can affect individuals of all ages and both sexes (Kanis, 1994; MacLaughlin *et al.*, 2006). Moreover, the symptoms of the disease are rarely detected until the first fracture occurs, making early diagnosis and treatment challenging. In fact, osteoporosis can be considered the most common bone disease, and the tendency for it is to become even more common in the future due to the aging of the population (Hernlund *et al.*, 2013; Rachner *et al.*, 2011).

1.1.1 Osteoporotic fractures

The main consequence of osteoporosis is the severe reduction of bone strength, which significantly increases the risk of future fractures even for low energy traumas (Kanis, 1994). The wrist, shoulder, spine and hip are the most common fracture sites and depending on their severity, fractures can lead to several complications such as hospitalization, disability, and in some cases, premature death (Ioannidis *et al.*, 2013). A Canadian population study (Tarride *et al.*, 2012) documented that during the fiscal year 2007/2008, 57,413 hospitalizations and 832,594 hospitalization days were registered due to osteoporosis fractures, accounting for a direct cost of \$1.2 billion for the Canadian government. The study also documented the total cost of \$2.3 billion and \$3.9 billion, when indirect costs and long-term care costs were respectively taken into account. In addition, osteoporosis was shown to cause a similar impact on the quality of

life compared to other chronic diseases, such as arthritis, pulmonary disease, diabetes mellitus and heart disease (Sawka *et al.*, 2005). Despite its economic burden and high impact on quality of life, a clear deficiency in management of diagnosis and treatment of osteoporosis can be found in Canada (Papaioannou *et al.*, 2004) and in different countries around the world (Strom *et al.*, 2011; Giangregorio *et al.*, 2006; Dempster, 2011). According to a prospective study (Bessette *et al.*, 2008), less than 16% of those who suffered a fragility fracture received treatment in a period of six to eight months following the fracture, and only 21% of them received an osteoporosis test during the same period. Since the risk of fracture can be considered higher after a previous fragility fracture (Sajjan *et al.*, 2012; Eisman *et al.*, 2012; Gehlbach *et al.*, 2012), the rates of future fractures and all related costs can be significantly reduced through the adequate identification and treatment of the first fracture.

1.1.2 Radius fracture

The distal radius fracture can be considered the most frequent osteoporotic fracture in elderly patients. In Canada in 2008 (Tarride *et al.*, 2012), wrist fractures were responsible for 25% of emergency room visits related to osteoporotic fractures, while hip and vertebral fractures accounted for 23% and 5%, respectively. In the same year, wrist fractures represented only 9% of the total care cost, while hip fractures accounted for 53%. For that reason, hip fractures have so far received more attention from the government and research communities.

In fact, wrist fracture is a minor fracture and the related costs are substantially lower. However, fragility fractures in one site can be used as a predictor of future fractures in different sites of the body, such as the hip and spine (Padegimas & Osei, 2013; Rozental *et al.*, 2013; Muller *et al.*, 2003). Furthermore, the frequency of radius fractures peaks at age 65, approximately 10 years before the peak for hip and spine fractures (Muller *et al.*, 2003), making early diagnosis at the distal radius important to predict future hip and spine fractures (Oyen *et al.*, 2010). In other words, the identification and treatment of fragility fractures on the distal radius is a great opportunity for the early detection of osteoporosis and reduction of its associated costs.

1.2 X-ray-based techniques for the assessment of osteoporosis

1.2.1 Dual-energy x-ray absorptiometry (DEXA)

Dual-energy X-ray absorptiometry (DEXA) is currently recognized as the gold standard to diagnose osteoporosis and evaluate the risk of fracture. DEXA measurement is based on dual X-ray beams of different energy levels, which interact differently according to the body tissue through which they propagate. Thus, the soft tissue effect can be eliminated and the mineral content of the bone can be interrogated separately, allowing the calculation of the Bone Mineral Density (BMD) (WHO, 1994). For the clinical assessment of osteoporosis and risk of fractures in patients, BMD is expressed in terms of standard deviations of a healthy young adult reference population, by a parameter commonly called the “T-score”. According to the World Health Organization (WHO) criteria, osteoporosis is recognized as a T-score of -2.5 or less (Sur, 2004).

The success of DEXA is mainly related to the acceptability of the X-ray technology, since all the mechanisms involving the interaction of X-rays with bone are well understood Gluer (1997). Moreover, DEXA densitometers have the ability to assess both peripheral and internal sites of the body using an acceptable dose of radiation for adults. The major limitation of DEXA is the fact that it is intrinsically insensitive to the mechanical properties of the bone, giving only an estimative of the relative risk of fracture through the general relationship between bone mineral density and mechanical properties (Haba *et al.*, 2016). Furthermore, DEXA seems to be insensitive to small variations in the BMD, taking several years to confirm a diagnosis and also showing difficulties to monitor response to treatments (Gluer, 1997). In addition, DEXA equipment is also relatively expensive and non-portable, restricting the analysis to large hospitals and making the access to the technology difficult in developing countries.

1.2.2 Quantitative computed tomography (QCT)

Quantitative Computed Tomography (QCT) is an X-ray modality that performs a volumetric density measurement with a high spatial resolution. Clinical CT can be generally considered

more sensitive to BMD changes when compared to DEXA (Li *et al.*, 2013). Furthermore, the QCT analyses can separately assess cortical and trabecular bone architectures, which is another advantage relative to DEXA (Engelke *et al.*, 2009). The main limitations of this technique are the high dose of X-ray radiation required to reach a good resolution on internal sites of the body and the high cost of the equipment, both higher than DEXA (Griffith & Genant, 2011).

1.2.3 High-resolution peripheral quantitative computed tomography (HR-pQCT)

High resolution peripheral quantitative computed tomography (HR-pQCT) is a relatively recent QCT imaging modality for assessing changes in cortical and trabecular bone on peripheral skeletal sites, such as the radius and the tibia. This technique can assess the bone architecture with an excellent spatial resolution, between 80-120 μm (Griffith & Genant, 2011), at a lower cost and smaller radiation doses, lower than an adult hip DEXA dose (Damilakis *et al.*, 2010). HR-pQCT demonstrates the capability to assess different structural parameters of peripheral bones, as shown in recent studies on the distal radius (Burt *et al.*, 2014; Kawalilak *et al.*, 2014; Zhu *et al.*, 2014). Indeed, HR-pQCT can be considered a promising new approach for estimating bone quality in peripheral sites. However, this X-ray based technique still provides an indirect assessment of mechanical properties, and, even if it is considered less expensive than other QCT techniques, it is too costly for a primary care setting.

1.3 Quantitative ultrasound (QUS) for the assessment of osteoporosis

The main motivation that drives the development of ultrasonic methods for osteoporosis assessment is the potential of the technique to directly interrogate the mechanical properties of the bone Kaufman & Einhorn (1993); Laugier & Haiat (2011). In addition, ultrasonic bone assessment can overcome the currently standard technique, DEXA, in other aspects, such as the possibility to separately interrogate the cortical and trabecular regions and the ability to assess other mechanical parameters than the BMD (Breban *et al.*, 2010). Furthermore, the ultrasonic equipment is portable, non-hazardous and relatively inexpensive (Gluer, 1997). As was mentioned before, wrist fractures play an important role in the early detection of future

fractures of different types. In this context, a cost-effective ultrasound technique to estimate the distal radius quality would represent an important tool to improve the management of osteoporosis. Currently, QUS assessment on radius is performed by two different techniques: (1) the through transmission method and (2) the axial transmission method. The research using these techniques are still being developed and a summary of the characteristics, as well as the advantages and limitations of each technique, is given below.

1.3.1 Through-transmission technique

Through-transmission techniques are based on the interaction between the mechanical properties and the propagating characteristics of the waves through the bone (Cavani *et al.*, 2008). The way that the waves interact with the bone depends on the operating frequency and the geometry of the transducers. Commonly, two transducers, a transmitter and a receiver, are positioned on opposite sides of the bone, usually in sites containing mainly trabecular bone: heel, distal radius or fingers (Mano *et al.*, 2013). Ultrasonic parameters, such as attenuation and speed of sound, are extracted from the measured signal, and then, bone properties can be estimated. Recently, different devices using through-transmission at the distal radius have been developed (Breban *et al.*, 2010; Stein *et al.*, 2013). As a limitation, the technique is not directly sensitive to elastic properties, reflecting mainly the porosity and architecture of the bone (Nicholson, 2008). In other words, the apparent sensitivity of the technique to the elastic properties exists most likely because there is a correlation between the structure, the porosity and the elastic properties, that are reflected together in the ultrasonic measurement.

1.3.2 Axial transmission technique

In axial transmission, the transmitter and the receiver are used to propagate ultrasonic waves along the axial direction of the bone. In axial transmission the transducers are positioned on the same side of the skeletal site. This method is mainly applied to long bones, such as the radius and tibia (Kilappa *et al.*, 2011). Furthermore, in the axial transmission setup, the generated waves travel along the cortical layer, instead of through the trabecular bone (Sievanen

et al., 2001; Bossy & Talmant, 2015). The first generation of axial transmission devices was developed based on the analysis of the time-of-flight (TOF) of the first arrival signal (FAS). In this approach, the velocity of the fastest mode is calculated by dividing the distance between the two transducers by the TOF of the first signal. The calculated FAS velocity can be, to some extent, correlated to the thickness and density of the cortical bone. Correlation between FAS measurements and bone degradation status has been performed in several clinical studies in different sites (Muller *et al.*, 2008; Kilappa *et al.*, 2011; Talmant *et al.*, 2009), but this simplistic approach does not seem to be sensitive enough to assess additional structural parameters to those predicted by DEXA measurements (Sasso *et al.*, 2009).

1.3.3 Axial transmission using ultrasonic guided waves

Ultrasonic guided wave methods have been successfully applied in non-destructive testing (NDT) to characterize different classes of materials, including composite plates and complex structures (Agostini *et al.*, 2003; Chimenti, 1997; Vallet *et al.*, 2014). In the last decade, the methods have been extensively studied and adapted to cortical bone quality assessment (Talmant, 2011; Nicholson *et al.*, 2002). Most developed axial transmission devices are focused on the assessment of the cortical tissue, since the cortical bone properties are affected by age-related bone reabsorption and osteoporosis (Rico, 1997). Furthermore, cortical bone accounts for the main portion of the skeleton and it supports most of the load of the body (Laugier & Haïat, 2011).

Similarly to pipes in the NDT field, long cortical bones such as the radius or tibia are suitable waveguides for the propagation of ultrasonic guided wave modes (Minonzio *et al.*, 2013). Each propagating mode interacts differently with the mechanical and geometric aspects of the waveguide, and this multi-modal characteristic can be considered the main advantage of the method, once the sensitivity of the analysis can be improved through the selection of a desired group of modes in order to interrogate a specific region/parameter of the bone structure. Recent studies based on this ultrasonic guided wave method already show considerable evidence that the multi-modal approach is more comprehensive and sensitive when compared

to the single velocity analysis (Ta *et al.*, 2006; Moilanen *et al.*, 2007a). However, due to the complex propagation characteristic of ultrasonic guided waves and the high number of modes, sophisticated multi-transducer setups (Minonzio *et al.*, 2010; Moilanen *et al.*, 2013) and signal processing algorithms (Xu *et al.*, 2010; Sasso *et al.*, 2008; ZhengGang Zhang & Wang, 2013) must be considered. A brief review of relevant concepts of ultrasonic guided waves theory and a semi-analytic simulation tool will be presented in the next section.

1.4 Ultrasonic guided waves

Ultrasonic guided waves are mechanical stress waves that propagate along any extended structure with a cross-section of finite dimensions. The wave energy is concentrated between the boundaries of the waveguide and travels in the direction parallel to the boundaries. In the quantitative ultrasound field, long bones with cylinder-like geometry can be considered as suitable waveguides for the propagation of ultrasonic guided waves (Minonzio *et al.*, 2013), and for that reason the discussion will adopt cylindrical coordinates which better represent bone systems (Figure ??). Extended content on ultrasonic guided wave propagation in cylindrical waveguide structures can be found in several textbooks (Rose, 2014; Collin, 1990; Cheeke, 2012). Here, only a brief overview is provided.

1.4.1 Ultrasonic guided waves in cylindrical waveguides

An ultrasonic guided wave in a cylinder can be described by the radial displacement field, $u(r, \theta, z, t)$, using the following expression:

$$u(r, \theta, z, t) = u(r)e^{i\vartheta\theta}e^{-i(kz-\omega t)} \quad (1.1)$$

where $u(r)$ is the radial distribution function characteristic of a specific mode, k and ϑ are the wavenumber in the axial and angular direction, respectively, z is the propagation direction, ω is the angular frequency and t is time. Considering the propagation along the axial direction of the cylinder, and continuous displacements in the angular direction, ϑ must be an integer and

is associated with the circumferential order of the mode. The wavenumber k can be complex if the waveguide has viscoelastic properties or if it is immersed in a viscoelastic medium.

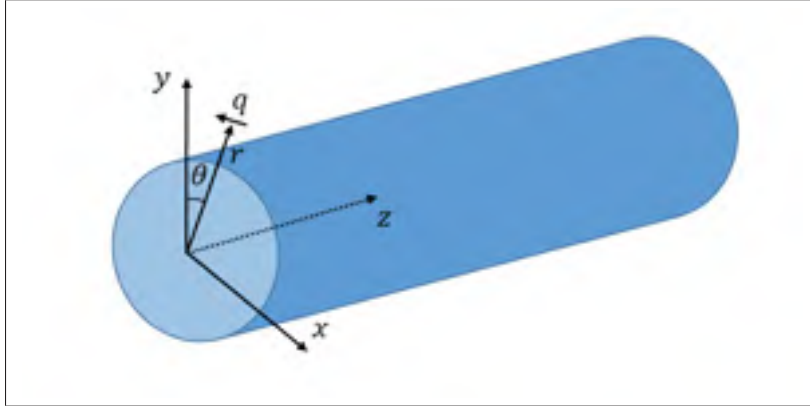


Figure 1.1 Cylindrical coordinates used to represent the bone system

The wave propagation phenomenon can be described by different parameters, depending on which kind of waves and the aspects or components to be considered. A common parameter for ultrasonic guided waves is the phase velocity, C_p which is defined as the rate at which the phase of the wave propagates in space. It is given by the wavelength Λ divided by the period T of vibration (equation (1.2)), or similarly dividing the angular frequency ω by the wavenumber k (equation (1.3)).

$$C_p = \frac{\Lambda}{T} \quad (1.2)$$

$$C_p = \frac{\omega}{k} \quad (1.3)$$

Another important parameter is the group velocity, C_g , defined as the velocity at which the energy of the wave propagates through space, giving an idea about how fast the energy of the wave is propagating along the z direction.

$$C_g = \frac{\partial \omega}{\partial k} \quad (1.4)$$

The group velocity will always be smaller than the fastest bulk wave present in the system and is given by the derivative of the angular frequency with respect to the derivative of the wavenumber, as shown in equation (1.4).

1.4.1.1 Dispersion curves

Ultrasonic guided waves exhibit dispersive characteristics of phase velocity and group velocity along the frequency axis. As a result of dispersion effects, the shape of the energy envelope that propagates along the structure is distorted, decreasing the amplitude of the signal. The dispersion curves are commonly used to predict those dispersive characteristics for each ultrasonic guided wave modes and for a specific frequency range. In order to select the most promising ultrasonic guided wave modes and operating frequency, it is fundamentally important to understand the dispersion curves of ultrasonic guided wave modes propagating in a certain waveguide.

In cylindrical waveguides, there are three families of ultrasonic guided wave modes: longitudinal, torsional, and flexural, each one with an infinite number of modes. Thus, the number of modes presented in a dispersion curve chart is only limited by the frequency and wavenumber range. Longitudinal and torsional modes are commonly abbreviated as $L(0,N)$ and $T(0,N)$, respectively, where the first parameter indicates the circumferential order and the second term distinguish the modes of the same family. The circumferential order for both longitudinal and torsional modes is zero, which means that the the mode-shape is constant around the circumference, in other words, they are axially symmetric. Flexural modes are abbreviated as $F(\vartheta,N)$, where the circumferential order in the first parameter is always 1 or higher.

Figure 1.2 shows the displacement field in the radial direction for longitudinal and flexural modes for a hollow steel cylinder at a frequency of 100 kHz. The geometrical parameters and material properties of the cylinder are given in Table 1.1. The displacement fields were obtained using the methodology presented in the section 1.4.2. Note that the longitudinal mode $L(0,1)$ has radial displacement constant around the circumference, while the flexural modes of

Table 1.1 The geometry parameters and material properties of the hollow cylinder.

Cylinder in vacuum	
Inner radius (mm)	7
Outer radius (mm)	10
Density (kg/m^3)	1600
Young modulus (GPa)	4.9
Poisson ratio	0.27

the same family $F(1,2)$, $F(2,2)$, $F(3,2)$ have different circumferential order.

Figure

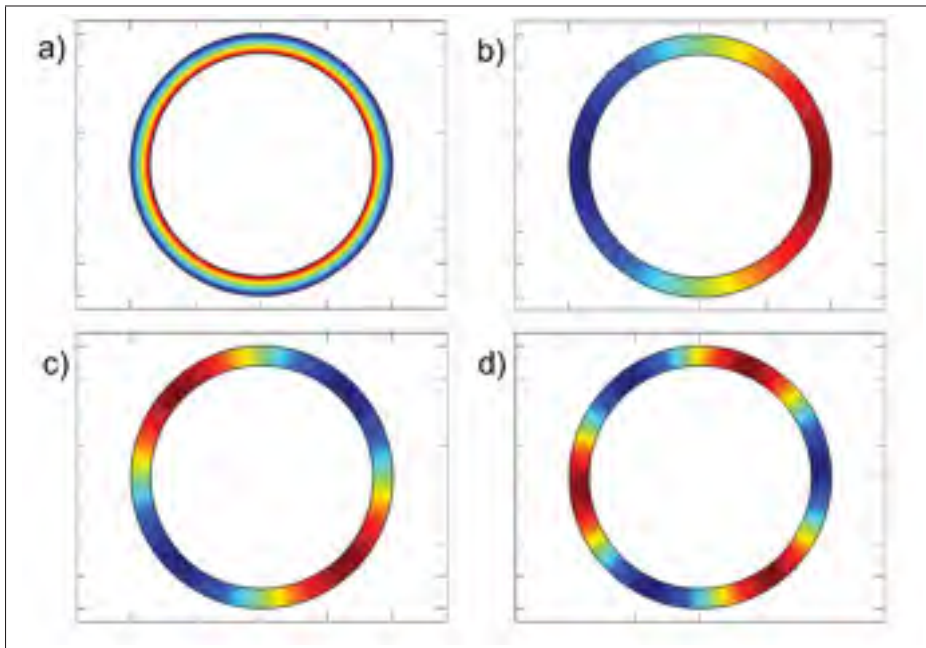


Figure 1.2 Displacement field in the radial direction for longitudinal (a) and flexural modes (b-d) for a hollow steel cylinder at frequency of 100 kHz.

1.3 shows the phase velocity dispersion curves of different families of ultrasonic guided wave modes propagating in a hollow cylinder in a vacuum (Table 1.1).

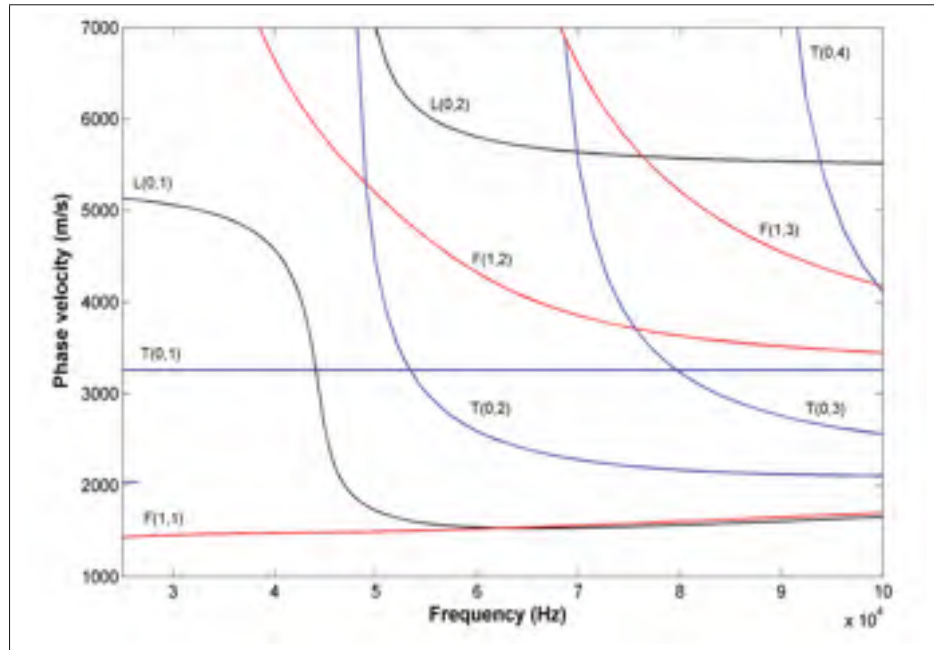


Figure 1.3 Phase velocity dispersion curves of ultrasonic guided wave modes in a hollow cylinder in vacuum. The dispersion curves were obtained using the methodology presented in the section 1.4.2.

1.4.1.2 Mode shape

The mode shape of an ultrasonic guided wave mode shows the distribution of the displacement, stress and energy fields along the cross-section of the waveguide. For each ultrasonic guided wave mode and each frequency in the dispersion curve, those quantities are different. Figure ?? shows the radial displacement variation for the frequency of 80 kHz, 100 kHz and 120 kHz for longitudinal $L(0,1)$ mode shape in a bi-layer cylinder. The geometrical parameters and material properties of the cylinder are the same given in Table 1.1. for the external layer, while the internal layer was modeled using different properties (Density= 1400 kg/m³, Young modulus= 3.5 GPa and Poisson ratio= 0.27)

The mode shape of the displacement field is commonly used to identify the mode family, but it is also related with the excitability of the mode. The mode excitability characteristic will be further discussed later in this thesis.

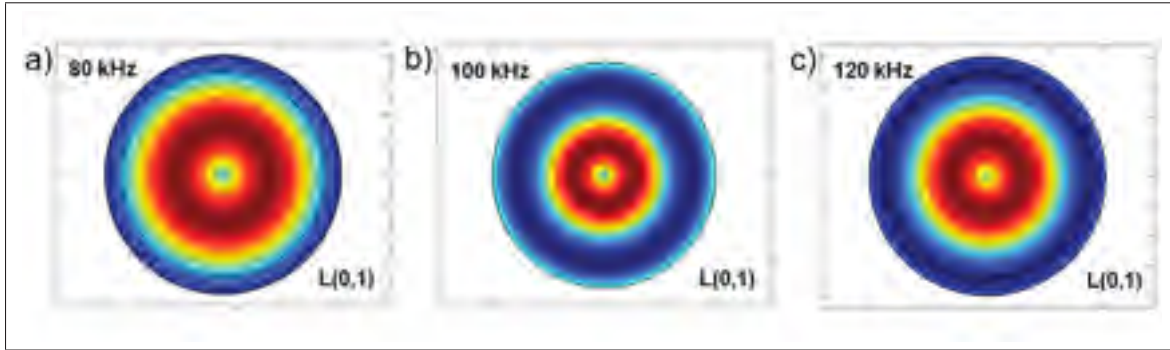


Figure 1.4 Radial displacement variation with the frequency for L(0,1) mode shape in a bi-layer cylinder. The displacement fields were obtained using the methodology presented in the section 1.4.2

Figure 1.5 shows the radial, axial and angular displacements along the thickness of a bi-layer cylinder waveguide for each mode family. It shows that the flexural mode exhibits displacement in the three directions, however, at the central point the angular displacement is always zero. The torsional mode exhibits only angular displacement, but it is zero at the central point. Finally, the longitudinal mode exhibits displacement mainly in the axial direction, but also some displacement in the radial direction. A summary of displacement features of each family of modes in a bi-layer cylinder is given in Table 1.2, where U_r , U_z and U_q denote radial, axial and angular displacements, respectively.

Table 1.2 Summary of displacement features of each family of mode in a bi-layer cylinder system.

Mode Family	Displacement	
	Radius line	Central point
Longitudinal	$U_r, U_z \neq 0; U_q = 0$	$U_r, U_z \neq 0; U_\theta = 0$
Flexural	$U_r, U_z, U_q \neq 0$	$U_q = 0$
Torsional	$U_q \neq 0; U_r, U_z = 0;$	$U_r, U_z, U_q = 0$

1.4.1.3 Modal excitability

Modal excitability is an important parameter that provides information on the amplitude of modes relative to each other for a given excitation direction. For example, to predict the prop-

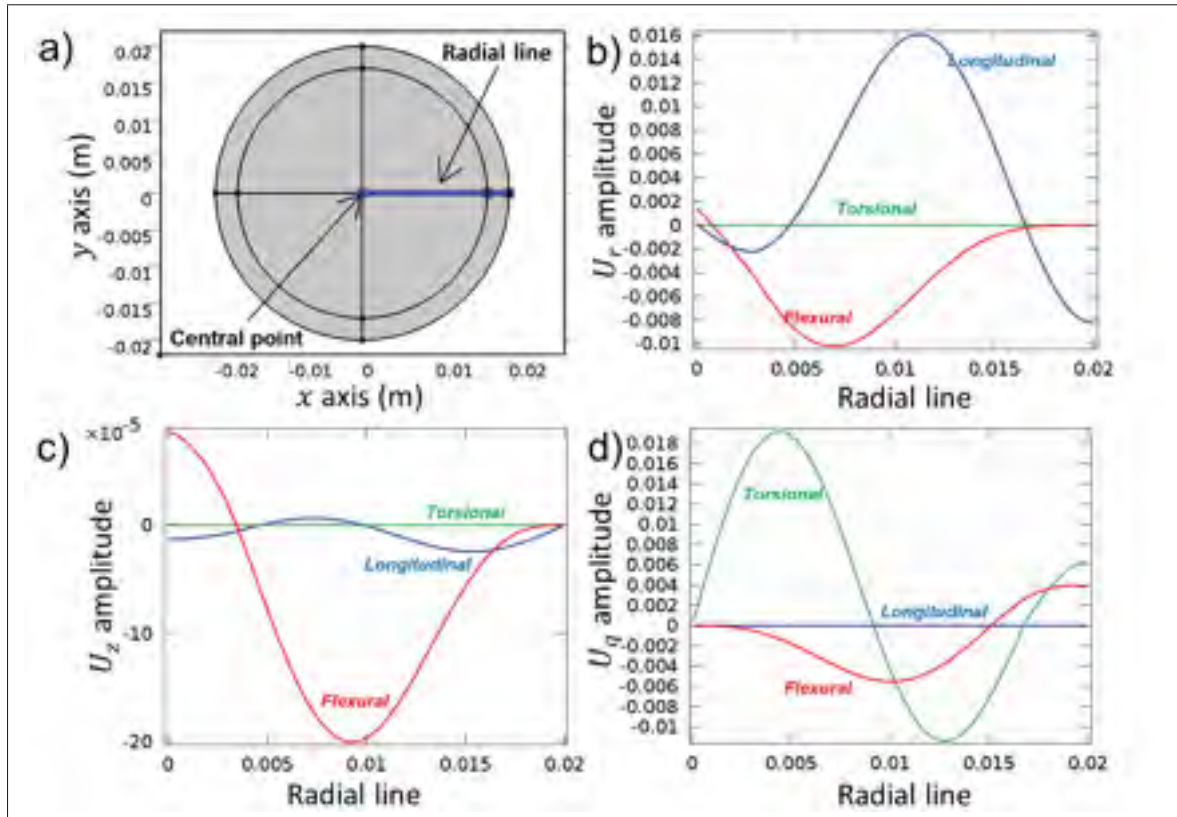


Figure 1.5 Displacement along the radial line according to the mode family for: a) radial displacement, b) axial displacement and c) angular displacement. The displacement along the radial line were taken from the displacement field obtained using the methodology presented in the section 1.4.2.

agating signal at the surface of a plate, excitability curves are crucial to distinguish the modes that can in fact be excited, and the mode that just exists theoretically and cannot be excited by a given excitation direction. Like the phase and group velocity, excitability curves are not constant along the frequency axis. For a given frequency, the modal excitability can be defined as the ratio of the induced force applied in a given direction to the displacement of the mode measured at the surface in the same direction. For a point excitation in a cylinder system, we can assume two different excitations: in-plane and out-of-plane. Using an analogy from the plate excitability (Wilcox *et al.*, 2005), out-of-plane excitation in cylinders will generate only circular crested Lamb waves (longitudinal and flexural modes), while in-plane excitation will generate a combination of circular crested Lamb waves and shear horizontal waves (torsional

modes), as shown in Figure 1.6. The definitions of in-plane and out of-plane excitation will be described separately next and they are only valid after the very near field.

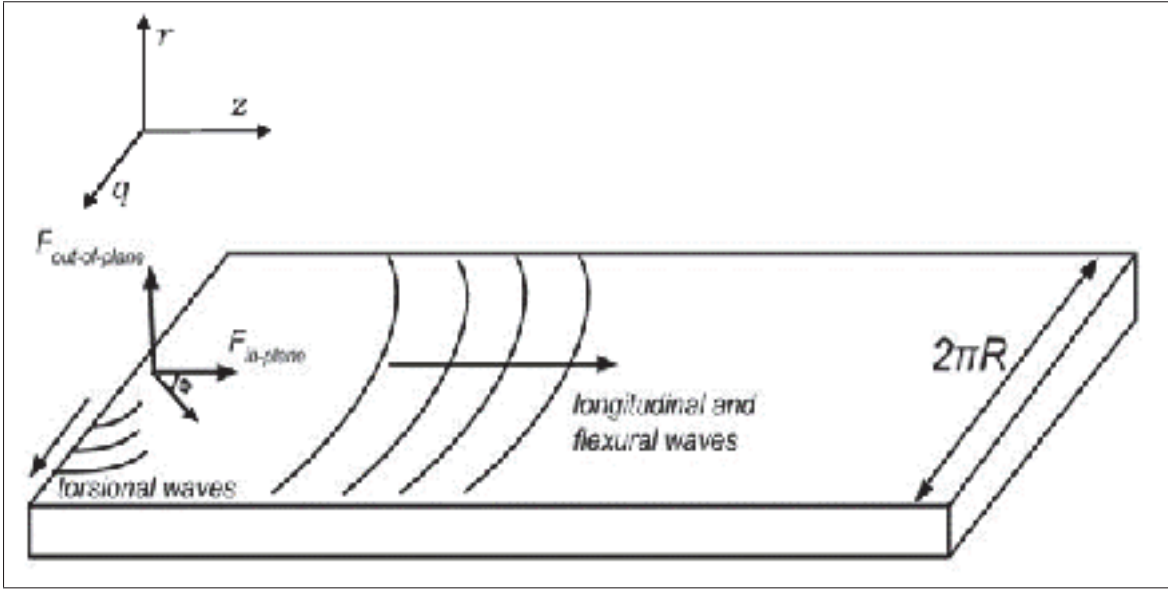


Figure 1.6 Plate analogy of circular Lamb waves and shear horizontal waves generated by out-of-plane and in-plane point excitation in a cylinder.

The out-of-plane point excitability of a specific mode responsible for out-of-plane displacement can be calculated in terms of the out-of-plane displacement on the surface, u_r , by the following equation:

$$E_{(r)}^{(r)} = \frac{ik\omega}{8} \left(\frac{u_r^2}{P} \right) \quad (1.5)$$

where i is $\sqrt{-1}$, and P the power flow associated with the mode shape. Similarly, the out-of-plane excitability responsible for the in-plane displacement can be defined in terms of the out-of-plane and in-plane displacements (u_r and u_z , respectively) on the surface of the mode as:

$$E_{(z)}^{(r)} = \frac{ik\omega}{8} \left(\frac{u_r * u_z}{P} \right) \quad (1.6)$$

In-plane point excitability

For the in-plane point force, the excitability can be divided into two kinds: the waves generated in the longitudinal direction z , composed by longitudinal and flexural modes (equations (1.7)

and (1.8)); and the waves excited in the tangential direction q by torsional modes (equations (1.9) and (1.10)). The in-plane point excitability in the longitudinal direction responsible for the in-plane displacement can be expressed by:

$$E_{(z)}^{(z)} = \frac{ik\omega}{8} \left(\frac{u_z^2}{P} \right) \cos\phi , \quad (1.7)$$

Where ϕ is the angular position with respect to the applied force (Figure 1.6). Similarly, the in-plane point excitability in the longitudinal direction responsible for the out-of-plane displacement can be defined by:

$$E_{(r)}^{(z)} = \frac{ik\omega}{8} \left(\frac{u_z^* u_r}{P} \right) \cos\phi , \quad (1.8)$$

Finally, for the tangential direction, q , the in-plane point excitability responsible for the in-plane displacement (Equation (1.9)) and responsible for the out-of-plane displacement (Equation (1.10)) can be defined as:

$$E_{(z)}^{(z)} = \frac{ik\omega}{8} \left(\frac{u_z^2}{P} \right) \sin\phi \quad (1.9)$$

$$E_{(r)}^{(z)} = \frac{ik\omega}{8} \left(\frac{u_z^* u_r}{P} \right) \sin\phi . \quad (1.10)$$

1.4.2 Semi-analytical finite-elements method (SAFE)

The Semi Analytical Finite Element (SAFE) method has been extensively used to study uniform waveguides of arbitrary cross-sections (Hayashi *et al.*, 2003; Treysse & Frikha, 2008; Fan *et al.*, 2008a; Mazzotti *et al.*, 2013; Bartoli *et al.*, 2006). The main advantage of this method when compared to conventional finite element modeling, is the fact that only the cross-section needs to be modeled and meshed (Predoi *et al.*, 2007). The method assumes that the waves propagate harmonically in the axial direction (z direction), and for that reason it can be consid-

ered computationally more efficient. Moreover, the method is much more comprehensive than the traditional global matrix method for multilayered media (Pavlakovic & Lowe, 1999; Lowe, 1995). Figure 1.7 shows the arbitrary cross-section waveguide SAFE representation.

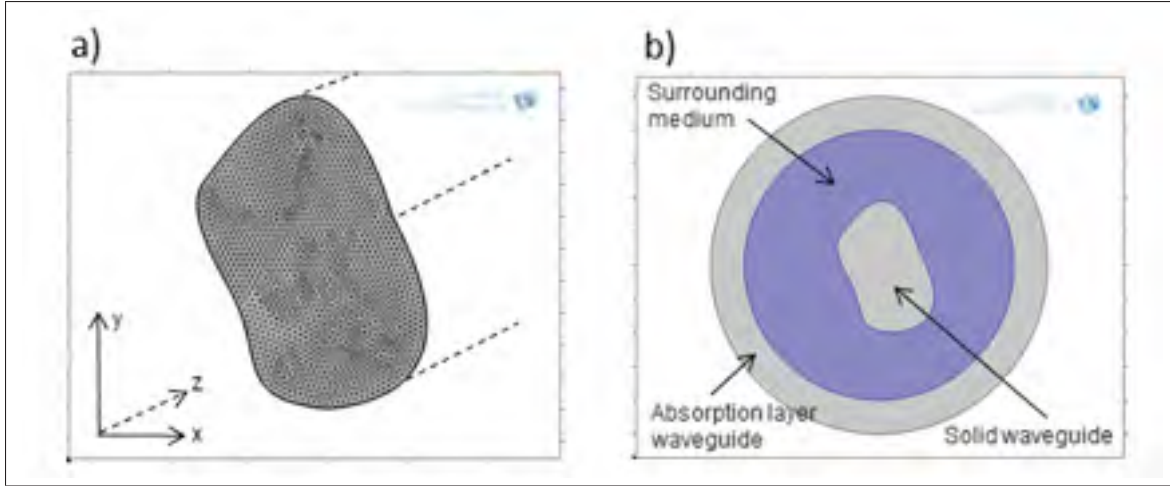


Figure 1.7 SAFE representation system; a) meshed arbitrary cross-section waveguide; b) representation of a waveguide in a multi-layer system (built using COMSOL Multiphysics Graphic User Interface).

The SAFE approach was first applied to waveguides of arbitrary geometries in the 70s (Kumar, 1972), but through recent development of specific finite element codes and improvements in system description, such as the consideration of material anisotropy (V. V. Volovoi & Sutyryn, 1998) and leaky waves (Fan *et al.*, 2008b). The first implementation of the SAFE method using the finite element eigenvalue formalism was done by Predoi *et al.* (2007), using a commercial finite element software, COMSOL Multiphysics. In this thesis, a brief review of the SAFE equations and finite element formalism is given.

1.4.2.1 SAFE in solid waveguide

As mentioned above, the waves are assumed to propagate harmonically in the axial direction (z direction) of the waveguide. Then, the displacements vector can be described as:

$$u_g(x, y, z, t) = U_g(x, y) e^{-i(kz - \omega t)}, \quad i = \sqrt{-1} \quad (1.11)$$

where $g=1,2,3$ and ρ is the mass density. Considering C_{ijkl} as the elastic constants, the differential equations of motion for an anisotropic material can be defined using the formalism for eigenvalues problems by:

$$C_{ghjl} \frac{\partial^2 U_j}{\partial x_h \partial x_l} + i(C_{g3jl} + C_{ghj3}) \frac{\partial(kU_j)}{\partial x_h} - kC_{g3j3}(kU_j) + \rho \omega^2 \delta_{gj} U_j = 0, \quad (1.12)$$

with the subscripts $h, l=1, 2$, and where δ_{gj} is the Kronecker symbol. In a commercial finite element software, the same formalism can be expressed by:

$$\Lambda^2 e_a u - \Lambda d_a u + \nabla \cdot (-c \nabla u - \alpha u + \gamma) + \beta \cdot \nabla u + a u = 0 \quad (1.13)$$

where u represents the unknowns. Comparing the two formalism and considering $\gamma=0$ and $e_a=0$, the coefficients c , α , β , a and d_a in equation (1.13), can be defined in terms of stiffness properties, density ρ and ω in order to match to equation (1.12). The detailed description of the coefficients used in this thesis is given by Predoi *et al.* (2007). Thus, the equation (1.13) can be solved for a certain angular frequency ω , resulting in an infinite number of complex wavenumbers k as an eigenvalue solution of the equation. Dispersion can be achieved by selecting all the propagative modes among the wavenumber solutions for a desired number of frequencies.

1.5 Chronological arrangement of the manuscripts

The core of this thesis consist on three journal publications. In addition, this thesis contains two conference proceeding that are presented as a supplementary content. The contextualization as well as the chronological sequence of these studies are described next:

Initially, a preliminary study involving 3D finite element (FE) simulations (appendix I) was performed to evaluate the potential of ultrasonic guided waves assessing the properties of trabecular bone at distal radius. The diagnosis of osteoporosis at skeletal sites composed mainly of trabecular bone is know to be clinically relevant. Therefore, the possibility to assess this site using ultrasonic guided waves is very motivating. Thus, this simulation study was published on

this topic in the Proceeding of the 170th Meeting of the Acoustical Society of America (Jacksonville, Florida, US), in November 2016. However, the proposed configuration was found to be very limited at a practical level for the propagation of ultrasonic guided waves due to the nonuniform nature of the cross-section along the distal region. From this point, the focus of this thesis changed to the assessment of cortical bone properties in middle 1/3 radius instead. The assessment of cortical bone have significant interest since it supports most of the body load is know to be associated with a number of osteoporotic fractures. Furthermore, the middle region consist in a much more suitable waveguide for the propagation of ultrasonic guided waves.

After that, a SAFE method was developed in the context of axial transmission method on cortical bone. The SAFE model provided a comprehensive and computationally efficient tool to simulate and understand the propagation of ultrasonic guided waves in the cortical bone medium. The SAFE method is attractive when modeling constant waveguide with arbitrary cross-section because of the significant reduction in computation time when compared to conventional 3D finite element (FE) simulation. A journal paper (Chapter 2) was published on this topic in April 2017 in the Journal of Acoustical Society of America (JASA). This study consist on the implementation of the SAFE model in the context of axial transmission in the middle 1/3 radius to investigate the feasibility of first arrival signal (FAS) to monitor degradation of intracortical properties at low frequencies. The FAS velocity consist on a very simple approach that has been extensively used to evaluate bone quality *in-vivo* but feasibility at low frequencies was completely investigated. From this publication, the FAS velocity was shown to be a poor discriminator of intracortical bone properties, which was mainly associated with the destructive and constructive interference between propagating modes in the time-domain signal at low frequencies.

To address this limitation, a time-spatial frequency analysis technique instead of the FAS velocity was proposed using a large array of receivers. A second manuscript (Chapter 3) was published on this topic in January 2019 in the same journal (JASA). In this study, the effect of intracortical bone properties on the phase velocity and cut-off frequency of low-frequency ultrasonic guided wave modes was determined for different excitation positions on the bone

surface. The results of this manuscript suggested that by selecting an adequate frequency and position of excitation, the low-frequency axial transmission (combined with appropriated frequency-domain signal processing techniques) was able to identify promising mode features for assessing intracortical bone properties.

Based on the success in the second publication (Chapter 3, an autonomous model-based optimization routine was proposed to perform the inverse characterization of the cortical bone properties. The model used in the second publication was adapted to a parameterized bone-like geometry and used to perform the inverse characterization of five *ex-vivo* radius samples at low frequencies (<60 kHz). A third journal paper (Chapter 4) was submitted on this topic to IEEE Transactions on Ultrasonics, Ferroelectrics and Frequency Control Journal in November 2018, which is currently under revision.

As an extension of this thesis, the inversion method implemented in the third paper was applied to another application. A very inversion procedure applied in Chapter 4 was adapted to perform the inverse characterization of a stiffener bonded line using an appropriated SAFE geometry and model parameters. This study was presented at the 45th Annual Review of Progress in Quantitative Nondestructive Evaluation (Burlington, Vermont, US) in July 2018 and published in the Proceeding of the 45th Annual Review of Progress in Quantitative Nondestructive Evaluation (Burlington, Vermont, US), in November 2018. (Appendix II).

The the next chapters (chapter 2, 3 and 4) consist of the complete journal manuscript while the two appendixes (appendix I and II) contains conference proceeding.

CHAPTER 2

SIMULATION OF ACOUSTIC GUIDED WAVE PROPAGATION IN CORTICAL BONE USING A SEMI-ANALYTICAL FINITE ELEMENT METHOD

Daniel Pereira^{1 4}, Guillaume Haiat^{1 2}, Julio Fernandes^{3 4}, Pierre Belanger^{1 4}

¹ Département de Génie Mécanique, École de Technologie Supérieure,
1100 Notre-Dame Ouest, Montréal, Québec, Canada H3C 1K3

² Centre National de la Recherche Scientifique, Laboratoire Modélisation et Simulation
Multiechelle, 61 avenue du Général de Gaulle, Cretéil Cedex, 94010, France

³ Department of Surgery, Université de Montréal, 2900 Boulevard Edouard-Montpetit,
Montreal, Quebec, H3T1J4 Canada

⁴ Centre de recherche l'Hôpital du Sacré-Coeur de Montréal, 5400 Boul Gouin O, Montreal,
Quebec, H4J1C5 Canada

Paper published in *The Journal of the Acoustical Society of America*, April 2017.
[<http://dx.doi.org/10.1121/1.4979695>]

Abstract Axial transmission techniques have been extensively studied for cortical bone quality assessment. However, the modeling of ultrasonic guided waves propagation in such a complex medium remains challenging. The aim of this paper is to develop a semi-analytical finite element method to simulate the propagation of guided waves in an irregular, multi-layer and heterogeneous bone cross-section modeled with anisotropic and viscoelastic material properties. The accuracy of the simulation results was verified against conventional time-domain three-dimensional (3D) finite element simulations. The method was applied in the context of axial transmission in bone to investigate the feasibility of first arrival signal (FAS) to monitor degradation of intracortical properties at low-frequencies. Different physiopathological conditions for the intracortical region, varying from healthy to osteoporotic, were monitored through FAS velocity using a 10-cycles tone burst excitation centered at 32.5 kHz. The results show that the variation in FAS velocity is mainly associated with four of the eight modes supported by the waveguide, varying with velocity values between 550 m/s and 700 m/s along the different scenarios. Furthermore, the FAS velocity is shown to be associated with the group velocity

of the mode with the highest relative amplitude contribution at each studied scenario. However, because of the evolution of the mode with the highest contribution, the FAS velocity is shown to be limited to discriminate intracortical bone properties at low-frequencies.

Keywords: Ultrasonic guided waves, Cortical bone, Axial transmission.

2.1 Introduction

One particular topic of interest to the biomedical engineering community is the possibility of using quantitative ultrasound (QUS) to monitor bone conditions. A cost-effective, non-hazardous and in-situ system that can be used to obtain the properties of the bones in a non-invasive manner is very desirable in this context (Gluer, 1997). Axial transmission techniques have been extensively studied for cortical bone quality assessment (Laugier & Haiat, 2011; Haiat *et al.*, 2011). Long cortical bones such as the radius or tibia are suitable waveguides for the propagation of ultrasonic guided waves. The possibility of measuring ultrasound waves using the axial transmission technique has been already demonstrated by several studies (Gluer, 1997; Haba *et al.*, 2016; Gluer, 2008). Axial transmission assessment using ultrasonic guided waves is attractive because they can interrogate mechanical and geometrical properties of cortical bone. When studying axial transmission configuration, it is of interest to develop effective modeling methods that accurately predict the excitation and propagation of each ultrasonic guided wave mode separately. For simple geometries, such as plates and cylinders, analytical solutions may be obtained (Pavlakovic *et al.*, 1997; Jin *et al.*, 2003). The effect of microstructure can be introduced by using non-classical elasticity theories such as higher-order gradient theories of elasticity (Vavva *et al.*, 2009). However, to predict time responses of complex geometry waveguides, such as long bone, numerical procedures are commonly used. Bossy *et al.* (2004) performed three-dimensional finite difference simulations using a realistic cortical bone model to evaluate the effect of curvature, cortical thickness, anisotropy, and microporosity on speed of sound. Similarly, Protopappas *et al.* (2007) performed 3D finite element simulations to investigate the influence of geometrical irregularities and callus formation on the characteristics of guided wave propagation. However, the simulation of the time responses using

these methods is typically computationally expensive because of the large number of elements required and the small time step between each increment. In addition, simulation of the responses of the individual ultrasonic guided wave modes using this method is not trivial. The semi-analytical finite element (SAFE) method can be used to study the propagation of guided waves in arbitrary cross-section waveguides in an effective way. The first implementation of the SAFE method on thin-walled arbitrary waveguides was done by Gavrić (1995), in 1995, on rail structures. More recently, the method has been applied in the context of the axial transmission technique for computation of the modal properties of cortical bone waveguides (Tran *et al.*, 2015; Castellazzi *et al.*, 2013). However, the method has not been thoroughly explored yet. The method enables the implementation of heterogeneous and viscoelastic material properties (Bartoli *et al.*, 2006). In addition, it is possible to consider a layer of surrounding fluid. All these features combined make the method suitable to model bones as waveguides. Moreover, the method assumes harmonic wave propagation along the axial direction while free displacement is assumed across the cross-section. Thus, only a 2D cross-section needs to be modeled and meshed, which results in a significant reduction in computation time. The modal properties of the waveguide are commonly computed in the frequency domain. In order to study the time domain interaction between each mode, time responses are required. In this paper, the modal properties of the waveguide in the frequency domain were used to compute the responses in the time domain, allowing the simulation of responses that can be directly compared with those obtained experimentally. The simulated time domain responses consist in a linear superposition of the response of each mode supported by the waveguide. This approach enables the simulation of only the selected modes, leading to a better understanding of the contribution of each mode to the wave propagation. The aim of this paper is to present a computationally efficient semi-analytical finite element method to simulate the propagation of acoustic guided waves in cortical bone modeled as a waveguide. The novelty of this study lies in the computation of the dispersion curves of the cortical bone waveguide with irregular, heterogeneous and multi-layer cross-section. The method allows the use of anisotropic and viscoelastic material properties. In order to verify the accuracy of the method, the simulations were first compared against conventional time-domain 3D finite element simulations. The method was then applied in the context

of an axial transmission configuration in order to investigate the feasibility of FAS velocity at low-frequencies. The FAS velocity is the most commonly used method to evaluate bone quality *in-vivo* (Barkmann *et al.*, 2000; Stegman *et al.*, 1995; Hans *et al.*, 1999) and its feasibility at low-frequencies has not been completely investigated yet. The current bone geometry of a human radius was modeled using different physiopathological conditions for the intracortical region, varying from healthy to osteoporotic. The excitation was performed using a 10-cycles tone burst centered at 32.5 kHz. The propagation was monitored through FAS velocity at a position 150 mm away from the point source. The results shown that FAS velocity is mainly associated with the group velocity of the mode with highest relative amplitude contribution. However, the mode with the highest amplitude contribution evolves with the properties of the bone waveguide. As a result, the FAS velocity is shown to be a poor discriminator of intracortical bone properties at low-frequencies.

2.2 Acoustical modeling of wave propagation

This section first describes the SAFE method employed to model wave propagation. Then, a finite element method used for the validation of our approach is described.

2.2.1 Semi-analytical finite element method

The SAFE method was used to simulate guided wave propagation in the time domain and in an infinite arbitrary cross-section waveguide. The modal properties of the waveguide were first determined in the frequency domain and then transformed into the time domain. Such an approach for computing the time response from the modal properties of waveguides had previously been performed by different authors, including (Wilcox *et al.*, 2001), considering a point source excitation and (Loveday, 2008), using a coupling with 3D piezoelectric elements as a source. In this paper, the resulting time domain signals consist in a superposition of the propagated response of each dispersive mode supported by the waveguide, excited from a point source in the out-of-plane direction.

2.2.1.1 Formulation of the semi-analytical finite elements

The SAFE method assumes that ultrasonic guided waves propagate harmonically in the axial direction z . Constant cross-section and material properties are assumed along the axial direction. Thus, the displacements field u_g can be described as (Fan *et al.*, 2008a):

$$u_g(x, y, z, t) = U_g(x, y) e^{-i(kz - \omega t)}, \quad i = \sqrt{-1} \quad (2.1)$$

where $g=1,2,3$, U_g is the displacement field in the cross-section plane (x, y) , k is the wavenumber, and ω is the angular frequency. Considering the mass density ρ and the viscoelastic coefficients C_{ghjl} , the differential equations of motion for an anisotropic material can be defined using the formalism for eigenvalues problems by:

$$C_{ghjl} \frac{\partial^2 U_j}{\partial x_h \partial x_l} + i(C_{g3jl} + C_{ghj3}) \frac{\partial(kU_j)}{\partial x_h} - kC_{g3j3} (kU_j) + \rho \omega^2 \delta_{gj} U_j = 0, \quad (2.2)$$

where

$$C_{ghjl} = C + Ni \quad (2.3)$$

with the subscripts $j=1, 2, 3$ and $h, l=1, 2$, where C and N are the elastic and viscous components of the viscoelastic coefficients and δ_{gj} is the Kronecker symbol. Equation 4.2 can be solved for a given angular frequency ω , resulting in infinite instances of complex wavenumber k and their respective displacement fields $U_j(x, y)$, the so-called mode shapes. The dispersion curve of each mode $k(\omega)$ can be obtained by selecting all the wavenumbers that have real parts significantly higher than the imaginary parts at each frequency. The curves provide the dispersive behavior of each mode that can propagate in the waveguide of interest. Furthermore, the modal properties, such as power flow and surface displacement, can be calculated based on the mode shape obtained at each frequency. These modal properties are used to simulate the theoretical time domain signal, as explained next.

2.2.1.2 Simulation of time domain signal

The time domain signal of a single guided wave mode excited from a point source and propagated over a certain distance along a given waveguide can be obtained by (Wilcox *et al.*, 2005):

$$u(t) = \frac{1}{2\pi} \int_{-\infty}^{+\infty} F(\omega) E(\omega) H_0^{(1)}(k(\omega) z_0) e^{-i\omega t} d\omega, \quad i = \sqrt{-1}, \quad (2.4)$$

where $u(t)$ is the out-of-plane surface displacement for a given mode as a function of time t , for an arbitrary propagation distance z_0 . The factor $H_0^{(1)}$ is the first Hankel function of order zero and $F(\omega)$ is the frequency spectrum of the force input signal $u_{input}(t)$ (a 10-cycle Hanning windowed tone burst centered at 32.5 kHz). The factor $k(\omega)$ is the mode wavenumber, defined as a complex number by:

$$k(\omega) = k(\omega)_{real} + ik(\omega)_{imag} \quad (2.5)$$

where the real part denotes the propagating term and the imaginary part denotes the attenuation associated with the wavenumber. The factor $E(\omega)$ is the excitability with the mode of interest as a function of the angular frequency respectively. The out-of-plane excitability can be defined roughly as the ratio between the applied out-of-plane force and the resulting out-of-plane displacement related to the mode of interest. More details related to the definition of excitability are given by Wilcox *et. al* (Wilcox *et al.*, 2005). The frequency-dependent out-of-plane excitability of a given mode can be obtained by:

$$E(\omega) = \frac{ik(\omega)\omega}{8} \left(\frac{U_{max}(\omega)^2}{P_z(\omega)} \right) \quad (2.6)$$

where $P_z(\omega)$ is the total power flow in the z -direction associated with the mode shape as a function of the angular frequency, and $U_{max}(\omega)$ is the maximum out-of-plane displacement on the surface of the mode shape in terms of the angular frequency. Thus, modes having large displacements in the out-of-plane direction tend to have higher out-of-plane excitability. Finally, the complete time domain signal $u_{sum}(t)$, including all the ultrasonic guided wave

modes supported by the waveguide can be obtained by the sum of the n existing modes by:

$$u_{sum}(t) = \sum_{m=1}^n u^m(t) \quad (2.7)$$

where $u^m(t)$ is the out-of-plane displacement associated with the m -th mode after propagating an arbitrary distance z_0 , and n is the total number of modes supported by the waveguide. It is worth noting that this approach considers the waveguide as infinite, neglecting the waves traveling around it (in the circumferential direction) and ignoring the reflections from the ends. The waves traveling in the circumferential direction will arrive later compared to the waves traveling straight in the axial direction. Therefore, the measured FAS velocity will not be affected by waves traveling circumferentially since the FAS is calculated using the beginning of the signal.

2.2.2 Finite element method

The accuracy of the SAFE method described above was verified by comparing the results with those obtained from a 3D finite element simulation. The validation was carried out by considering a 500 mm long cortical bone waveguide filled with bone marrow and surrounded by 3.5 mm of soft tissue. Cortical bone layer was modeled by a homogeneous transversally isotropic medium using the elastic coefficients and density shown in Table 2.1, for the "Middle" region. Soft tissue and bone marrow were modeled using the properties of water (Naili *et al.*, 2010) (bulk modulus= $2.25e9$ Pa and density= 1000 kg/m³). Absorbing boundaries were added to avoid reflections from the edges (Drozd *et al.*, 2007). The mesh was built using 1 mm tetragonal-shaped elements, respecting a constraint of at least 15 elements per wavelength. The complete mesh size consists of around 611,000 elements and results in approximately 4,600,000 degrees of freedom. The simulation was carried out in the time domain using explicit integration. A $2e-8$ seconds time step was considered, and the total simulation time was equal to 1 ms. A point force source in the out-of-plane direction was applied in contact with the upper part of the periosteal region of the bone cross-section as shown in Figure 2.2, at one extremity of the model. The excitation signal was the same as the one applied for the

SAFE method (a 10-cycle Hanning windowed tone burst centered at 32.5 kHz). A linear array of 73 receivers equally spaced by 4 mm was placed along the axial direction, recording the out-of-plane displacement. The problem was solved using the ABAQUS 6.13-1 software. Once the 73 signals were obtained in the time domain, they were processed using the 2D-FFT (Alleyne & Cawley, 1990) in order to obtain the intensities of the propagating modes in the wavenumber-frequency diagram. The obtained intensities were then compared to the simulations performed by the SAFE method using equivalent configurations.

2.3 Application to cortical bone

In this section, the SAFE method described in the previous section was applied to cortical bone assessment. The ultrasonic responses were computed at different positions along a heterogeneous waveguide in the context of axial transmission configuration. Different physiopathological conditions were simulated and the contribution of each mode to the first arrival signal (FAS) velocity was investigated.

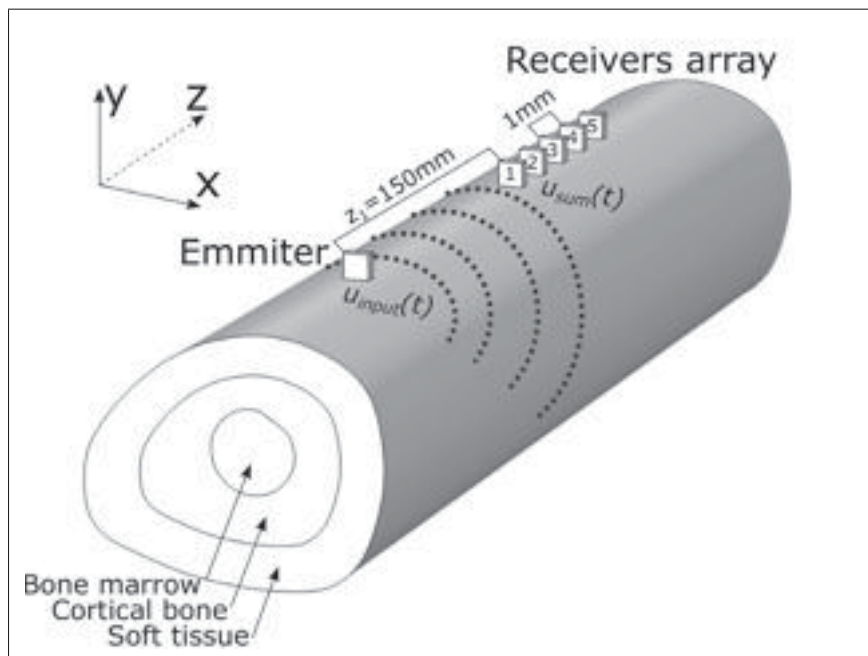


Figure 2.1 Schematic of the equivalent 3D axial transmission configuration used to perform the SAFE simulations.

2.3.1 Axial transmission configuration

The geometrical configuration (see Figure 2.1) was modeled as a 2D multilayer medium composed of a viscoelastic heterogeneous solid layer corresponding to cortical bone. The solid layer was surrounded by two viscoelastic homogeneous fluids corresponding to bone marrow and soft tissues, respectively.

Such a 2D multilayer waveguide is assumed to have an infinite length along the axial direction, resulting in a 3D equivalent medium, as shown in Figure 2.1. The bone geometry was taken from a micro computed tomography (μ CT) image of a human radius sample obtained in the middle of the long bone. Cortical bone was modeled as a transverse isotropic viscoelastic material with heterogeneous material properties along the radial direction (see subsection 2.3.2.2 for further details). Acoustic excitation was performed using a point source located in a plane denoted $z_0 = 0$ in contact with the upper part of the periosteal region of the bone cross-section as shown in Figure 2.2. The input waveform was defined as a 10-cycle Hanning windowed tone burst centered at 32.5 kHz. The frequency was chosen based on a recent study performed by (Moilanen *et al.*, 2013), which reported improved performance of fundamental flexural modes in assessing cortical bone thickness using low ultrasonic frequency (30 kHz). A large number of cycles was used to reduce the bandwidth in order to control the number of excited modes. The propagating waves were monitored using out-of-plane displacement at five positions (#1, #2, #3, #4 and #5) on the same side of the excitation. The acquisition positions were separated by a distance of 1 mm, varying from $z = 150$ mm to $z = 155$ mm. For each position # i located at $z = z_i$, the time t_i of the FAS was determined when the envelope of the signal crossed a pre-established threshold. The threshold was defined based on a percentage of the maximum envelope amplitude of the complete signal, 10% in this study. The FAS velocity was then given by the slope of z_i as a function of t_i obtained through a least-square linear regression analysis. For high frequencies, the FAS velocity is consistent with the bulk velocity propagating in thick waveguides. The SAFE method might not be interesting for calculating the signal at those frequencies since the number of modes increases drastically. However, the SAFE method is still suitable to determine the signal at higher frequencies up to approximately 500 kHz (as-

suming a cortical thickness of 4 mm) (Bossy *et al.*, 2002). At low-frequencies, the wavelength is large when compared to the bone thickness. Therefore, the waves are guided by the boundaries of the bone and travel with the velocity of guided wave modes. The FAS is expected to have the velocity of the fastest guided wave modes traveling in the waveguide. In addition, the amplitude contribution of each mode was calculated in order to provide an estimation of the influence of each mode on the FAS velocity. This parameter is useful for understanding the variations of the FAS velocity for the different scenarios investigated in this work. In order to calculate this parameter, the acquisition at position #3 was performed considering each mode separately, which was made possible by the flexibility of the SAFE approach (see subsection 2.2.1 for further details). Then, for the response obtained for each mode, the amplitude was measured at the same time step as the response signal that the FAS velocity was calculated (in the acquisition containing all modes). In other words, the mode contribution used the time t_3 , obtained by the thresholding method in the acquisition considering all modes, as a reference to calculate the amplitude in the acquisition, considering a single mode. More specifically, the relative amplitude contribution of each mode A^m can be estimated by:

$$A^m = \frac{a^m}{\sum_{m=1}^n a^m} \quad (2.8)$$

where a^m is the envelope amplitude of the m -th mode at time t_3 , and n is the total number of modes.

2.3.2 Modeling cortical bone

2.3.2.1 Cortical bone waveguide

The bone geometry was taken from μ CT images of a human radius provided by Sawbones (Sawbone - Pacific Research Laboratories, USA). The images were converted into a 3D model and delivered as a CAD geometry by the supplier, where the original dimensions of the human bone were kept. The boundaries of the waveguide were extracted from a slice of the

CAD geometry. In this work, the middle 1/3 region was used, which is composed only of cortical bone, as shown in Figure 2.2. Additionally, bone marrow and 3.5 mm of soft tissue were added internally and surrounding the cortical bone, respectively. The selected slice was imported into COMSOL Multiphysics-5.2, and meshed using triangular elements with a maximum size of 0.55 mm. The complete mesh size consists of around 3,400 elements, resulting in approximately 62,400 degrees of freedom. The bone marrow and soft tissue were modeled as homogeneous viscoelastic fluids with the same properties used by (Naili *et al.*, 2010) (bulk modulus= $2.25e9+1.97fi$ Pa and density= 1000 kg/m^3), while cortical bone was modeled as a viscoelastic transversally isotropic material. Furthermore, cortical bone was divided into three regions along the radial direction: periosteal (A-B), middle (B-C) and endosteal region (D-E) (see Figure 2.2a). Each region was defined with different values for the transversally isotropic stiffness coefficients and density ($C_{11}, C_{13}, C_{33}, C_{44}, C_{66}$ and ρ). The value of each region was chosen based on a simplification of experimental results reported by (Sansalone *et al.*, 2010), which were obtained using 3D synchrotron micro-computed tomography images. A more detailed description of the distribution of the material properties along the radial direction is provided in the next section. Because of a lack of available data, the viscoelastic coefficients ($N_{11}, N_{13}, N_{33}, N_{44}$ and N_{66}) were defined based on the same ratio between the viscosity and elastic coefficients found in the literature, as given by:

$$N_c = \frac{\eta_c^*}{C_c^*} \cdot C_c \cdot f = \eta_c \cdot f \quad (2.9)$$

where the subscript $c=11, 13, 33, 44$ and 66 , η_c^* and C_c^* are respectively the viscosity and elastic coefficients reported by Naili *et al.* (2010) for the cortical bone, and f is the frequency.

2.3.2.2 Heterogeneous distribution of bone properties

The heterogeneous nature of the biomechanical properties of cortical bone tissue was adapted from the experimental results obtained by (Sansalone *et al.*, 2010). In order to properly sim-

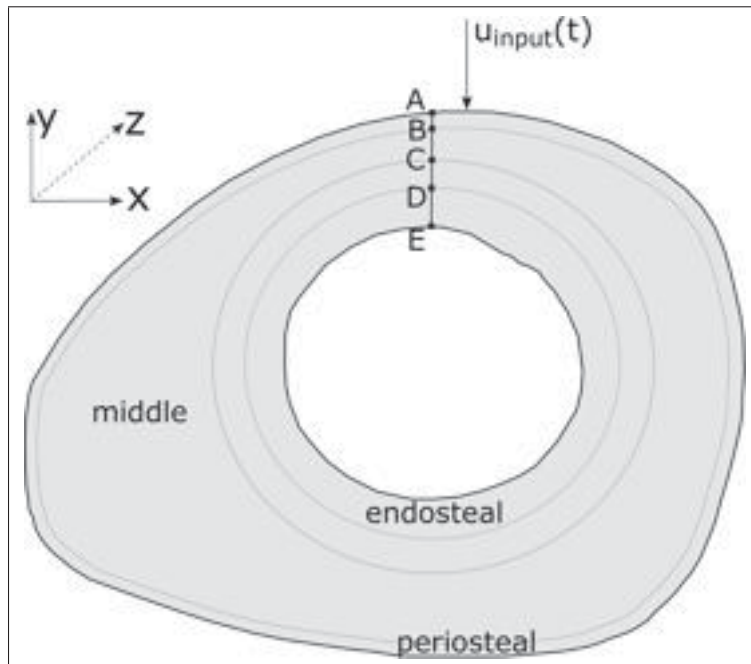


Figure 2.2 Cross-section taken from the middle of the radius bone and used for the SAFE analysis. Different regions were defined along the radial direction: periosteal (A-B), middle (B-C) and endosteal (D-E) regions.

plify the spatial distribution of each material property, the original values (Sansalone *et al.*, 2010) were adapted by choosing three different constant values for the periosteal (between A and B), middle (between B and C) and endosteal (between D and E) regions, as shown in Figure 2.3a for the coefficient C_{11} . Moreover, a linear variation was assumed in the region between the middle and periosteal bones (between C and D in Figure 2.2). For the density, the same approach was applied based on the distribution of porosity reported in the study. The conversion was made considering a scale where 0% of porosity denotes a bone density value of 1850 kg/m^3 and 100% of porosity denotes a bone density value of 1000 kg/m^3 . The constant values and the linear variation of each material property were chosen to minimize the gap between the original (Sansalone *et al.*, 2010) and simplified values. Figure 2.3b shows the simplified distribution defined for each coefficient and density. In order to model the evolution of the physiopathological condition varying from healthy to osteoporotic, each material property was defined with different values for the endosteal region (between D and E in Figure 2.2).

The "Osteoporotic" condition (identified as IX in what follows) was defined with the simplified distribution taken from the original data (Sansalone *et al.*, 2010). This assumption was made because the data were obtained from an osteoporotic 79-year old patient. The "Healthy" condition (numbered I next) was obtained by i) arbitrarily increasing the value of all stiffness coefficients and densities in the endosteal region by 20% and ii) by reducing the length of the endosteal region by an amount of 20%. These differences between healthy and osteoporotic conditions reflect the fact that early osteoporosis is known to be associated with endosteal resorption. Once the "Osteoporotic" and "Healthy" conditions were defined, seven intermediate distributions (identified as II to VIII) were considered in order to mimick the evolution of the osteoporotic state. This procedure resulted in a total of nine distributions, as shown in Figure 2.4, for the elastic constant C_{11} . This approach constitutes a simple way of modeling the gradual degradation of intracortical bone properties due to early stage osteoporosis. Table 2.1 shows a summary of the "Healthy" and "Osteoporotic" material properties used to defined the scenarios investigated numerically in this work.

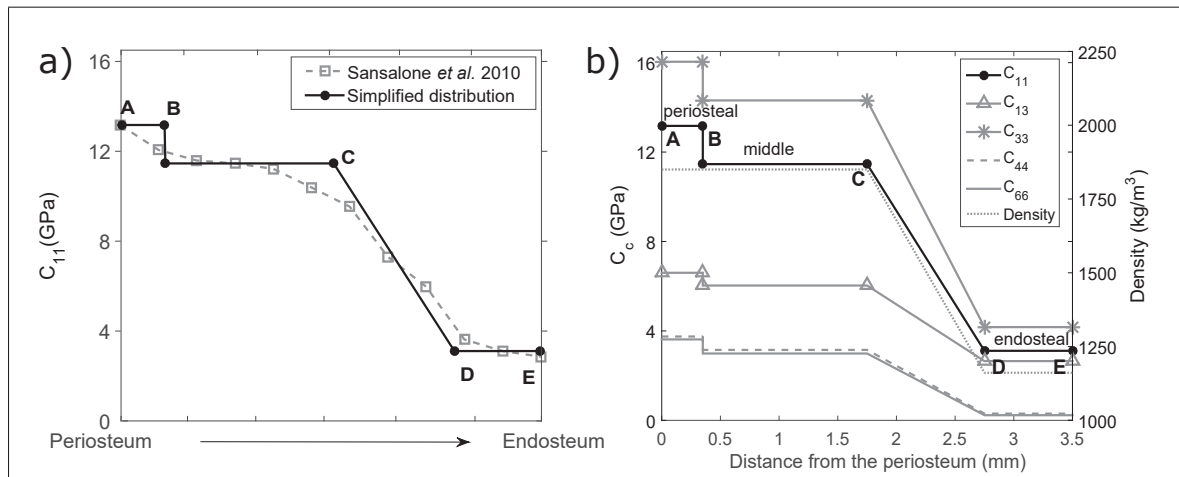


Figure 2.3 a) Original and simplified distribution of C_{11} varying from the periosteum to endosteum b) Elastic coefficients and density varying with the distance from the periosteum.

Table 2.1 Summary of the properties used to model cortical bone. The real part of the stiffness coefficients was adapted from the experimental results obtained by (Sansalone *et al.*, 2010). The imaginary part was adapted from the results used by (Naili *et al.*, 2010), applying equation 2.9.

Properties ^a	Periosteal (A-B)	Middle (B-C)	Endosteal (D-E)	
			I-Healthy*	IX-Osteoporotic
C_{11} (Pa)	$13.17e9 + 94.95fi$	$11.46e9 + 82.62fi$	$4.78e9 + 34.46fi$	$3.11e9 + 22.42fi$
C_{13} (Pa)	$6.60e9 + 91.74fi$	$6.03e9 + 83.81fi$	$3.32e9 + 46.14fi$	$2.65e9 + 36.83fi$
C_{33} (Pa)	$16.04e9 + 109.2fi$	$14.31e9 + 97.45fi$	$6.19e9 + 42.15fi$	$4.17e9 + 28.39fi$
C_{44} (Pa)	$3.75e9 + 14.70fi$	$3.15e9 + 12.34fi$	$0.87e9 + 3.41fi$	$0.30e9 + 1.17fi$
C_{66} (Pa)	$3.62e9 + 14.19fi$	$2.99e9 + 11.72fi$	$0.78e9 + 3.05fi$	$0.23e9 + 0.90fi$
Density (kg/m ³)	1850.00	1850.00	1299.04	1161.30

^a Defined as a complex number by $C_c + \eta_c fi$.

* The "Healthy" condition was defined based on an arbitrary increase of the value of all stiffness coefficients and density by 20%.

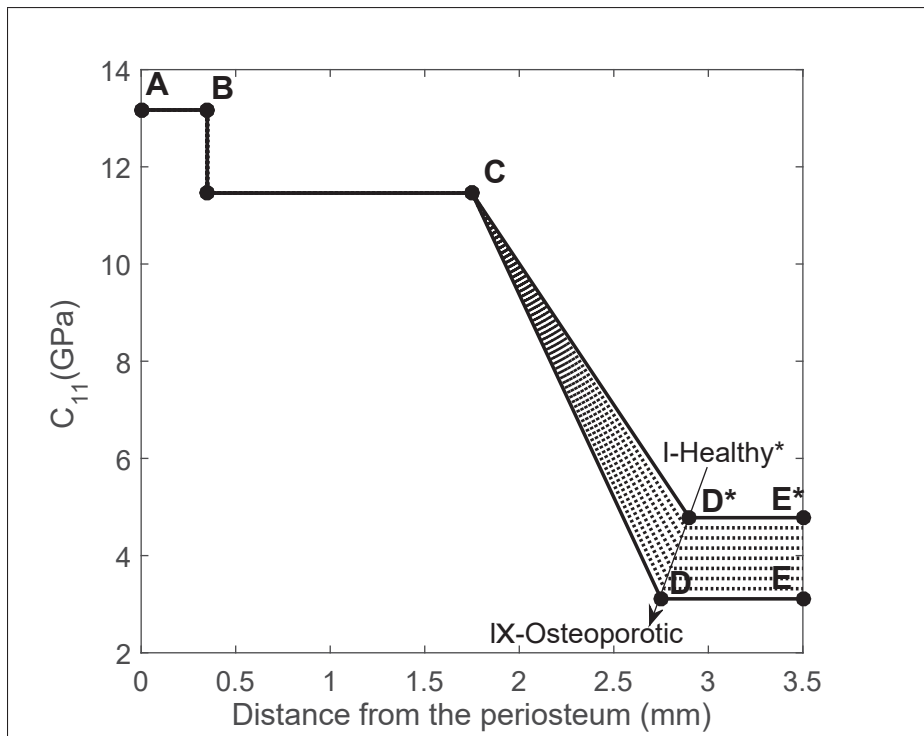


Figure 2.4 Nine different heterogeneous distributions defined between the "Healthy" and "Osteoporotic" conditions.

2.4 Results and discussion

2.4.1 Validation of SAFE simulations

Figure 2.5a and 2.5b show the 2D-FFT maps obtained by the FEM and SAFE methods, respectively. The gray lines show the dispersion curves obtained by SAFE. The intensities obtained for both simulation methods are consistent with the dispersion curves obtained by SAFE. Furthermore, the distributions of the intensities in the maps are similar for both methods, which constitutes a validation of the SAFE approach. Figs. 2.6a and 2.6b show the normalized time domain signal recorded at 150 mm for the simulation performed using FE and the SAFE methods, respectively. The signals of both methods are similar, especially at their beginning, where the FAS velocity is calculated. A few discrepancies can be observed at the end of the signal, which may be associated with the ultrasonic waves traveling in the circumferential direction due to the point excitation. The advantage of the SAFE method as compared to finite element modeling is that with SAFE, only the cross-section is modeled and meshed, resulting in computationally efficient simulations. For example, one simulation using the FE method required approximately 5.5 hrs and 2.5 Gb of memory while to obtain an equivalent signal using the SAFE method required around 4 hrs and 1.4 Gb of memory. Even though the advantages of SAFE in term of resources requirements are modest, once the dispersion curves are calculated, the propagated responses can be computed for different excitation configurations without running the simulations again, which may represent a significant gain for large parametric studies. Furthermore, the simulations can be performed separately mode by mode, as shown Figure 2.6c, where only the four modes with the highest amplitude were computed. The flexibility of the SAFE method may lead to a better understanding of the contribution of each mode to the signal. However, the waveguide is assumed to have constant cross-sectional properties along the axial direction.

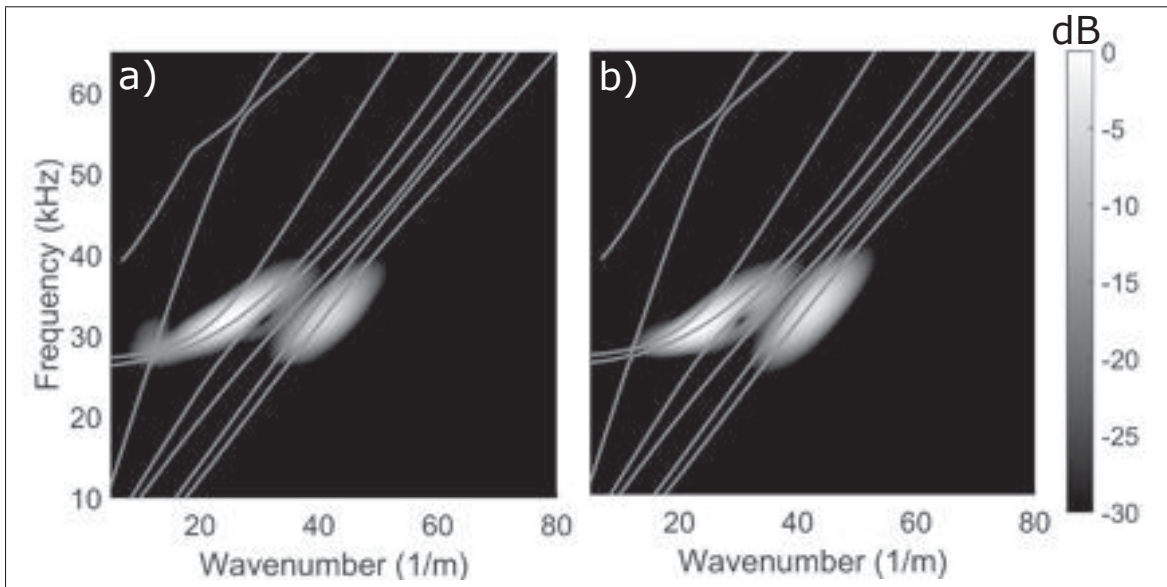


Figure 2.5 Time-domain signal obtained at 150 mm of propagation distance using: a) FE simulations; b) SAFE simulations showing the signal containing all modes; c) SAFE simulations showing the signal of each mode separately.

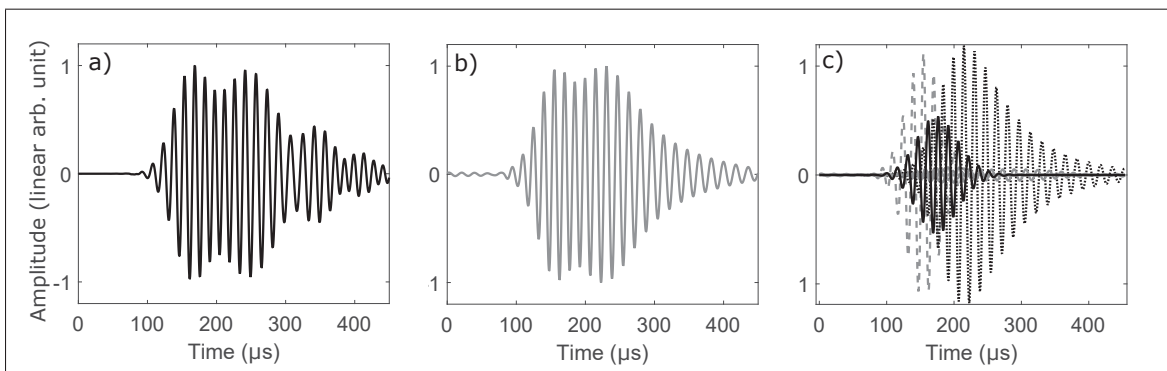


Figure 2.6 Time-domain signal obtained at 150 mm of propagation distance using: a) FE simulations; b) SAFE simulations showing the signal containing all modes; c) SAFE simulations showing the signal of each mode separately.

2.4.2 Dispersion curves of cortical bone

Figure 2.7 shows the velocity dispersion curves obtained with a "Healthy" and "Osteoporotic" cortical bone properties (condition I and IX, respectively). Due to the modification of the waveguide properties, a variation in the mode velocity at several regions of the dispersion

curves was obtained. However, the interpretation of these dispersion curves in the context of an axial transmission measurement using FAS is difficult because the FAS velocity behavior is associated to a combination of different modal properties of the waveguide (velocity, excitability and attenuation) as well as the input signal used to perform the excitation. For that reason, the FAS velocity cannot be predicted using only the phase velocity taken from the dispersion curves. However, simulating the temporal synthetic signals (combining velocity, excitability and attenuation dispersion curves) is an efficient way of modeling and understanding the FAS velocity.

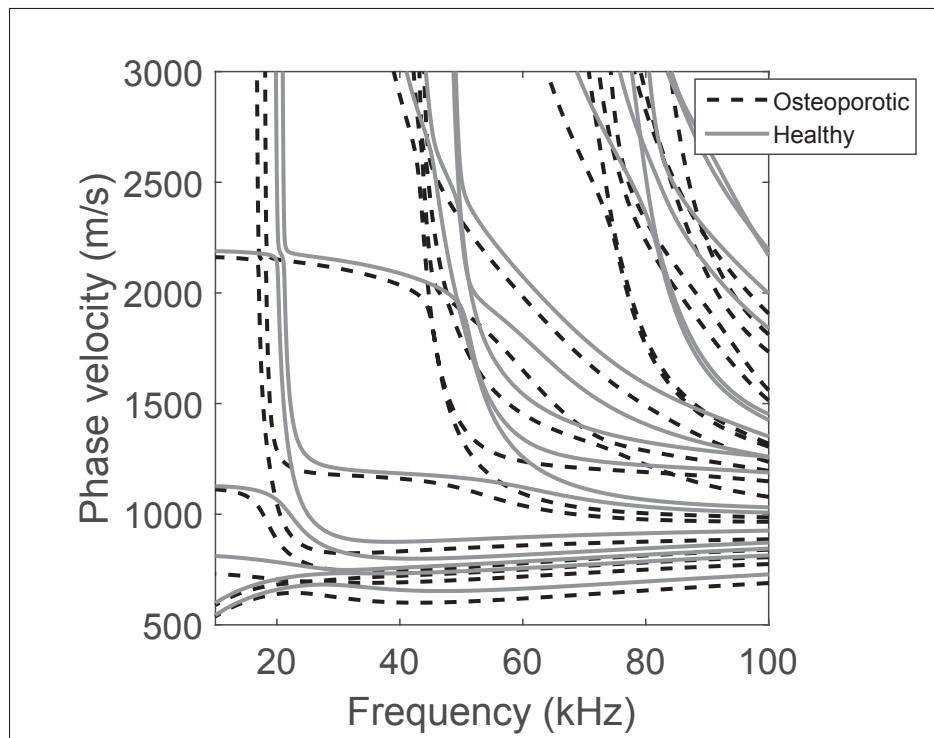


Figure 2.7 Phase velocity dispersion curves of the simulated modes obtained with "Healthy" and "Osteoporotic" waveguide condition.

Figure 2.8a shows the group velocity dispersion curves obtained with a "Healthy" cortical bone waveguide (condition I). Eight ultrasonic guided wave modes were identified in the 10-60 kHz frequency range, with group velocities varying between 0 and 2200 m/s. The dotted line shows the frequency spectrum of the excitation waveform used to simulate the signal in the time

domain. The 6dB bandwidth is concentrated between 25 kHz and 40 kHz. Figure 2.8b and 2.8c show, respectively, the attenuation and excitability dispersion curves used to compute the time-domain signal for the "Healthy" condition.

The simulated signals obtained from this dispersion curve consist of the superposition of propagated responses of each mode. One advantage of the semi-analytic approach is that it allows the simulation of only the selected modes, which can lead to a better understanding of the contribution of each mode to FAS velocity. Such a mode contribution cannot be easily resolved using conventional finite element modeling.

Figure 2.8d shows the time domain signal obtained for each mode separately and all modes together, for the "Healthy" condition. It is worth noting that at time t_3 , the amplitude contributions of the modes $m=1, 3, 4$ and 5 are substantially higher as compared to the amplitudes of modes $m=2, 6, 7$ and 8 . This result suggests that the high amplitude modes tend to affect the FAS velocity to a lesser degree since the FAS velocity is measured in this part of the signal. However, the influence of the modes on the FAS velocity along the different scenarios will be investigated in the following section.

2.4.3 Effect of properties on the FAS velocity

Figure 2.9 shows the calculated FAS velocity when different combinations of modes are considered. The dashed line shows the results obtained when all the modes are taken into account. The dashed line with stars shows the results obtained when considering the three dominant modes observed in Figure 2.8 ($m=1, 4$ and 5). Between scenarios I and V, the values of the computed FAS velocity are significantly different as compared to the combination including all modes. The discrepancy is related to the fact that the amplitude contribution of mode $m=3$ decreases as we go from scenario I to scenario V as shown in Figure 2.10a. This suggests that mode $m=3$ affects the FAS velocity for scenarios I to V. Thus, the solid line with circles shows the results when taking into account modes $m=1, 3, 4$ and 5 . The variation of the FAS velocity as a function of the physiopathological state matches the results obtained when considering

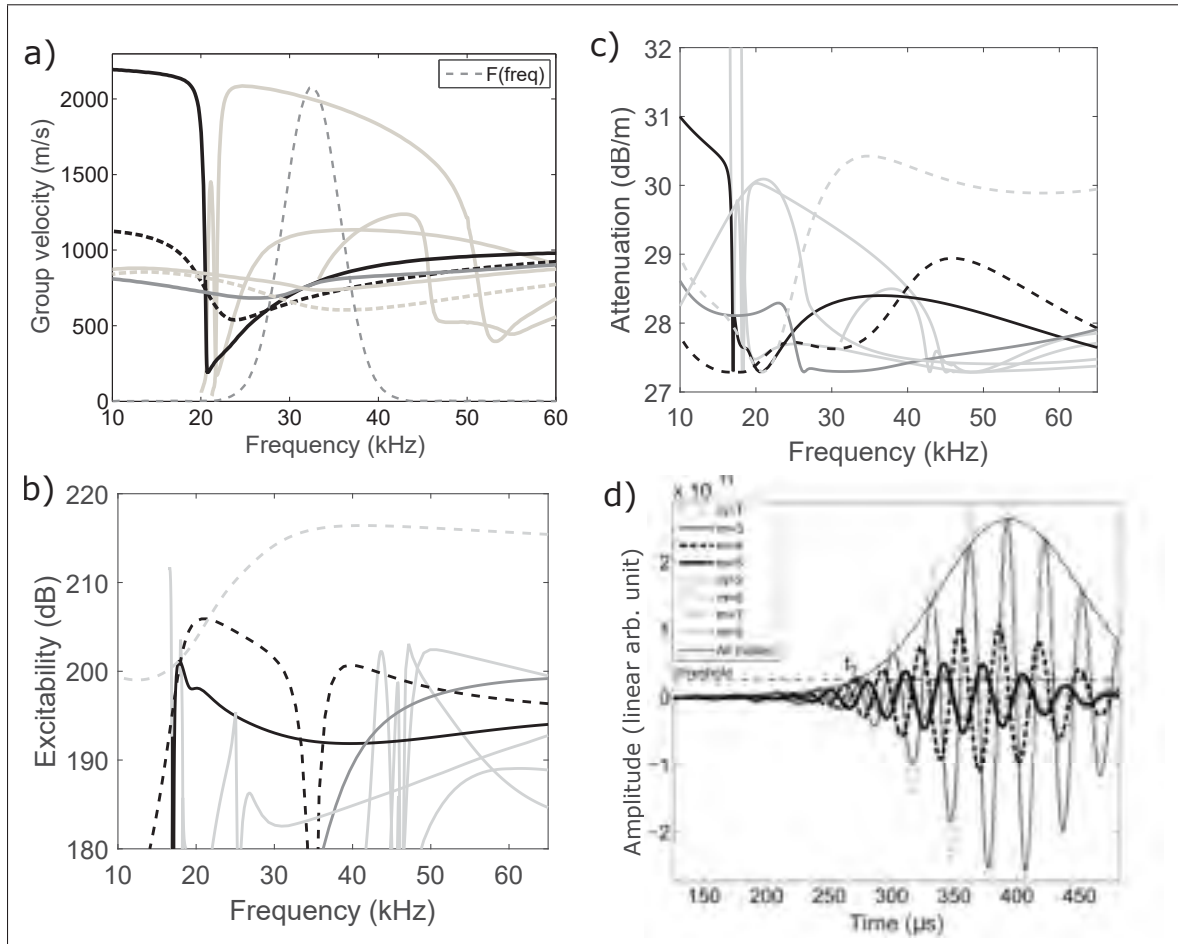


Figure 2.8 Dispersion curves obtained for the "Healthy" condition a) Group velocity superposed with the frequency bandwidth of the input signal; b) Attenuation; c) Out-of-plane excitability; d) Time-domain signal obtained for the SAFE simulation, showing each mode separately and all modes together for the "Healthy" condition. The legend in Figure 2.8d is applied to Figure 2.8a, 2.8b, and 2.8c.

all modes for all scenarios (see Figure 2.9b). Therefore, combining modes $m=1, 3, 4$ and 5 constitutes a good approximation that can be used to mimic the complete signal, which will facilitate the interpretation of the results.

Figure 2.10a shows the amplitude contribution of modes $m=1, 3, 4$ and 5 , varying separately from the "Healthy" to the "Osteoporotic" condition. Similarly, Figure 2.10b shows the group velocity of each mode separately and the FAS velocity varying with the same scenarios. The

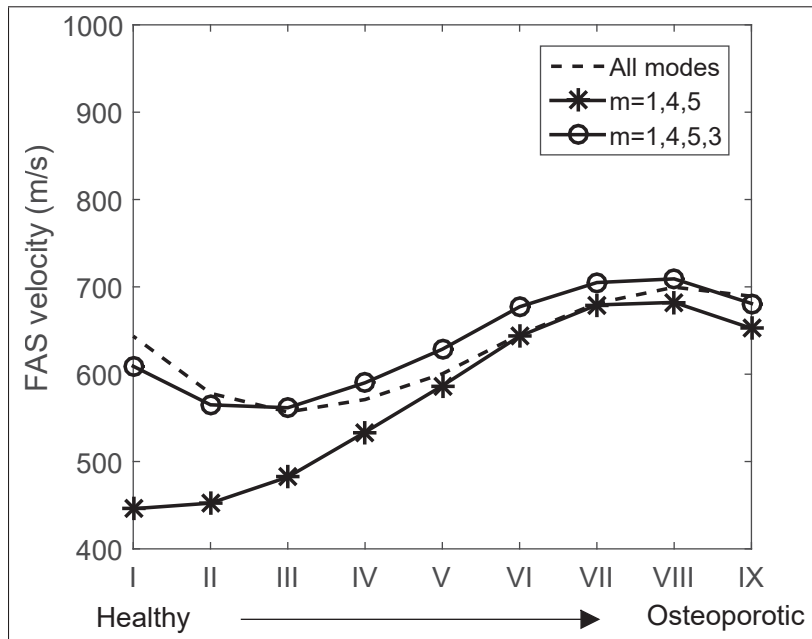


Figure 2.9 FAS velocity obtained using the combinations of different modes.

group velocity was taken from the dispersion curves at 32.5 kHz and the FAS velocity simulated considering the combination of modes $m=1, 3, 4$ and 5 .

A decrease is observed for the FAS velocity at the beginning (from scenarios I to III), followed by an increase in the intermediate scenarios (from III to VIII) and, again, a decrease at the end (from VIII to IX). Such non-linear behavior is not desirable in a clinical measurement since a given measured FAS velocity can be associated with more than one scenario. However, this phenomenon is expected since the amplitude contribution of each mode is changing along the different scenarios. Indeed, the variations of the FAS velocity cannot be associated with the group velocity of a single mode. The FAS velocity tends to follow the group velocity of the higher contribution modes. However, due to the competition between the modes with the higher contribution, the FAS velocity switches its velocity from mode to mode with the different scenarios.

For example, between scenarios I and III, the FAS velocity has a value similar to mode $m=1$ (Figure 2.10b). This is consistent with the fact that the mode $m=1$ has the highest amplitude

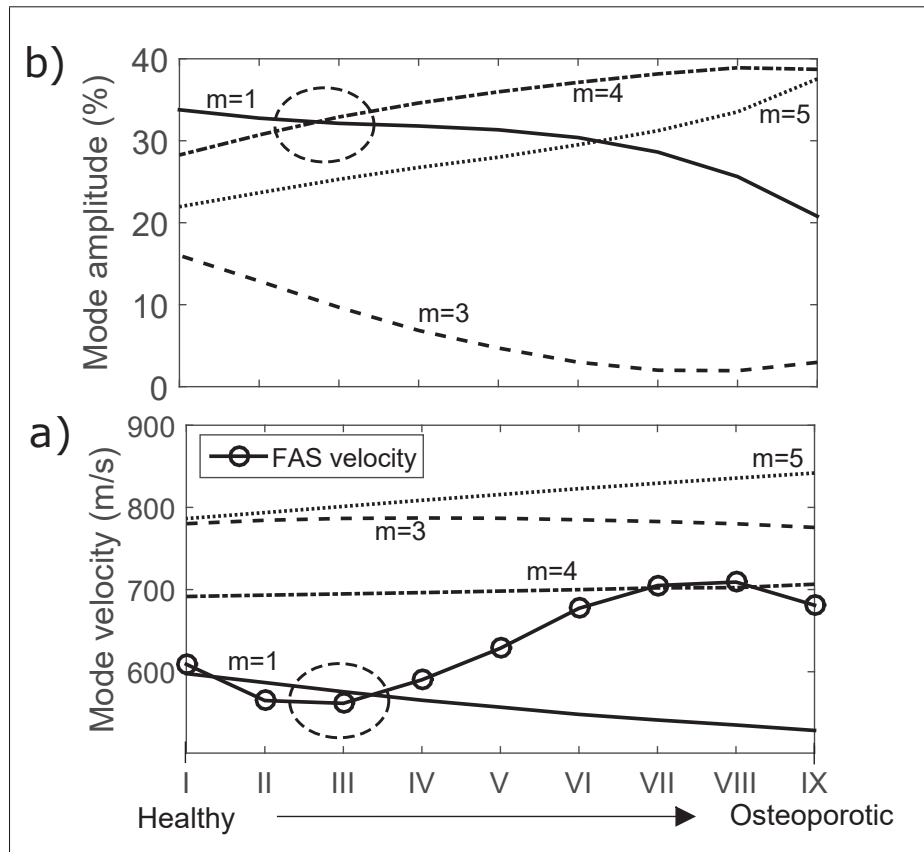


Figure 2.10 a) Amplitude contribution of the four main modes separately, varying with the scenarios; b) Group velocity of each of the four modes separately and FAS velocity (simulated considering four of the modes) varying with the scenarios. The circles show the change of the mode with the highest amplitude contribution (from $m=1$ to $m=4$).

contribution in this range (Figure 2.10a). Then, from scenarios III to VIII, the FAS velocity switches its behavior and starts to increase. This is in accordance with the change of the mode with the highest amplitude contribution (from $m=1$ to $m=4$), as indicated by the circles in Figure 2.10a. Then, from scenario VI to VIII, the FAS velocity has a similar value as mode $m=4$. Again, mode $m=4$ has a substantially higher amplitude contribution compared to the other modes in this range.

However, although the FAS velocity could be associated with the high contribution mode velocities, a completely unexpected behavior of the FAS velocity was found for some scenarios

(from IV to VI). Such an unexpected behavior may be due to the constructive and destructive interference between the modes for certain scenarios.

2.4.4 Limitations of the study

The 2D trilayer model investigated in this study using the SAFE method did not account for the impacts of structural irregularities along the axial direction since the waveguide is assumed to be constant and infinite. Such structural features can change the signal of guided waves propagation in bone tissue, and consequently, modify the effect of bone status on the FAS velocity. However, this limitation is mitigated by the fact that the bone properties are measured in the central region of the bone, where the assumption of a constant profile along the axial direction holds. Despite the lack of experimental data, the predictions obtained have shown results in good agreement with conventional 3D finite element simulations.

The influence of the heterogeneous nature of the biomechanical properties of realistic cortical bone geometry was analyzed with respect to the FAS velocity. The heterogeneous distribution of cortical bone properties applied in this study was based on homogenized local material properties applied by Sansalone *et al.* (2010), which are not easy to define due to the multi-scale nature of bone and its dependence on the microstructure at smaller scales. Furthermore, approximations were employed in order to determine the value and the distributions of stiffness coefficients adapted from (Naili *et al.*, 2010) and (Sansalone *et al.*, 2010) by choosing constant values and linear variations to describe the variation along the radial direction. However, such discrepancies tend to be minimized by using low-frequencies excitation since the large wavelength characteristic of the low-frequencies excitation performed in this work tends to be less sensitive to minor variations in the distribution.

Another limitation of this study is that the physiopathological condition was defined based on an evolution from arbitrarily extrapolated "Healthy" values to the original "Osteoporotic" data. More complex variations in material properties are expected for real bone degradation. This approach provides a simple way of modeling the gradual degradation of intracortical

bone properties, which may be due to the aging and/or early stage osteoporosis. It would be beneficial for the study to adapt the scenarios to a more realistic degradation condition by using appropriate homogenization procedures.

2.5 Conclusion

It has been shown that the propagation of guided waves using axial transmission configurations can be simulated using the SAFE method. The 2D-FFTs maps obtained for simulations using the SAFE and 3D FE methods showed comparable results. For the assessment of intracortical bone properties, eight guided wave modes were found to be propagating as a result of an excitation in the 25-40 kHz frequency range. However, only four modes showed a substantial influence on the propagated signal and, consequently, a major impact on the FAS velocity. The calculated FAS velocity was shown to be associated with the velocity of the mode with the highest amplitude contribution. However, due to the change between the modes with the greater contribution, the FAS velocity was shown not to be a good discriminator of intracortical bone properties. This method can now be used to study the possibility of targeting specific modes by performing the excitation at different orientation on the bone surface, as well as to investigate different receiver array configurations through more advanced signal processing methods.

CHAPTER 3

EFFECT OF INTRACORTICAL BONE PROPERTIES ON THE PHASE VELOCITY AND CUT-OFF FREQUENCY OF LOW-FREQUENCY GUIDED WAVE MODES (20-85 KHZ)

Daniel Pereira^{1 4}, Guillaume Haiat^{1 2}, Julio Fernandes^{3 4}, Pierre Belanger^{1 4}

¹ Département de Génie Mécanique, École de Technologie Supérieure,
1100 Notre-Dame Ouest, Montréal, Québec, Canada H3C 1K3

² Centre National de la Recherche Scientifique, Laboratoire Modélisation et Simulation
Multiechelle, 61 avenue du Général de Gaulle, Cretéil Cedex, 94010, France

³ Department of Surgery, Université de Montréal, 2900 Boulevard Edouard-Montpetit,
Montreal, Quebec, H3T1J4 Canada

⁴ Centre de recherche l'Hôpital du Sacré-Coeur de Montréal, 5400 Boul Gouin O, Montreal,
Quebec, H4J1C5 Canada

Paper submitted to *The Journal of the Acoustical Society of America*, July 2018. First round of reviews completed, September 2018.

Abstract The assessment of intracortical bone properties is of interest since early-stage osteoporosis is associated with resorption in the endosteal region. However, understanding the interaction between ultrasonic guided waves and the cortical bone structure remains challenging. The purpose of this work is to investigate the effect of intracortical bone properties on the ultrasonic response obtained at low-frequency (<100 kHz) using an axial transmission configuration. The semi-analytical finite element method was used to simulate the propagation of ultrasonic guided waves in a waveguide with realistic geometry and material properties. An array of 20 receivers was used to calculate the phase velocity and cut-off frequency of the excited modes using the 2D Fourier transform. The results show that the position of the emitter around the circumference of the bone is an important parameter to control since it can lead to variations of up to 10 dB in the amplitude of the transmitted modes. The cut-off frequency of the high order modes was, however, only slightly affected by the circumferential position of the emitter, and was sensitive mainly to the axial shear modulus. The phase velocity and cut-off

frequency in the 20-85 kHz range are promising parameters for the assessment of intracortical properties.

Keywords: Ultrasonic guided waves, Intracortical, Low-frequency.

3.1 Introduction

Osteoporosis is associated with a reduction of the bone mass and microarchitectural bone deterioration, leading to a reduction in bone quality (Papaioannou *et al.*, 2004; Strom *et al.*, 2011; Giangregorio *et al.*, 2006) and to an increase in fracture risk (Con, 1991). Endosteal resorption of cortical bone results in an increase in bone porosity at the inner part of the cortical shell and in a reduction of the cortical bone thickness (Ritzel *et al.*, 1997). Dual-energy X-ray absorptiometry (DEXA), which is currently the gold standard for osteoporosis diagnostics (Kanis, 1994), nonetheless suffers from several limitations (Haba *et al.*, 2016; Gluer, 2008). Quantitative ultrasound (QUS) was developed to assess bone quality and has the advantage of being non-radiative, non-invasive and relatively cheap (Gluer, 1997). It, therefore, holds promise as a rapid screening method in a clinical setting. The mechanical nature of ultrasonic waves allows the technique to be used to retrieve the biomechanical properties of bone tissue (Kaufman & Einhorn, 1993). QUS techniques can be used to go beyond a simple estimation of the bone mineral density (Nicholson, 2008), which can be achieved with DEXA and which is not sufficient to assess fracture risk (Sur, 2004).

Bone QUS was initially developed in the context of trabecular bone characterization using transverse transmission devices (Stein *et al.*, 2013). However, the investigation of cortical bone (Rico, 1997) has attracted significant interest since about 80% of the skeleton is made of cortical bone, which supports most of the body load, and is involved in osteoporotic fractures (DG *et al.*, 1991). QUS using axial transmission techniques have mostly been used to study the cortical bone quality (Haiat *et al.*, 2011). Cortical bones, such as the radius or the tibia, constitute suitable waveguides for the propagation of ultrasonic guided waves, as was shown in various studies, including for instance (Haba *et al.*, 2016; Gluer, 2008, 1997). Ultrasonic

guided waves have the advantage of being sensitive to both the mechanical and geometrical properties of cortical bone (Yeh & Yang, 2011; Rozental *et al.*, 2013; Muller *et al.*, 2005).

Most studies focusing on the assessment of cortical bone properties using axial transmission consider plate or cylinder waveguides (as an approximation of the actual bone geometry) to simplify the interpretation of ultrasonic responses obtained numerically or experimentally (Minnozio *et al.*, 2015; Xu *et al.*, 2016; Kilappa *et al.*, 2015). Recently, more comprehensive numerical approaches were explored with the aim of improving the realism of the effect of cortical bone features on the axial transmission propagation expected *in vivo*. Bossy *et al.* (2004) performed three-dimensional (3D) finite difference simulations on geometries derived from a human radius tomography image to evaluate the effect of bone curvature, anisotropy, and micro-porosity on the first arriving signal (FAS) velocity. However, the actual anatomical variations of bone biomechanical properties were not taken into account and more emphasis was brought to the analysis of numerical simulations performed with idealized 3D objects (tubes and semi-infinite hemicylinder geometries). Moilanen *et al.* (2007a) developed a 2D numerical bone model to investigate the impact of realistic bone geometry specimens on the ultrasonic cortical thickness evaluation using plate assumptions. Haiat *et al.* (2009) and Naili *et al.* (2010) assessed the effect of the heterogeneous nature of cortical bone on the axial transmission response at 1 MHz in the context of an anisotropic material by using 2D finite element (FE) simulation on a plate model. More recently, Chen & Su (2014) proposed a quantitative compensation for the effect of soft tissues based on an *in vitro* calibration, which facilitates the development of high-precision measurements of ultrasonic guided wave modes. Moreau *et al.* (2014) introduced a modified method to predict the dispersion curves of an isotropic plate waveguide with a linearly varying thickness along the propagation direction. The enhanced model allows the detection of the mode's wavenumbers more accurately in the context of the formulation of inverse problems. However, despite the improvements achieved so far concerning the modeling of cortical bone, a more detailed numerical study remains needed to explain the influence of the cross-sectional curvature and distribution of properties in the radial direction on the propagation of ultrasonic guided waves at low frequencies.

Low-frequency (typically below 200 kHz) axial transmission research (Sarvazyan *et al.*, 2009; Kilappa *et al.*, 2011; Egorov *et al.*, 2014; Tran *et al.*, 2015) demonstrated that ultrasonic guided waves are sensitive to changes in bone properties, such as cortical thickness and porosity. Muller *et al.* (2005) introduced low-frequency axial transmission as a promising method for assessing the cortical thickness. Tatarinov *et al.* (2005) showed the potential of low frequencies (≈ 100 kHz) in assessing changes of deep underlying spongy layers in bovine tibia. More recently, Kilappa *et al.* (2015) reported an improved performance of fundamental flexural modes used to assess cortical bone thickness using phase-delayed excitation at very low-frequency (50 kHz). Kassou *et al.* (2017) investigated the feasibility of dry point-contact transducers to infer the thickness of the *in-vivo* subjects in the 50-150 kHz frequency range. Operating at low-frequency offers the advantage of a lower attenuation as well as a reduced number of generated modes, which simplifies the signal analysis. In addition, low-frequency ultrasonic guided wave modes tend to achieve greater penetration depths as compared to high-frequency. As a consequence, the sensitivity to variations in intracortical bone properties could be improved when using low-frequencies, which is relevant to assess early stages of osteoporosis. Notwithstanding the remarkable level of realism that has been introduced in simulations over the past few years, the physical interaction between low-frequency ultrasonic guided waves and the cortical bone structure remains unexplored because the cortical bone has i) a complex cross-sectional geometry and ii) a heterogeneous distribution of material properties along the circumferential direction.

In a previous study by our group (Pereira *et al.*, 2017), the propagation of ultrasonic guided waves in an irregular, multi-layer and heterogeneous bone cross-section modeled with anisotropic and viscoelastic material properties was investigated. The effect of the intracortical bone properties was then evaluated using the first arriving signal (FAS) velocity obtained from only five receivers. However, due to the interaction between several modes around the FAS, the velocity associated with the FAS was shown to be a poor discriminator of the intracortical bone properties. The goal of this paper is therefore to determine the effect of intracortical bone properties on the phase velocity and cut-off frequency of low-frequency ultrasonic guided wave modes

using an array of receivers, as well as a time-spatial frequency analysis technique instead of the FAS velocity. In order to do so, the excitation was generated by an emitter while the acquisition was performed in the time domain by an array of 20 receivers equally spaced along the bone surface. The bone ultrasonic responses were converted into the frequency domain using the two-dimensional Fourier transform (2D-FFT) in order to obtain the phase velocity and cut-off frequency of the propagating modes. Therefore, in this paper, the individual contribution of each viscoelastic coefficient and of the density were evaluated separately. The originality of this study when compared to our previous publication also lies in the application of the excitation source at different positions on the bone surface. This leads to a more comprehensive understanding of the physical interaction between the cortical bone curvature and the excitability of low-frequency ultrasonic guided wave modes.

The paper is organized as follows: section 3.2.1 introduces the semi-analytical finite element (SAFE) method used to simulate the signal of ultrasonic guided waves propagation in an arbitrary cross-section waveguide; section 3.2.2 describes the emitter/receivers configuration used to measure the ultrasonic responses on the bone surface in order to compute the *frequency vs. wavenumber* diagram. This section also describes the procedure employed to derive the phase velocity and cut-off frequency from the measured diagrams. In section 3.2.3 and 3.2.4, the cross-sectional geometry of the cortical bone model and the methodology used to define the distribution of properties along the radial direction are presented respectively. In section 3.3.1 and 3.3.2, the effect of the excitation position and the physiopathological condition on the phase velocity and cut-off frequency are presented, respectively. In addition, the individual contribution of each viscoelastic coefficient and density on the overall physiopathological conditions are presented in the section 3.3.3. Conclusion including potential clinical implications are presented in section 3.4.

3.2 Material and methods

3.2.1 Simulating time domain signals

The SAFE method has recently been used to simulate the modal properties of ultrasonic guided waves in bone systems (Thakare *et al.*, 2017; Nguyen *et al.*, 2017; Tran *et al.*, 2015; Nguyen & Naili, 2014). The computation of the time response from the modal properties of waveguides in an infinite arbitrary cross-section waveguide was previously described by Wilcox *et al.* (2001) and Loveday (2008). The resulting time domain signals consist in a linear superposition of the propagated response of each mode supported by the waveguide. A more detailed description of the implementation of the SAFE method can be found in the literature (Predoi *et al.*, 2007; Fan *et al.*, 2008c), while the detailed procedure used to generate the time domain signal, can be found in a recently published study (Pereira *et al.*, 2017).

The dispersive response of a given mode excited from a point source in the out-of-plane direction (radial direction r in Figure 3.1) can be calculated in the time domain using the following expression (Wilcox *et al.*, 2001):

$$u(t) = \frac{1}{2\pi} \int_{-\infty}^{+\infty} F(\omega) E(\omega) H_0^{(1)}(k(\omega) z_0) e^{-i\omega t} d\omega \quad (3.1)$$

$$i = \sqrt{-1} \quad (3.2)$$

where $u(t)$ is the surface out-of-plane displacement for a given mode as a function of time t , after propagating for an arbitrary distance z_0 . The factor $H_0^{(1)}$ is the zeroth-order Hankel function of the first kind and $F(\omega)$ is the frequency spectrum of a force input signal $u_{input}(t)$. The factor $k(\omega)$ is the mode wavenumber, defined by:

$$k(\omega) = k(\omega)_{real} + ik(\omega)_{imag} \quad (3.3)$$

where the real part denotes the propagating term and the imaginary part denotes the attenuation associated with the wavenumber. The term $E(\omega)$ is the frequency-dependent out-of-plane excitability of a given mode, and can be obtained with (Wilcox *et al.*, 2005):

$$E(\omega) = \frac{ik(\omega)\omega}{8} \left(\frac{u_{out}(\omega)^2}{P_z(\omega)} \right) \quad (3.4)$$

where $P_z(\omega)$ is the total power flow in the z -direction associated with the mode-shape as a function of the angular frequency, and $u_{out}(\omega)$ is the out-of-plane displacement on the surface of the mode-shape (at the position of excitation) as a function of the angular frequency. The dispersion curves of the waveguide (k , P_z and u_{out}) were obtained by solving the SAFE equations using the partial differential equation package in the COMSOL Multiphysics-4.4 and Matlab LiveLink environment. The complete time domain signal $u_{sum}(t)$ can then be obtained with the linear superposition of n modes supported by the waveguide as:

$$u_{sum}(t) = \sum_{m=1}^n u^m(t) \quad (3.5)$$

where $u^m(t)$ is the surface out-of-plane displacement associated with the m -th mode and n is the total number of modes supported by the waveguide. The advantage of the SAFE method as compared to other simulation methods such as 3D FE modeling is that with SAFE, only the cross-section is modeled and meshed, resulting in computationally efficient simulations, which may represent a significant gain of computation time. Furthermore, the dispersion curves are only calculated once using the SAFE method and then a number of time domain signals can be generated within minutes at minimal computational cost. The equivalent simulation using 3D FE would take hours, if not days, and use many times more memory (Pereira *et al.*, 2017).

The SAFE method can be considered an accurate tool for simulating the ultrasonic guided wave response. The method has shown results in agreement with 3D conventional FE simulations, as presented in our previous study (Pereira *et al.*, 2017). However, SAFE has the advantage of requiring reduced computing resources (e.g. 5.5 h and 2.5 Gb of memory against 4 h and 1.4 Gb of memory for the FE and SAFE methods respectively). Even though the advantages of SAFE in

terms of resource requirements are modest, it is worth noting that once the dispersion curves are calculated, the propagated responses can be computed for different excitation configurations without running the simulations again within seconds at minimal memory cost (<500 Mb).

3.2.2 Axial transmission configuration

The axial transmission configuration was modeled using the SAFE procedure described above. The waveguide consists of a 2D multilayer model composed of a viscoelastic heterogeneous solid layer surrounded by two viscoelastic homogeneous fluids. The solid layer corresponds to cortical bone while the two fluids correspond respectively to bone marrow and soft tissues. Because of the characteristics of the SAFE simulations, the multilayer 2D medium is assumed to have an infinite length along the axial direction, resulting in a 3D equivalent medium, as shown in Figure 3.1.

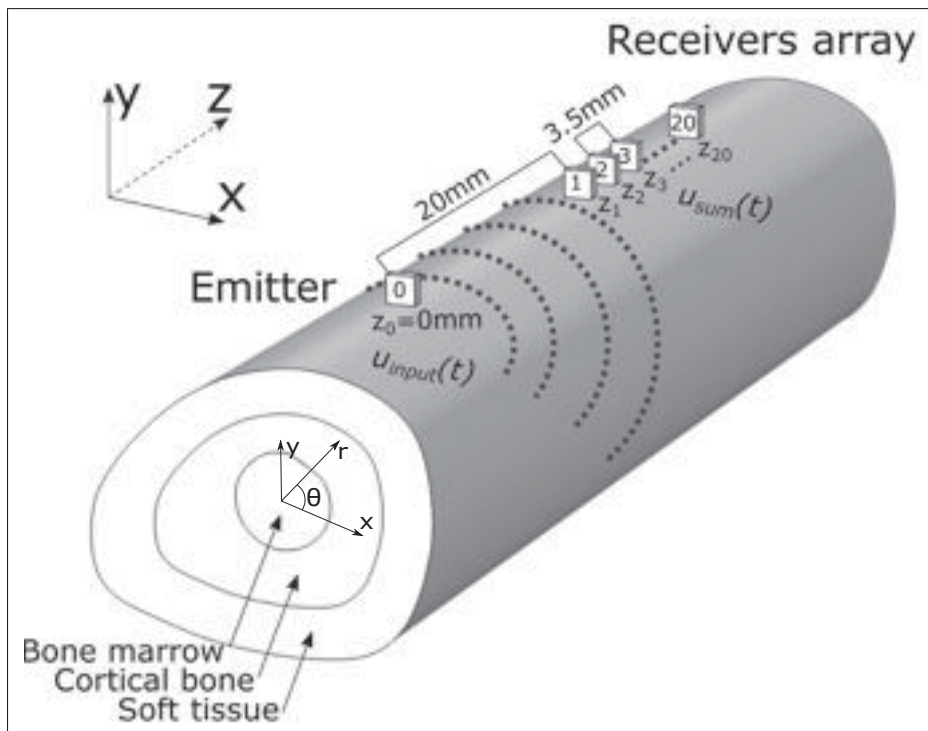


Figure 3.1 Schematic of the equivalent 3D axial transmission configuration used to perform the SAFE simulations.

The acoustic excitation was performed using a point source located in a plane denoted $z_0 = 0$ mm in contact with the upper part of the periosteal region of the bone cross-section. A 5-cycle Hann windowed toneburst centered at different frequencies between 20-85 kHz was used as the input waveform to perform the excitation. Eight different excitation positions around the circumference of the cortical bone were investigated in this study. The positions, identified with the letters "A" to "H" in Figure 3.2, were chosen based on the anatomical accessibility of a probe in a left human forearm. As a limitation of our study, the simulation of the excitability curves was conducted based on the displacement computed directly on the cortical bone tissue instead of on the overlying soft tissue (see Figure 2). The reason for this simplification is the higher mesh stability afforded by considering the displacement in the inner elements (cortical tissue) instead of in the outer elements (soft tissue). When considering the displacement on the cortical bone tissue instead of the overlying soft tissue, a negligible change in the excitability curves was observed. However, for modes traveling with most of the energy in the cortical layer (which is the case for the majority of modes investigated in this study), the effect of this assumption on the excitability curves is acceptable. As the wavelengths of the modes of interest are long relative to the soft tissue thickness, a very limited number of modes are traveling with significant energy in the soft tissue. For the modes traveling in the cortical layer, the excitability curves have shown similar shape for both cases so that the relative difference and the rank between modes remained the same. As a consequence, no significant change on the relative variation obtained for the phase velocity and cut-off frequencies in the sensitivity study is expected by modeling the waveguide with or without the soft tissue.

At reception, the out-of-plane displacements of the propagating waves were simulated at 20 positions (#1, #2, #3...#20 in Figure 3.1), denoting an array of 20 receivers. The acquisition array was rotated in accordance with the excitation position around the circumference in order to keep the emitter and the receivers aligned. The acquisition elements were separated from one another by a distance of 3.5 mm, while varied from $z = 20$ mm to $z = 90$ mm. The signals obtained were processed using the 2D-FFT in order to calculate the *frequency vs. phase-velocity* diagram (Alleyne & Cawley, 1990). Figure 3.3a shows typical received time domain signals

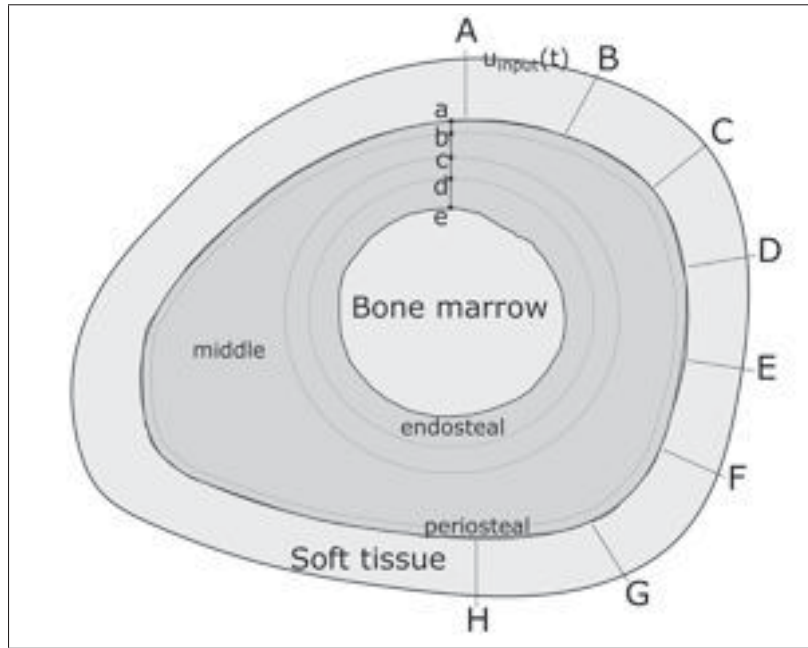


Figure 3.2 Cross-section of the middle of the radius bone used for the SAFE analysis. Different regions were defined along the radial direction: periosteal (a-b), middle (b-c) and endosteal (d-e) regions. The letters "A" to "H" show the eight different positions used to perform the excitation on the bone surface.

obtained for an excitation frequency centered at 45 kHz. Figure 3.3b shows the *frequency vs. phase-velocity* diagram obtained after performing the 2D-FFT.

For each diagram, the phase velocity of the low-order mode (named V_{ph}) was measured by taking the peak energy at the central frequency of the excitation waveform, as shown in the black square in Figure 3.3b. Similarly, the cut-off frequency of the higher-order mode (named $F_{cut-off}$) was measured by taking the peak of energy at a reference velocity equal to 4000 m/s (see black circle in Figure 3.3b). Those two features (V_{ph} and $F_{cut-off}$) were used to evaluate the performance of each configuration in terms of assessing the variations in the intracortical bone properties.

It should be noted that the 2D tri-layer model investigated in this study did not account for the impacts of structural or geometrical irregularities along the axial direction since the waveguide

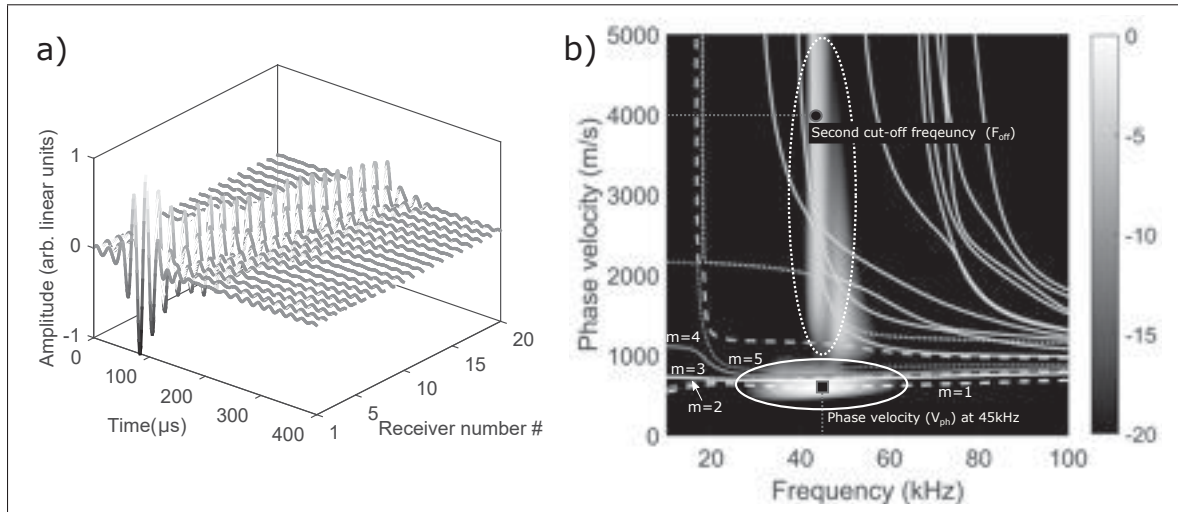


Figure 3.3 a) Simulated time domain signals obtained at each receiving position. b) Typical phase velocity vs. frequency diagram showing the intensity of the excited modes (dB scale) and the measured phase velocity V_{ph} and cut-off frequency $F_{cut-off}$. The white ellipsis show the two excited regions in the diagram.

was assumed to be constant and infinite. Such an assumption may change the propagation of ultrasonic guided waves in bone tissue. However, this limitation is balanced by the fact that the bone properties are typically measured in the central region of the bone, where the assumption of a constant profile along the axial direction holds because of the long wavelength in the frequency range used in this study.

3.2.3 Modeling cortical bone

The geometry of the waveguide was extracted from a slice of a human radius geometry. The radius geometry was provided by Sawbones (Sawbone - Pacific Research Laboratories, USA), and was built based on μ CT images of the human radius. In this work, the middle third region, which is composed only of cortical bone, was used. Moreover, bone-marrow was added inside the cortical shell, and a 3.5 mm layer of soft-tissue was added outside the cortical shell. The tri-layer cross-section was imported into the COMSOL Multiphysics environment for execution of the SAFE analysis. The mesh was built using triangular elements with a maximum size of 0.5 mm, subject to a constraint of at least 15 elements per wavelength. Bone marrow and soft tissue

were modeled as homogeneous viscoelastic fluids with the same properties used by Naili *et al.* (2010) (bulk modulus=2.25e9 Pa, bulk viscosity=1.97 Pa.s and density=1000 kg/m³), while the cortical bone was modeled as a viscoelastic transversally isotropic material. Furthermore, cortical bone was divided into three regions along the radial direction: periosteal (a-b), middle (b-c) and endosteal (d-e) regions (see Figure 3.2a). Each region was defined with different values for the transversally isotropic stiffness coefficients and density ($C_{11}, C_{13}, C_{33}, C_{44}, C_{66}$ and ρ), as summarized in Table 3.1. The values of each region were chosen based on a simplification of experimental results reported by Sansalone *et al.* (2010). A more detailed description of the distribution of the material properties along the radial direction is provided in the next section.

Table 3.1 Summary of the properties used to model cortical bone. The real parts of the stiffness coefficients were adapted from the experimental results obtained by Sansalone *et al.* (2010), while the imaginary parts were adapted from the results presented by Naili *et al.* (2010), using equation 3.7.

Viscoelastic coefficient ^b	Periosteal (a-b)	Middle (b-c)	Endosteal	
			Healthy (d*-e*)	Osteoporotic (d-e) ^b
C_{11} (Pa)	13.17e9 + 94.95 <i>fi</i>	11.46e9 + 82.62 <i>fi</i>	4.78e9 + 34.46 <i>fi</i>	3.11e9 + 22.42 <i>fi</i>
C_{13} (Pa)	6.60e9 + 91.74 <i>fi</i>	6.03e9 + 83.81 <i>fi</i>	3.32e9 + 46.14 <i>fi</i>	2.65e9 + 36.83 <i>fi</i>
C_{33} (Pa)	16.04e9 + 109.2 <i>fi</i>	14.31e9 + 97.45 <i>fi</i>	6.19e9 + 42.15 <i>fi</i>	4.17e9 + 28.39 <i>fi</i>
C_{44} (Pa)	3.75e9 + 14.70 <i>fi</i>	3.15e9 + 12.34 <i>fi</i>	0.87e9 + 3.41 <i>fi</i>	0.30e9 + 1.17 <i>fi</i>
C_{66} (Pa)	3.62e9 + 14.19 <i>fi</i>	2.99e9 + 11.72 <i>fi</i>	0.78e9 + 3.05 <i>fi</i>	0.23e9 + 0.90 <i>fi</i>
Density (kg/m ³)	1850.00	1850.00	1299.04	1161.30

^a Adapted from the experimental results obtained by Sansalone *et al.* (2010)

* The "Healthy" conditions were defined based on an arbitrary gain of 20% on the value of all stiffness coefficients and density.

In the viscoelastic model used in this study, the elastic stiffness constants were written as complex numbers:

$$C_c = C_c + \eta_c f i \quad (3.6)$$

where the subscripts $c=11, 13, 33, 44$ and 66 , and f corresponds to the frequency. The real part of the stiffness constants is assumed to be independent of the frequency, while the imag-

inary part results from the use of the linear theory of viscoelasticity, assuming frequency-dependent losses in the waveguide. Because relevant data were lacking, the viscosity coefficients $\eta_{11}, \eta_{13}, \eta_{33}, \eta_{44}$ and η_{66} shown in Table 3.1 were defined based on the viscosity coefficients found in the literature. The coefficients were adjusted by the ratio between the elastic coefficients used in this study and those reported in (Naili *et al.*, 2010), as given by:

$$\eta_c = \frac{C_c^*}{C_c} \cdot \eta_c^* \quad (3.7)$$

where the subscripts $c=11, 13, 33, 44$ and 66 , η_c^* and C_c^* are respectively the viscosity and elastic coefficients reported by Naili *et al.* (2010) for the cortical bone.

3.2.4 Heterogeneous distribution of bone properties

The heterogeneous nature of the biomechanical properties of cortical bone tissue was adapted from the experimental results obtained by Sansalone *et al.* (2010) using 3D synchrotron micro-computed tomography images (79-year old patient). In order to simplify the spatial distribution of each material property, the original values (Figure 3.4) were adapted by choosing three different constant values for the periosteal (between a-b), middle (between b-c) and endosteal (between d-e) regions. Moreover, a linear variation was assumed in the region between the middle and periosteal bone (between c-d). For the density, the same approach was applied based on porosity distribution reported in the study. The conversion was made considering a scale where 100% BV/TV (bone volume/ total volume) denotes a bone with a 1850 kg/m³ density and 0% BV/TV denotes only bone marrow with a 1000 kg/m³ density. The constant values, as well as the linear variation of each material property, were chosen to minimize the gap between the original (Sansalone *et al.*, 2010) and simplified values. Figure 3.4 shows the original and simplified (healthy and osteoporotic) distributions for the coefficient C_{11} .

Two different physiopathological conditions, namely "Healthy" and "Osteoporotic", were defined for the endosteal region (between d*-e* and d-e in Figure 3.4, respectively). The "Osteoporotic" condition was defined with the simplified distribution taken from the original data

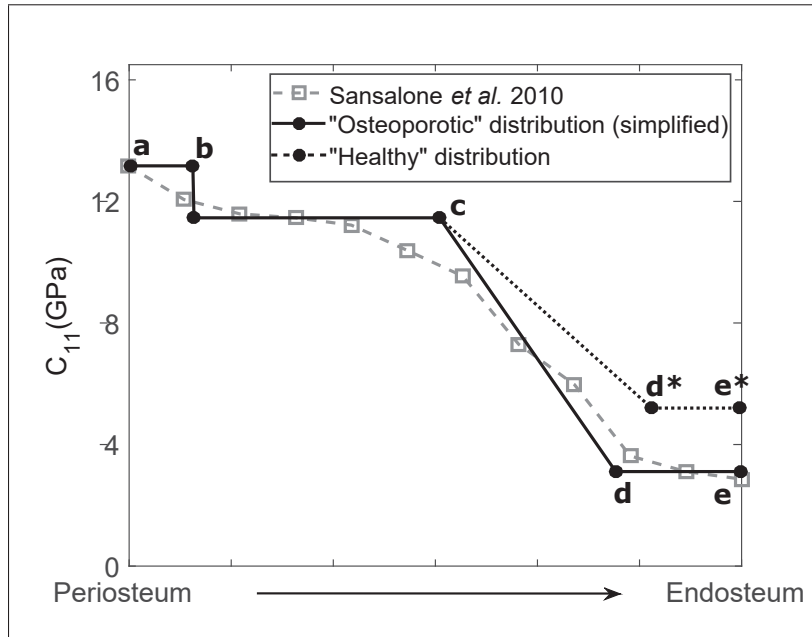


Figure 3.4 Simplified distribution of the elastic coefficients C_{11} varying with the distance from the periosteum for the healthy and osteoporotic condition.

(Sansalone *et al.*, 2010). This assumption was made because the data were obtained from an osteoporotic 79-year old patient. The "Healthy" condition was then obtained by: i) arbitrarily increasing the values of all stiffness coefficients and density in the endosteal region by 20%, and ii) by reducing the length of the endosteal region by 20%.

As a limitation, the approach used to model the "Healthy" condition constitutes a simple way of modeling a slightly less degraded condition, which does not necessarily represents the condition associated with a healthy patient. However, since the properties are changing only in the endosteal region in our sensitivity study, the magnitude of change between the "Healthy" and "Osteoporotic" condition can be considered very small, which may be similar to the magnitude of degradation associated to the early-stage osteoporosis.

Furthermore, the heterogeneous distribution of cortical bone properties applied in this study was based on homogenized local material properties applied by Sansalone *et al.* (2010), which are not easy to define due to the multi-scale nature of bone and its dependence on the mi-

crostructure at smaller scales. However, such discrepancies tend to be minimized by using low-frequency excitation associated with long wavelengths of the excited modes. Table 3.1 shows a summary of the "Healthy" and "Osteoporotic" elastic coefficients and densities used to defined the aforementioned scenarios.

3.3 Results and discussion

3.3.1 Effect of excitation position

Figures 3.5a to h show the normalized excitability curves (in the 10-100 kHz range) for an excitation performed at eight different positions on the bone surface (identified with letters "A" to "H" in Figure 3.2). The normalized excitability predicts the relative amplitude expected to be observed by a receiver when an emitter at position "A" applies a load in the radial direction (see Figure 3.2). The curves show the modal excitability of five modes with similar velocities ($m=1$, $m=2$, $m=3$, $m=4$, and $m=5$, marked with a solid line ellipse in Figure 3.3). A notable difference in the modal excitability can be observed between each configuration, which is expected for non-symmetric waveguides such as the bone geometry modeled in this study. For practical applications, a position that can mainly excite a single mode is preferable in order to avoid interferences from other modes.

Modes $m=1$, $m=2$, $m=3$, $m=4$, and $m=5$ all present flexural-like mode shapes. For instance, Figure 3.6a and 3.6b show the out-of-plane component of the fundamental flexural tube mode $F(1,1)$ and mode shape of $m=1$ respectively. Despite the similarities between the displacement fields and the mode order, a direct association to the mode shape of tubular waveguides is not possible due to the asymmetric nature of the waveguide and its arbitrary geometry

The modes $m=1$, $m=2$, and $m=3$ all show an excitability 10 dB higher than the other modes, as shown in the highlighted regions in Figures 3.5a, 3.5c, and 3.5h, respectively. Furthermore, according to Figure 3.7, the modes $m=1$, $m=2$, and $m=3$ have a higher percentage of the total power flow concentrated in the endosteal region as compared to the other modes, which

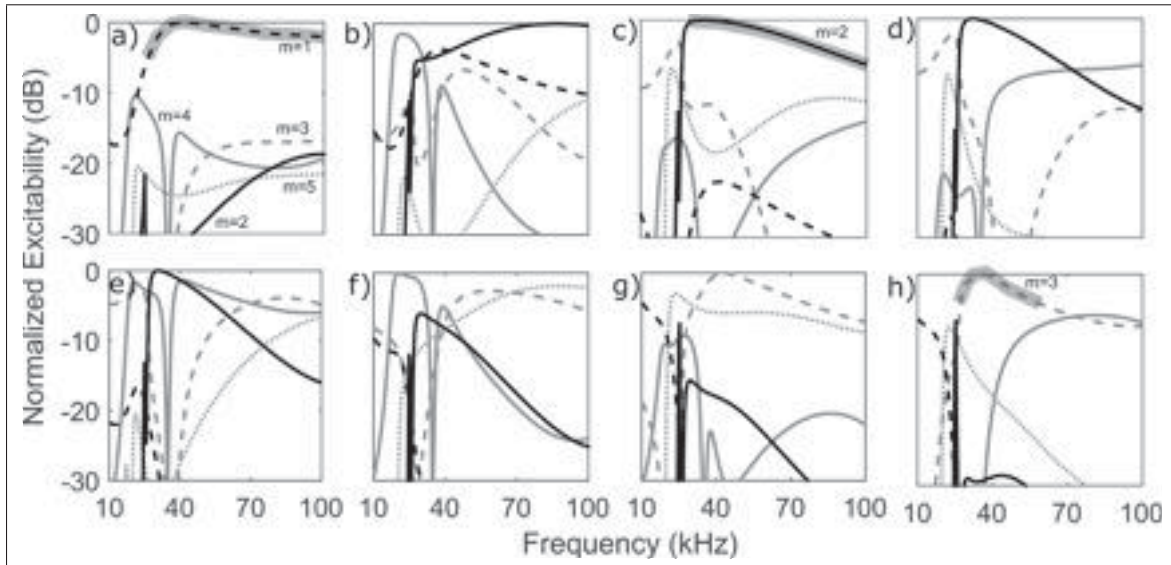


Figure 3.5 Normalized modal excitability obtained for the excitation performed at eight different position on the bone surface from 10 kHz to 100 kHz. The letters a) to h) are associated to the excitation position "A" to "H" shown in Figure 2, respectively.

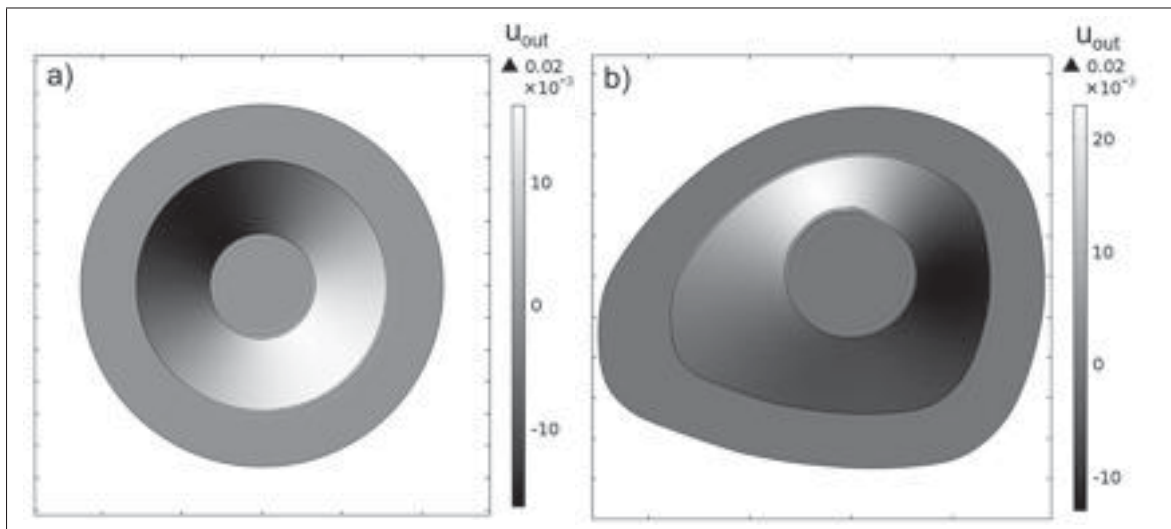


Figure 3.6 Out-of-plane displacement field (radial direction r in Figure 3.1) at 40 kHz for: a) fundamental flexural mode $F(1,1)$ on a tubular geometry waveguide and b) mode $m=1$ on a bone-like geometry waveguide. The highlighted regions denote modes segments that have an excitability 10 dB higher than the other modes.

indicates that they are likely to be sensitive to changes in this region. Thus, the excitation at position "A", "C" and "H" were chosen as the most suitable positions to excite a dominant mode; they were therefore further investigated in this paper. Since the attenuation of the modes is expected to be small at very low frequencies (<100 kHz), it was not taken into account to choose the most suitable excitation and detection positions

3.3.2 Effect of physiopathological conditions

Table 3.2 shows the percentage variation in the phase velocity (V_{ph}) and cut-off frequency ($F_{cut-off}$) for the excitation performed at position "A", "C" and "H". The variations were calculated based on the difference computed between the two physiopathological conditions ("Healthy" and "Osteoporotic"). The simulations were performed using input waveforms centered at different frequencies between 20-85 kHz. This choice was made in order to cover a frequency range that has the potential to excite separately one of the five modes with similar velocities on the excitability curves in Figure 3.5.

Table 3.2 Total variation of the phase velocity V_{ph} and cut-off frequency $F_{cut-off}$ for the excitations performed at position "A", "C" and "H".

Phase velocity (V_{ph}) ^a	Position A (%)	Position C (%)	Position H (%)
35 kHz	5.59	4.91	4.21
45 kHz	7.98	6.01	4.23
55 kHz	7.36	6.23	4.03
65 kHz	6.72	5.44	2.18
75 kHz	6.21	4.99	2.50
85 kHz	5.99	4.48	2.07
Cut-off frequency ($F_{cut-off}$) ^a	Position A (%)	Position C (%)	Position H (%)
First cut-off frequency (20 kHz)	17.37	16.31	16.31
Second cut-off frequency (40 kHz)	9.42	12.15	11.23
Third cut-off frequency (70 kHz)	5.45	6.99	5.38

^a The variations were calculated based on the difference computed between the "Healthy" and the "Osteoporotic" condition.

The sensitivity of phase velocity (V_{ph}) was strongly affected by the excitation position. The highest sensitivity was achieved at position "A", for all frequencies. On the other hand, the

cut-off frequency ($F_{cut-off}$) was only slightly affected by the position of excitation, showing similar sensitivities for all positions. However, the cut-off frequency was strongly affected by the frequency of excitation, showing a significantly higher sensitivity at the first cut-off frequency (20 kHz) as compared to the second (40 kHz) and third (70 kHz). Similarly, an increase in the sensitivity of the phase velocity (V_{ph}) was observed at lower frequencies, reaching a maximum variation at 45kHz, for all positions.

Figure 3.7 shows the power flow in the endosteal region (normalized to the total power flow) for modes $m=1$, $m=2$, $m=3$, $m=4$, and $m=5$, varying from 20 kHz to 100 kHz. The results show that mode $m=1$ has a higher power flow in the endosteal region as compared to the other modes, achieving approximately 23% of the total power in this region at 45 kHz. This explains the higher sensitivity obtained for the excitation performed at position "A", in which the mode $m=1$ excitability is 15 dB higher than the other modes (see Figure 3.5a)

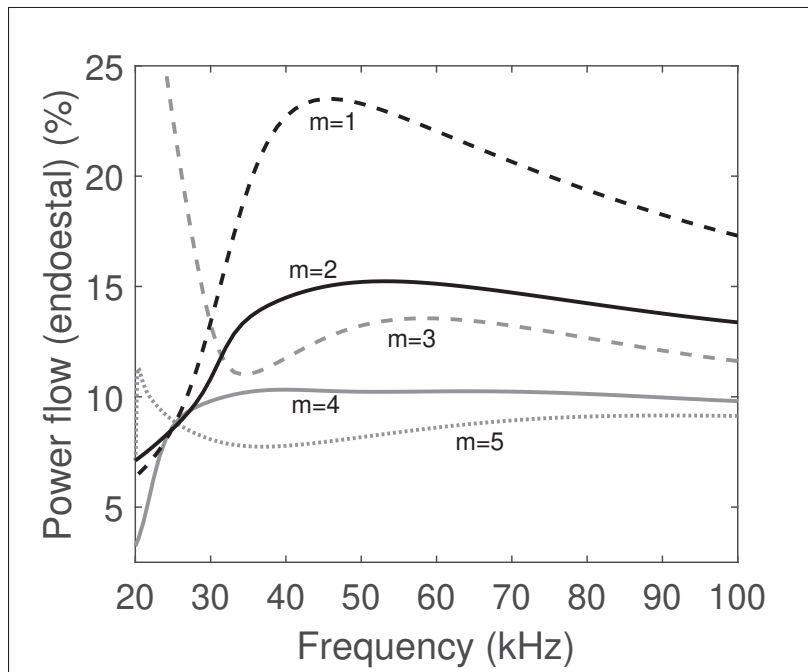


Figure 3.7 Power flow in the endosteal region normalized by the total power flow for modes $m=1$, $m=2$, $m=3$, $m=4$, and $m=5$ from 20 kHz to 100 kHz.

3.3.3 Effect of stiffness coefficients and density

Table 3.3 shows the percentage variation computed for the V_{ph} and $F_{cut-off}$ for each viscoelastic coefficient and density separately. The condition varied from "Healthy" to the "Osteoporotic". The excitation was performed at position "A" using central frequencies ranging between 20-85 kHz.

The sensitivity of V_{ph} showed a positive variation associated with coefficients C_{11} , C_{33} , C_{44} , C_{66} , while a negative variation was associated with the coefficient C_{13} and the density. Coefficient C_{44} showed the major contribution for most of the frequencies investigated (except at 35 kHz), accounting for approximately 50% of the variations in the degradation of all parameters taken together (identified as "Overall" in Table 3.3). The reduction in sensitivity observed at 35 kHz was found to be associated with the sharp decrease in the power flow of mode $m=1$ seen in Figure 3.7 at frequencies below 45kHz. In addition, it may be related to the reduction in excitability seen in mode $m=1$ at lower frequencies (see the excitability curves in Figure 3.5a), which may increase the interference from other modes, and consequently, reduce the sensitivity.

For the sensitivity of $F_{cut-off}$, a positive variation associated with the coefficient C_{66} was observed, accounting for almost 100% of the "Overall" variation. Such a dependence could be used to assess the status of coefficient C_{66} separately.

3.4 Conclusion

In this paper, the SAFE method was used to simulate the propagation of ultrasonic guided waves at low frequency (20-85 kHz) in a bone waveguide in the context of an axial transmission configuration. The SAFE method was shown to be an efficient tool for investigating the effect of intracortical properties on the propagation of ultrasonic guided waves since a number of configurations were simulated using reduced computing resources.

Table 3.3 Percentage variation computed for V_{ph} and $F_{cut-off}$ for each viscoelastic coefficient and density separately

Phase velocity (V_{ph}) variation (%) ^a	Position A						Overall
	C_{11}	C_{13}	C_{33}	C_{44}	C_{66}	Density	
35 kHz	0.32	-1.42	0.8	1.30	1.63	-0.79	5.59
45 kHz	0.37	-1.45	1.24	3.30	2.01	-0.611	7.98
55 kHz	0.31	-2.23	1.47	3.21	0.31	-0.72	7.36
65 kHz	0.36	-2.02	1.73	3.25	0.36	-0.62	6.72
75 kHz	0.16	-1.73	1.54	3.25	0.32	-0.71	6.21
85 kHz	0.08	-1.14	1.20	3.21	0.42	-0.67	5.99
Cut-off frequency ($F_{cut-off}$) variation (%) ^a							
First cut-off frequency (20 kHz)	0	0	0	0	22.06	-2.34	17.37
Second cut-off frequency (40 kHz)	0	0	0.90	0.90	9.42	-0.90	9.42
Third cut-off frequency (70 kHz)	0.94	0.52	0.41	0.94	3.98	-1.05	5.45

^a The variations were calculated based on the difference computed between the "Healthy" and the "Osteoporotic" condition.

Considering the actual bone geometry, sixteen ultrasonic guided wave modes were found in the 10-100 kHz frequency range (Figure 3.3b). However, only some of the modes have shown enough excitability and consequently clinical interest. In addition, the excitability and sensitivity of each mode were shown to vary according to the frequency and position of excitation on the bone surface. The phase velocity showed a maximum sensitivity at 45 kHz, which would appear to be associated with the peak of energy (power flow) concentrated in the endosteal region at this frequency. The cut-off frequency was only slightly affected by the position of excitation, but strongly by the frequency of excitation. A maximum sensitivity was achieved for the first cut-off frequency at approximately 20 kHz.

The sensitivity of phase velocity was associated with the variation in the physiopathological conditions of all the coefficients and density, but mainly with C_{44} . The sensitivity of the cut-off frequency for its part was mainly associated with variation in the physiopathological conditions of the stiffness coefficient C_{66} , allowing the axial shear modulus to be assessed separately.

Thus, by selecting an adequate frequency and position of excitation, low-frequency axial transmission was shown to be a promising method for assessing intracortical bone properties. The

features identified in this study could be used as metrics to compare the similarity between experimental and numerical data. A cost function based on these features could then be implemented into an inversion scheme to retrieve reliable bone properties from experimental data at low frequency. A parameterized bone-like geometry model, instead of a plate or cylinder, could potentially reduce the errors commonly encountered with in-vivo and ex-vivo experiments. For instance, the model could potentially compensate geometrical variations between different patients that are unrelated to the bone quality, such as the outer diameter and the external shape of the bone. The method could, therefore, be applied to identify small changes associated with early-stage osteoporosis or gradual evolution of the bone condition over time. For these extreme cases, since the sensitivity associated to slightly different degraded conditions was found to be modest, a good basis for comparison (e.g., a baseline method or a large reference database) would have to be implemented in order to guarantee the robustness of the method.

CHAPTER 4

EX-VIVO ASSESSMENT OF CORTICAL BONE PROPERTIES USING LOW-FREQUENCY ULTRASONIC GUIDED WAVES (<60 KHZ)

Daniel Pereira^{1 3}, Julio Fernandes^{2 3}, Pierre Belanger^{1 3}

¹ Department of Mechanical Engineering, École de technologie supérieure,
1100 Notre-Dame Street West, Montreal, Quebec, Canada H3C 1K3

² Department of Surgery, Université de Montréal, 2900 Boulevard Edouard-Montpetit,
Montreal, Quebec, H3T1J4 Canada

³ Centre de recherche l'Hôpital du Sacré-Coeur de Montréal, 5400 Boul Gouin O, Montreal,
Quebec, H4J1C5 Canada

Manuscript submitted to The Journal of the Acoustical Society of America in November 2018.

Abstract The early diagnosis of osteoporosis through bone quality assessment is a major public health challenge. Research in axial transmission using ultrasonic guided waves has shown the method to be sensitive to the geometrical and mechanical properties of the cortical layer in long bones. However, because of the asymmetric nature of cortical bone, the introduction of a more elaborate numerical model, as well as its inversion, continues to be challenging. The aim of this paper is, therefore, to implement a bone-like geometry using semi-analytical finite element (SAFE) modelling to perform the inverse characterization of *ex-vivo* radiuses at low frequencies (<60kHz). Five cadaveric radiuses were taken from donors aged between 53 and 88, and tested using a typical axial transmission configuration at the middle of the diaphysis. The dispersion curves of the propagating modes were measured experimentally, and then systematically compared to the solutions obtained with the SAFE method. For each sample, four parameters were estimated using an automated parameter identification procedure: (1) the bulk density; (2) the thickness; (3) the outer diameter, and (4) the shape factor. The results showed a good agreement between the predicted bulk density and the average voxel value calculated from computed x-ray tomography images. Furthermore, an excellent agreement was

observed between the geometrical parameters (thickness, outer diameter and shape factor) and the reference images.

Keywords: Low-frequency ultrasonic guided waves, Axial transmission, Cortical bone.

4.1 Introduction

Osteoporosis is associated with a reduction of bone mass and microarchitectural bone deterioration, leading to a reduction of bone quality (Papaioannou *et al.*, 2004; Strom *et al.*, 2011; Giangregorio *et al.*, 2006) and to an increase in the risk of fracture (Con, 1991). Dual-energy X-ray absorptiometry (DEXA) is currently the gold standard for diagnosing osteoporosis (Kanis, 1994). However, it suffers from several limitations (Haba *et al.*, 2016; Gluer, 2008). Quantitative ultrasound (QUS) was developed to assess bone quality using ultrasonic waves, and has the advantage of being non-radiative, non-invasive and relatively inexpensive (Gluer, 1997). It is therefore promising as a rapid screening method in clinical settings. The mechanical nature of ultrasonic waves allows the technique to be used to retrieve the biomechanical properties of bone tissues (Kaufman & Einhorn, 1993). QUS techniques can be used to go beyond simply estimating the bone mineral density currently obtained when using DEXA (Nicholson, 2008), and which is not sufficient to assess the risk of fracture (Sur, 2004).

QUS using axial transmission techniques has attracted significant interest, and has mostly been used to study the cortical bone. The resorption of the cortical bone results in a deterioration of material properties and in a reduction of the cortical bone thickness (Ritzel *et al.*, 1997). Thus, the stiffness, the density and the thickness are important properties when assessing cortical bone condition. Long bones, such as the radius or the tibia, constitute suitable waveguides for the propagation of ultrasonic guided waves, as has been shown in various studies (Haba *et al.*, 2016; Gluer, 2008, 1997). In this context, a multi-mode approach combining the measurement of more than one mode was shown to be capable of distinguishing between the contributions of mechanical and geometrical properties (Tatarinov *et al.*, 2005). For instance, low-frequency axial transmission (typically below 200 kHz) research has demonstrated that ultrasonic guided

waves are sensitive to changes in bone properties, such as the cortical thickness and the bone stiffness (Sarvazyan *et al.*, 2009; Kilappa *et al.*, 2011; Egorov *et al.*, 2014; Tran *et al.*, 2015). Operating at low frequencies offers the advantage of a lower attenuation, as well as a reduced number of propagating ultrasonic guided wave modes. The limited number of modes leads to a simplified interpretation of the signals. In addition, low-frequency ultrasonic guided wave modes tend to achieve greater penetration depths due to the longer wavelengths involved. Consequently, a low-frequency configuration has the potential to assess a much larger volume when compared to those with higher frequencies, e.g. 400-2000 kHz (Minonzio *et al.*, 2018; Bochud *et al.*, 2017). Furthermore, the sensitivity to variations in intracortical bone properties could be improved when using low-frequencies, which is of interest since early-stage osteoporosis is associated with resorption in the endosteal region (Ritzel *et al.*, 1997).

The ultrasonic assessment of mechanical and geometrical properties of cortical bone using ultrasonic guided waves commonly comes up against the challenge of solving multi-parametric inverse problems. Current multi-mode characterization methods rely on inversion schemes used to match experimental data with the modes simulated using simplified models, such as plates and cylinders (Minonzio *et al.*, 2015; Xu *et al.*, 2016; Kilappa *et al.*, 2015). Moilanen *et al.* (2007b) introduced an inversion scheme based on a free isotropic tube model for the *ex-vivo* estimation of the cortical thickness of the human radius. Similarly, Ta *et al.* (2009) used a bilayer isotropic tube model to estimate the thickness of bovine tibia specimens by manually matching the experimental velocities with the velocity of simulated modes. Recently, Foiret *et al.* (2014) implemented an inverse characterization routine to perform a pioneering estimation of both the thickness and the stiffness of *ex-vivo* cortical bone samples using a transversely isotropic free plate model. However, the proposed gradient-based optimization procedure required considerable prior knowledge to match the experimental data with the modelled ultrasonic guided wave modes. To overcome this issue, the same group later implemented a user-independent inversion scheme based on genetic algorithms to retrieve information from a multi-mode data set without any prior knowledge of the mode orders (Bochud *et al.*, 2016). More recently, they used a bilayer model to solve a similar inverse problem in order to evaluate

the impact of the complexity of the forward model on the accuracy of the inversion method (Bochud *et al.*, 2017). The results suggest that the sophisticated bilayer model is more precise in predicting experimental data when compared to a free plate model, but is very difficult to manage when solving the inverse problem. The reason for this was partially associated with the large number of modes generated by a bilayer model, which eventually would let almost any set of model parameters to fit the experimental data.

In this context, more comprehensive numerical approaches have increasingly been explored with the aim of improving the realism of cortical bone models and obtaining a better understanding of the ultrasonic guided wave phenomenon in cortical bone (Bossy *et al.*, 2004; Haiat *et al.*, 2011; Chen & Su, 2014; Moreau *et al.*, 2014). The semi-analytical finite-element (SAFE) method was already successfully implemented for modelling waveguides with arbitrary cross-sections (Thakare *et al.*, 2017; Nguyen *et al.*, 2017; Tran *et al.*, 2015; Pereira *et al.*, 2017). The capacity to model complex geometries is of particular interest at low frequencies, when the cross-sectional curvature of the cortical bone and its particular shape play an important role in modal excitability and on the propagation of the transmitted modes (Pereira *et al.*, 2017). Thus, introducing such a flexible model in an inversion scheme could potentially compensate for errors commonly encountered with *in-vivo* and *ex-vivo* measurements, as well as provide additional information associated with the cortical bone structure.

This paper aims to implement a parameterized bone-like model using the SAFE method to perform the inverse characterization of the cortical bone at low frequencies (<60kHz). Five *ex-vivo* radiuses were obtained from donors between the ages of 53 and 88 and tested using a typical axial transmission configuration in the middle 1/3 diaphysis. From the measured data, the dispersion curves of the propagating modes were computed using the two-dimensional spatio-temporal Fourier transform (2D-FFT), and then systematically compared to the simulated modes obtained with the SAFE method. For each acquisition, four parameters were estimated using an automated parameter identification routine: (1) bulk density; (2) thickness, (3) outer diameter, and (4) shape factor. The bulk density value is associated with a set of five effective transversally isotropic stiffness coefficients, which together constitute the material

properties of the volume of interest (VOI). The originality of the proposed inverse method lies in the consideration of the excitability curves to determine the most relevant modes when fitting the experimental data. Using the excitability greatly reduces the number of relevant modes, and therefore simplifies the mechanism of the inversion. The paper begins with a section on the materials and methods (Section 4.2), with details of the experimental measurements, the forward model and the procedure for the identification of the model parameters. This is then followed by a section presenting the results, which also includes the discussions (Section 4.3). Finally, conclusions are drawn (Section 4.4).

4.2 Material and Methods

4.2.1 Experimental measurements

4.2.1.1 Ex-vivo samples and reference values

The measurements were performed on five *ex-vivo* radius specimens supplied by the Université de Sherbrooke (Sherbrooke, Canada). The samples were taken from fresh cadavers aged from 53 to 88 years old (three males and two females). Consent from the donors to provide their tissues for investigation was provided in accordance with the Canadian code of ethics. The samples were kept frozen at -23°C until the measurements were performed. As a reference, measurements using computed x-ray tomography (CT) were performed in order to evaluate the robustness of the proposed inverse approach. The images were obtained with an isotropic voxel size of 0.19 mm in the cross-section (x and y in Figure 4.1) and 0.62 mm in the axial direction (z in Figure 4.2), using a CT scanner (GE-VCT-64, HSCM, Montreal, Canada).

For each specimen, the cross-sectional images were reconstructed at 120 sections in the middle 1/3 region. The region of interest (ROI - delimited by the white line in Figure 4.1) was defined for each cross-sectional image using a semi-automated threshold-based image processing algorithm. The average voxel value was then obtained for each cross-sectional image by averaging the gray level of all the pixels inside the ROI. For their part, the mean and standard

deviation values were determined by averaging the values obtained for all 120 cross-sectional images of the middle 1/3 region. Since the X-ray absorption coefficient depends mainly on the density, the mean value provides an estimation of the effective bulk density associated with the VOI while the standard deviation estimates the variation in the bulk density over the VOI. Similarly, the cortical thickness and outer diameter were computed by averaging the local thickness (th) obtained at 60 different angles θ over the ROI (Figure 4.1) using an edge detector image processing algorithm available in MATLAB 2017. The average cortical thickness was then obtained for each of the 120 cross-sectional images. The mean provides an estimation of the equivalent thickness associated with the VOI while the standard deviation estimates the cortical thickness variability observed over the VOI.

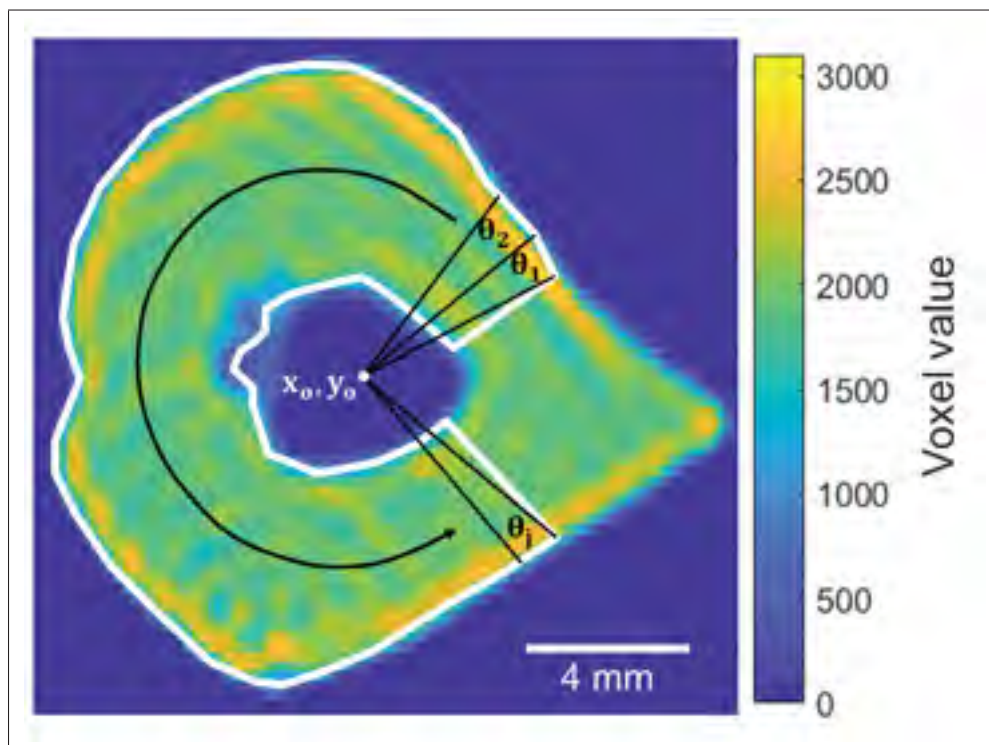


Figure 4.1 Computed tomography (CT) image taken at the middle 1/3 radius, with the white solid lines showing the ROI of the axial transmission measurements.

4.2.1.2 Axial transmission measurements

Acoustic excitation was performed using a piezoelectric probe (Olympus V318-SU-CF0.78IN-PTF) in contact with the upper part of the periosteal region next to the middle 1/3 region diaphysis, as shown in Figure 4.2. A 3-cycle Hann windowed toneburst centered at 40 kHz was used as the input waveform to perform the excitation. Three consecutive acquisitions over the middle 1/3 region were performed in the axial direction z at 38 positions equally spaced by 2 mm using a laser Doppler vibrometer (Polytec OFV-505). The probe and the sample were repositioned between each acquisition. A reflective tape coupled to the bone surface using ultrasonic gel was used to improve the signal-to-noise ratio (SNR) of the signal received by the laser Doppler vibrometer.

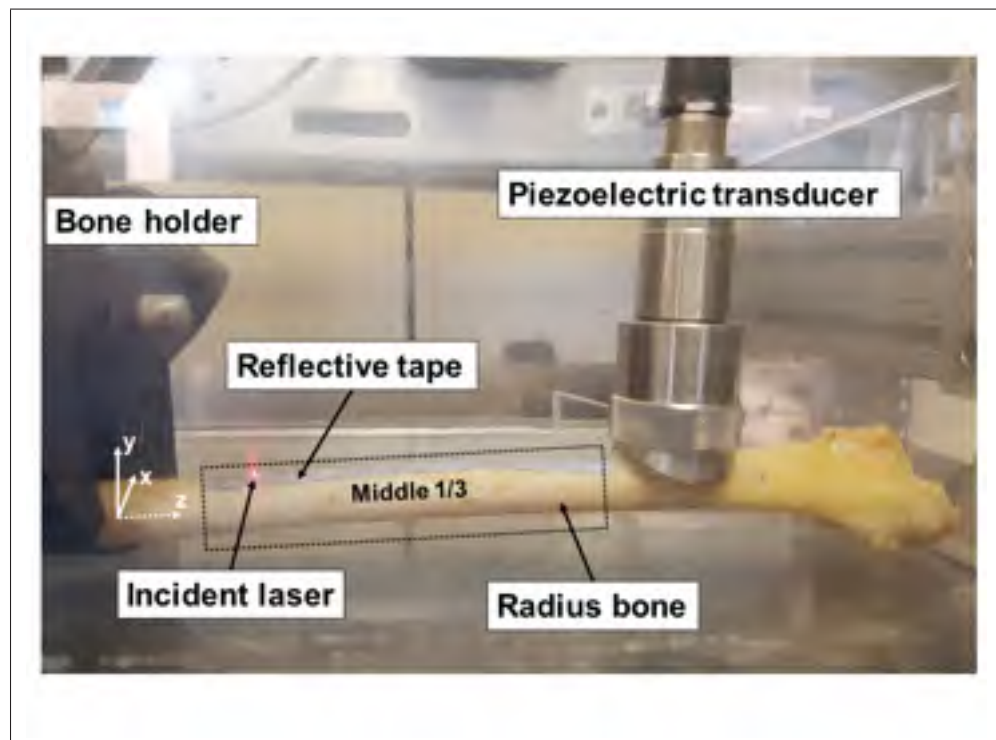


Figure 4.2 Axial transmission configuration used to perform the measurements on the radius specimens, with the black dashed lines showing the ROI.

The acquired time domain signals were processed using the 2D-FFT so as to calculate the intensities of the propagating modes in a frequency-wavenumber diagram (Alleyne & Cawley, 1990). Such frequency-wavenumber dispersion curves are extensively used in the literature in the context of cortical bone assessment (Lefebvre *et al.*, 2002; Moilanen *et al.*, 2006; Kiplappa *et al.*, 2011). More recently, the sparse singular value decomposition (S-SVD) method, combined with the fast Fourier transform (FFT), was established as an alternative for the high-resolution extraction of dispersion curves on cortical bone systems (Xu *et al.*, 2016). However, the S-SVD-based methods are known to increase the resolution by removing the singular vectors associated with the lowest singular values, which may lead to changes in the relative amplitude of the modes in the experimental dispersion curves. Since the proposed approach uses modal excitability to fit the experimental data with the simulated modes, the 2D-FFT appears to be more appropriate for preserving the relative amplitude between the propagating modes.

4.2.2 Forward model

In this study, a bone-like geometry was used as a forward model to match the experimental dispersion curves with the simulated ultrasonic guided wave modes generated by the SAFE model. The simulated solutions were obtained by solving the SAFE equations using the COMSOL Multiphysics 4.4 partial differential equation package. The following subsection (4.2.2.1) summarizes the background of the SAFE method, while a more detailed description of the SAFE procedure can be found in the literature (Predoi *et al.*, 2007; Fan *et al.*, 2008a). Subsection 4.2.2.2 then describes the bone-like model used as a forward model in this study.

4.2.2.1 Semi-analytical finite-element method

Essentially, the SAFE method assumes that ultrasonic guided waves propagate harmonically in the axial direction z with constant cross-section and material properties (Fan *et al.*, 2008a). Thus, the displacements field u_g can be described as:

$$u_g(x, y, z, t) = U_g(x, y) e^{-i(kz - \omega t)}, \quad i = \sqrt{-1} \quad (4.1)$$

where $g=1,2,3$ stands for the direction x , y and z , respectively. U_g is the displacement field in the cross-section plane (x, y) , k is the wavenumber, and ω is the angular frequency. Considering the mass density ρ and the viscoelastic coefficients C_{ghjl} , the differential equations of motion for an anisotropic material can be defined using the formalism for eigenvalue problems by:

$$C_{ghjl} \frac{\partial^2 U_j}{\partial x_h \partial x_l} + i(C_{g3jl} + C_{ghj3}) \frac{\partial(kU_j)}{\partial x_h} - kC_{g3j3}(kU_j) + \rho\omega^2 \delta_{gj} U_j = 0. \quad (4.2)$$

Equation 4.2 can be solved for a given frequency f , resulting in infinite instances of complex wavenumber k and their respective displacement fields $U_j(x, y)$, the so-called mode shapes.

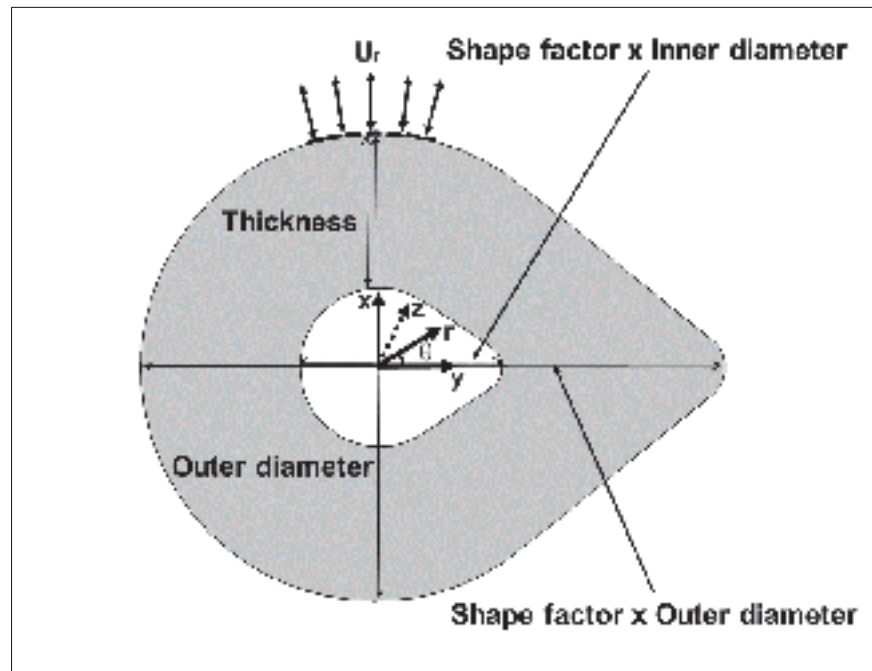


Figure 4.3 Forward model showing the bone-like geometry described in terms of thickness and outer diameter variables.

For a given frequency, the point excitability of the n^{th} mode E_n can be calculated based on its mode shape as (Wilcox *et al.*, 2005):

$$E_n = \frac{ik_n f}{8} \left(\frac{U_r^2}{P_z} \right) \quad (4.3)$$

where P_z is the total power flow in the z -direction associated with the mode shape, and U_r is the integral of the radial displacement over the region of excitation (see dashed line in Figure 4.3). Thus, modes having mode shape with large radial displacements in the excitation region tend to be highly excitable.

4.2.2.2 Bone-like model

The model geometry was defined based on the profile of the cortical bone in the middle 1/3 region of the human radius. Since the measurements were performed on dry specimens (without soft tissue), the soft tissue was not taken into account in this study. Furthermore, the bone marrow was not taken into account either in order to limit the complexity of the model and reduce the computational time. Therefore, a single cortical layer was modeled with a bone-like shape defined by three geometrical parameters: thickness (TH), outer diameter (OD) and shape factor (SF), as shown in Figure 4.3.

The waveguide was modelled as a homogeneous medium defined by a density (ρ) and five transversally isotropic stiffness coefficients ($C_{11}, C_{13}, C_{33}, C_{44}$ and C_{66}). The material properties were derived from an anisotropic homogenization theory recently introduced in the literature by Vu & Nguyen-Sy (2018). Figure 4.5 shows the effective coefficients as a function of the bulk density obtained using the aforementioned homogenization method. The bone-like geometry was then imported into the COMSOL Multiphysics environment. The mesh was built using triangular elements, with the size of the elements subjected to a constraint of at least 15 elements per wavelength, according to the frequency. Figure 4.4 shows a typical wavenumber-frequency representation of the simulated ultrasonic guided wave modes found between 5 and 60 kHz using the SAFE method. The color of each circle denotes the magni-

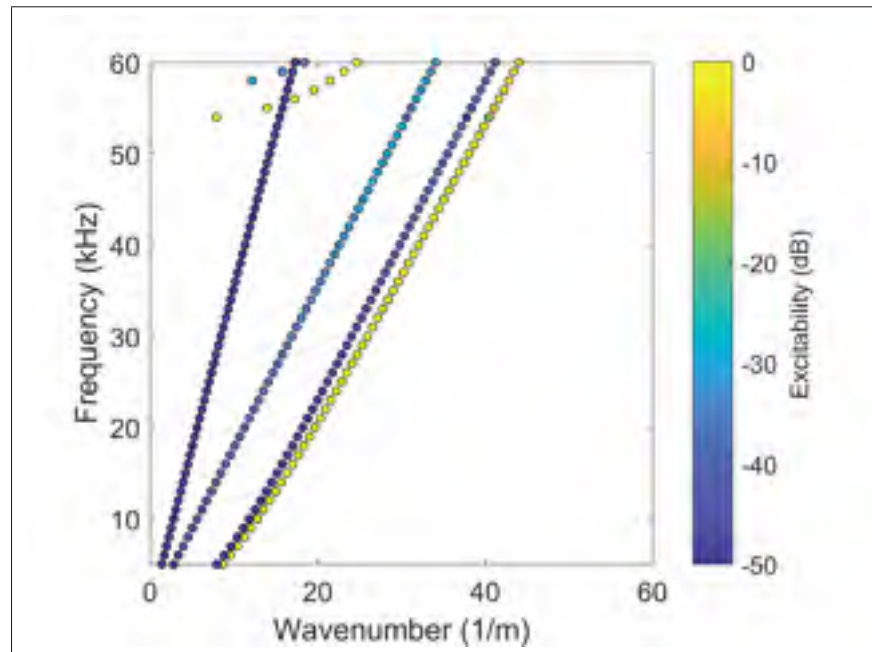


Figure 4.4 Typical wavenumber-frequency-excitability diagram computed by the forward model using the SAFE method. The color-map shows the excitability of each mode.

tude of the modal excitability (equation 4.3) associated with each wavenumber solution. Such a wavenumber-frequency-excitability representation was then systematically compared to the experimental dispersion curves in order to solve the inverse problem, as detailed in the next subsection.

4.2.3 Inversion problem

The inversion problem assumes that the properties of the cortical bone samples can be estimated by matching the experimental dispersion curves with simulated ultrasonic guided wave modes obtained from the parametrized bone-like model. Such a multi-parametric model-based approach requires the implementation of a cost function into an optimization procedure in order to find the optimal model parameters. The following two subsections (4.2.3.1 and 4.2.3.2) describe the cost function and the automatic parameter optimization routine employed in this study.

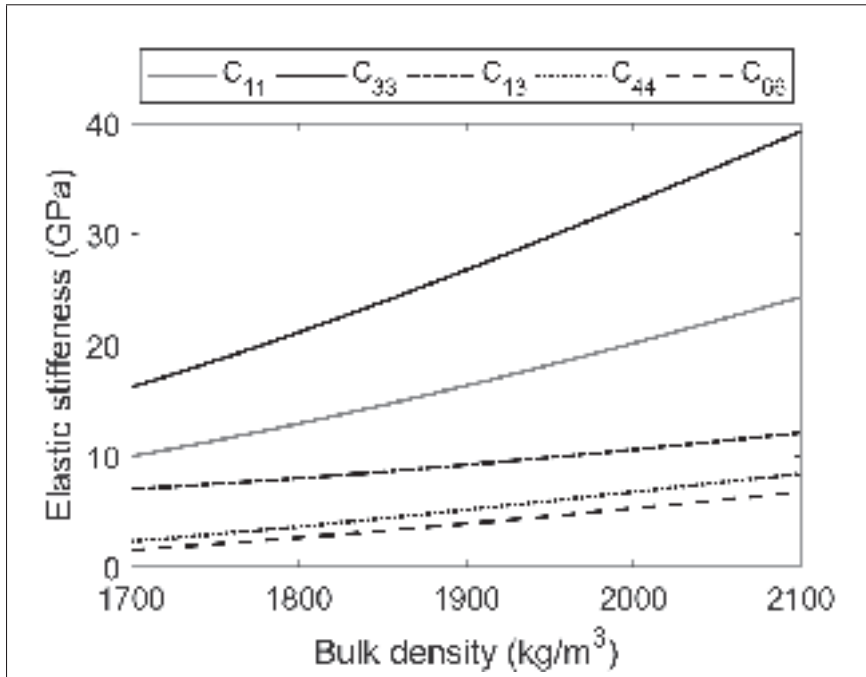


Figure 4.5 Effective transversally isotropic elastic properties of cortical bone varying with bulk density. The properties were obtained using an anisotropic homogenization theory introduced by Vu & Nguyen-Sy (2018).

4.2.3.1 Cost function

The cost function is typically the criterion used to fit the experimental data with a numerical solution, and it is a crucial element for solving the inversion problem. In the context of cortical bone assessment, it is far from trivial to establish a robust approach to evaluate the fit between the experimental and simulated dispersion curves (Minonzio *et al.*, 2018). However, both operating at low frequencies and using the modal excitability both reduce the number of ultrasonic guided wave modes of interest. A lower number of modes facilitates the fitting of the experimental dispersion curves to the simulated modes. As an example, Figure 4.6 (a) shows the dispersion curves measured experimentally on sample #1 between 5 and 60 kHz. The experimental amplitude (surface plot) can be interpreted as the excited modes that were propagating in the cortical bone waveguide during the experimental acquisition. Similarly, the circles de-

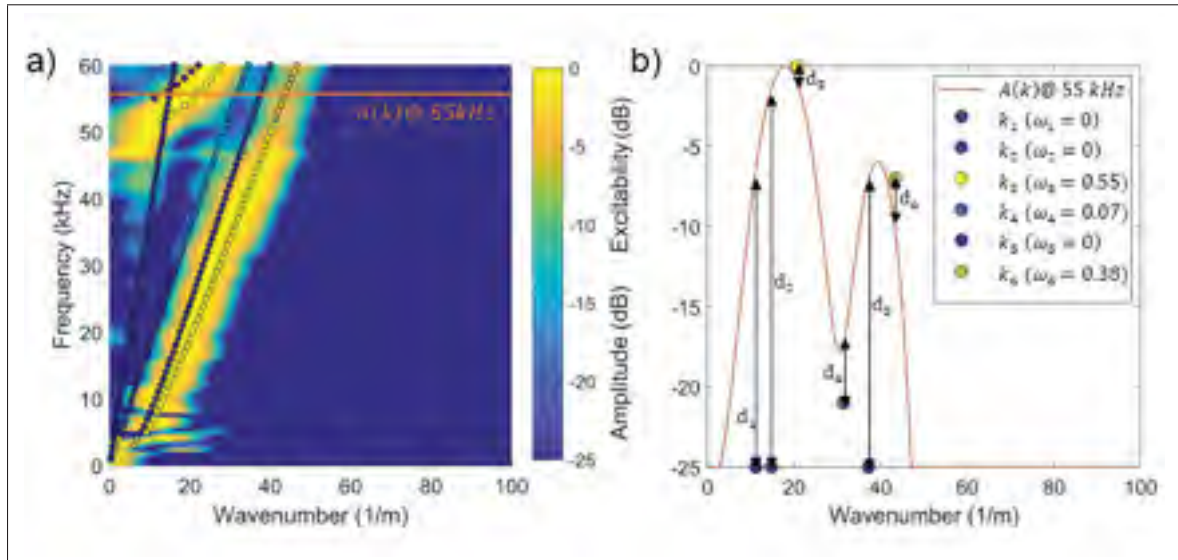


Figure 4.6 a) Typical solutions of the SAFE model (circles) overlaid onto experimental dispersion curves for frequencies between 5 and 60 kHz. The circles were filled with colors defined based on the modal excitability computed using equation (4.3); b) Amplitude extracted from experimental dispersion curves at 55 kHz along with simulated modes computed with the SAFE model and their respective excitabilities.

notes the wavenumber-frequency-excitability representation of the modes that were obtained using the SAFE model for a given set of model parameters. The challenge lies in defining a cost function that can be systematically used to quantify the fit between these two representations. In this study, the misfit of a given simulated mode was defined at each frequency by the distance between its modal excitability and the amplitude observed experimentally by:

$$d_n = E_n - A(k_n) \quad (4.4)$$

where E_n is the excitability of mode k_n and $A(k_n)$ is the amplitude observed experimentally at position k_n . For instance, Figure 4.6b shows the experimental amplitude and the modelled excitability at 55 kHz. The orange line shows the experimental amplitude varying as a function of the wavenumber, while the circles denotes the wavenumber-excitability representation for each of the six simulated modes obtained at 55 kHz. The respective distances between the modal excitability and the experimental amplitude (d_1, d_2, \dots, d_6) are shown in Figure 4.6b.

Furthermore, a weighting factor w_n associated with each mode was calculated by dividing the excitability E_n of each mode by the sum of the excitability of all the modes as:

$$w_n = \begin{cases} \frac{E_n}{\sum_{n=1}^N E_n}, & \text{if } E_n > L. \\ 0, & \text{otherwise.} \end{cases} \quad (4.5)$$

where N is the total number of modes and L is user-defined threshold. The weighting factor provides a means of accounting for the relevance of each mode when compared to all the possible modes. In other words, the modes with excitabilities lower than L are not taken into account in the cost function. For instance, by considering $L=-25\text{dB}$ in Figure 4.6b, the modes $n=3$, $n=4$ and $n=6$ have the weighting factors $w_3=0.55$, $w_4=0.07$ and $w_6=0.38$, respectively, while the modes $n=1$, $n=2$ and $n=5$ all have weighting factors equal to zero ($w_{1,2,5}=0$) because their excitabilities are lower than -25dB . The cost function J is defined by the sum over a range of frequencies of the square root of the sum of the square weighted distances as:

$$J = \sum_{f=f_s}^{f_e} \sqrt{\sum_{n=1}^N (d_n \cdot w_n)^2} \quad (4.6)$$

where f_s is the starting frequency and f_e is the ending frequency. Thus, the cost function takes into account only the most relevant modes, thereby reducing the possibility of confusion between solutions due to overfitting to the data. Furthermore, by evaluating the modes according to their excitability, this approach can be used to solve the inverse problem without any prior knowledge of the modes in the experimental dispersion curves.

4.2.3.2 Automatic parameter identification

The cost function was calculated for several different model solutions by sweeping the model parameters along a multi-dimensional grid in steps, according to the values in Table 4.1. The lowest value (global minimum) of the multi-dimensional grid was automatically identified for each of the three consecutive acquisitions on each sample. The respective mean and standard

deviations associated with the global minimums were then obtained and compared to the reference values obtained from the CT images. The density range was defined according to the physiological observations found in the literature (Vu & Nguyen-Sy, 2018), while the geometrical parameter ranges (thickness, outer diameter and shape factor) were defined in order to cover all the values observed in the CT images. The frequency bandwidth was defined to have enough mode features in the experimental dispersion curves while keeping the maximum frequency as low as possible. The grid steps were defined based on a trade-off between resolution and computation time. To resolve all the mode features, the frequency resolution was chosen to be sufficiently high, at 1 kHz steps.

Table 4.1 Bounds of the model parameters and their respective discretization used to perform the automatic parameter identification.

	Range	Step size
Bulk density (kg/m ³)	1720 - 2080	20
Thickness (mm)	1.5 - 4.0	0.1
Outer diameter (mm)	9.0 - 13.0	2.0
Shape factor	1.6 - 2.0	0.4
Frequency (kHz)	5 - 60	1

4.3 Results and Discussion

4.3.1 Dispersion curves fitting

Dispersion curves were measured for five *ex-vivo* specimens. Figure 4.7 shows the first acquisition of experimental data (surface plot), along with the simulated modes (circles) computed using the optimal model parameters. As shown, a remarkable agreement was found between the experimental data and the bone-like model. Most of the experimental data was matched by a combination of several high excitability mode segments (Excitability \geq -5dB). At least one cut-off frequency was identified in the dispersion curves and matched by a cut-off mode at different frequencies between 25 to 55 kHz, depending on each sample. For sample #5, however, no cut-off modes were observed. Furthermore, a considerable misfit between the

experimental amplitude and the simulated modes was found for frequencies between 20 and 50 kHz. This would appear to be related to the lower SNR observed for this specimen which is possibly associated with the high level of deterioration expected for the 88 year old female donor. Nonetheless, although the data are noisy and incomplete, the optimal bone-like model was able to match some of the features located at 10-20 kHz and 50-60 kHz.

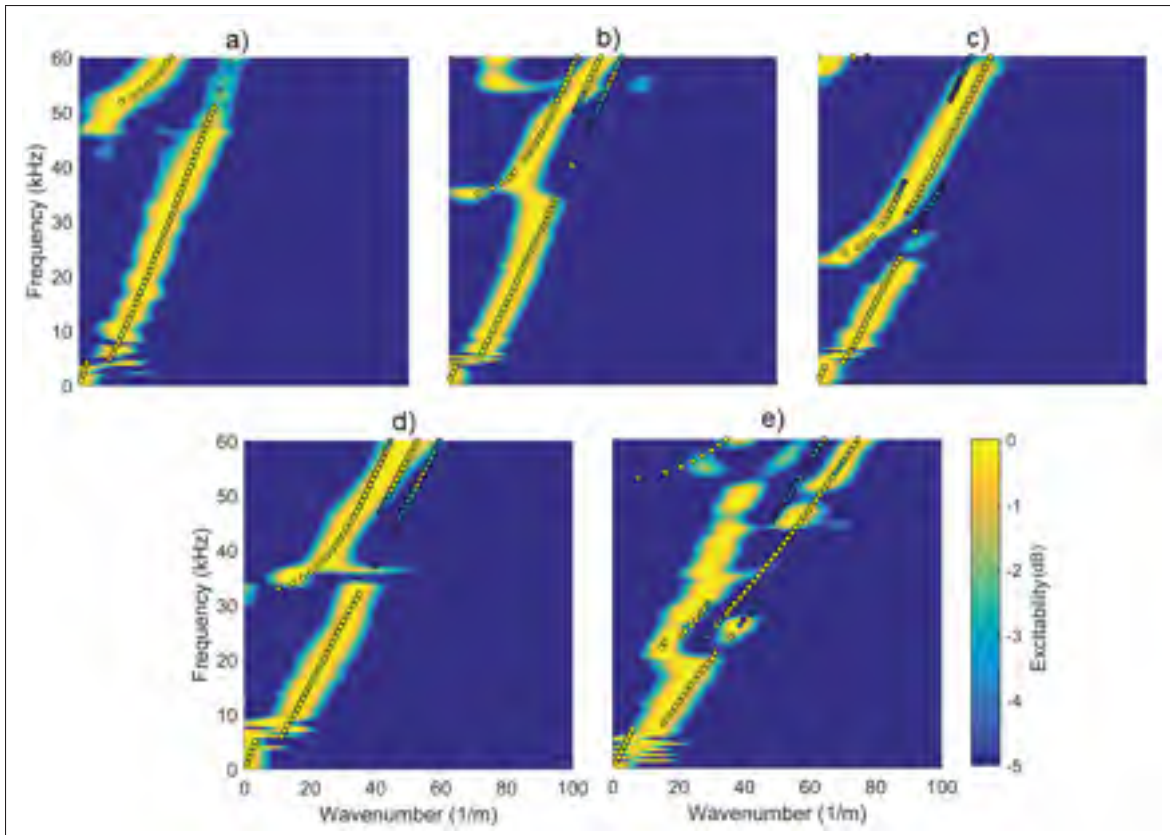


Figure 4.7 Optimal matching between the experimental dispersion curves and the simulated modes for: a) Sample # 1; b) Sample # 2; c) Sample # 3; d) Sample # 4, and e) Sample # 5.

Figure 4.8 shows a 2D representation of the normalized cost function values obtained (lower values mean better fit) when varying two model parameters (density and thickness). The remaining two parameters (outer diameter and shape factor) were set at the optimal values observed for the solution with the best fit out of all the evaluated models. For each sample, filled isolines were displayed using constant colors according to their current contour level in the

colormap. The colormap was set at values between 1 and 4, while the contour levels were separated from each other by an arbitrary value of 0.3. The contrast between the first and last contour levels can be interpreted as the susceptibility to ambiguities associated with each acquisition (higher contrast means less susceptibility to ambiguities). The dark blue area delimited by the first level (between 1 and 1.3) gives an idea of the resolution associated with the density and thickness, which can be interpreted as the ability of the inverse method to distinguish between two similar conditions involving these parameters. Finally, the red circles identify the precise location of the minimum values ($J=1$) associated with the first acquisition (filled circle) and second and third acquisitions (hollow circles). On each sample, one single and well defined dark blue region can be observed. The respective optimal density and thickness values associated to the global minimum ranged from 1820 to 1980 kg/m³ and from 1.3 to 4.4 mm. The contrast between the first and last contour levels and the sizes of the dark blue areas were found to be fairly similar for all the samples, except for sample # 5. As observed in Figure 4.8e, a much wider dark blue area in the density dimension was found on sample # 5. The same phenomenon was recently reported on a similar cost function evaluation by Mionzio *et al.* (2018) for strongly deteriorated bone samples. The authors associated the weak generation of guided modes with the disruption of the endosteal bone edge observed in aged donors. Therefore, it can be argued that a considerable part of the mode energy is expected to transfer across the endosteal edge to the bone marrow. Hence, this problem could potentially be addressed by adding the bone marrow inside the cortical bone model.

Furthermore, because of the very poor contrast between the first and last contour levels, the susceptibility to ambiguity was very evident for sample # 5. For instance, Figure 4.9 shows the normalized objective function grid for the second and third acquisitions performed on sample # 5. As observed, the presence of a second dark blue region was found on the third acquisition on sample # 5 (Figure 4.9b). Consequently, the optimal solution switched to the second local minimum region.

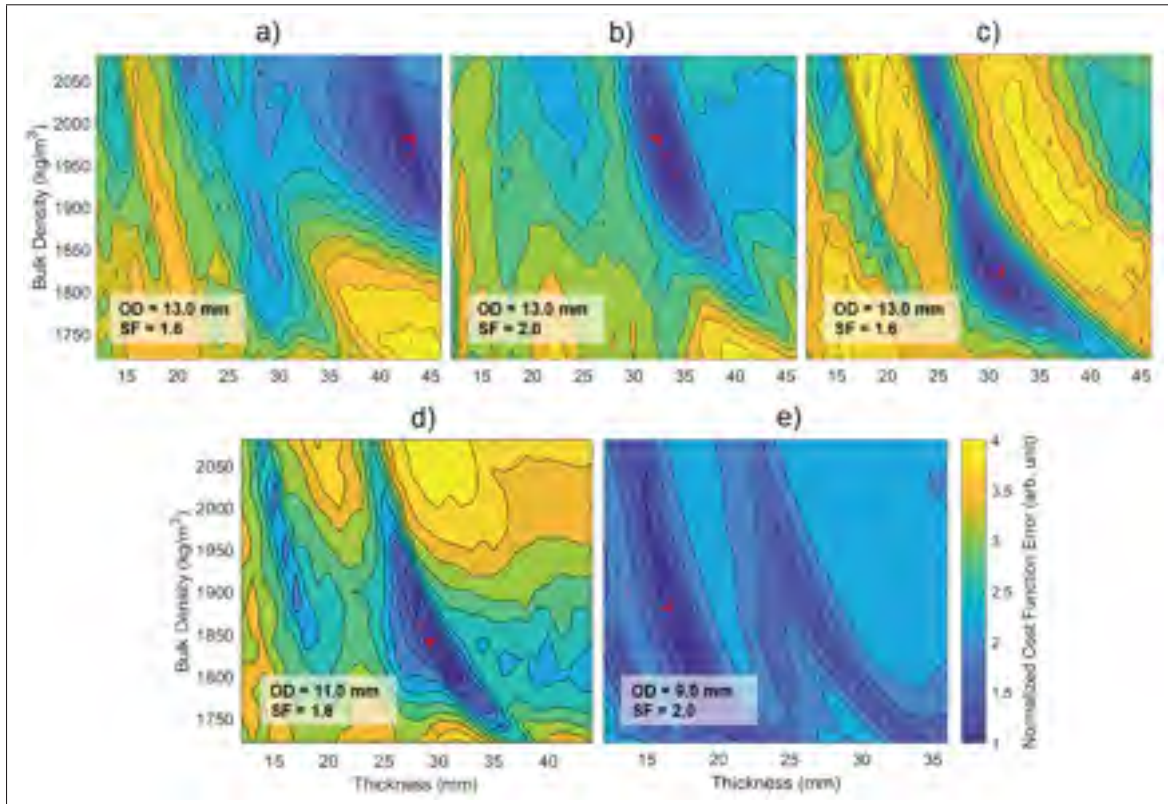


Figure 4.8 Normalized cost function obtained for the first acquisition by sweeping density and thickness while keeping outer diameter and shape factor with the optimal values on: a) Sample # 1; b) Sample # 2; c) Sample # 3; d) Sample # 4, and e) Sample # 5.

4.3.2 Estimated density

Figure 4.10 shows the mean and standard deviation obtained for the density (red circles) varying from samples # 1 to # 5, along with the reference average voxel values measured from the CT images (black solid lines). It is worth remembering that the ultrasonic measurements were performed over the whole middle diaphysis (76 mm of acquisition length) and at very low-frequency (high penetration). Therefore, the predicted density values (and their respective stiffness coefficients) can be interpreted as the effective material status associated with the whole middle diaphysis volume. Similarly, the average voxel values were calculated from the average of 120 sections over the middle diaphysis and, therefore, allow a plausible comparison with the equivalent density. Hence, the results suggest that the material condition on samples

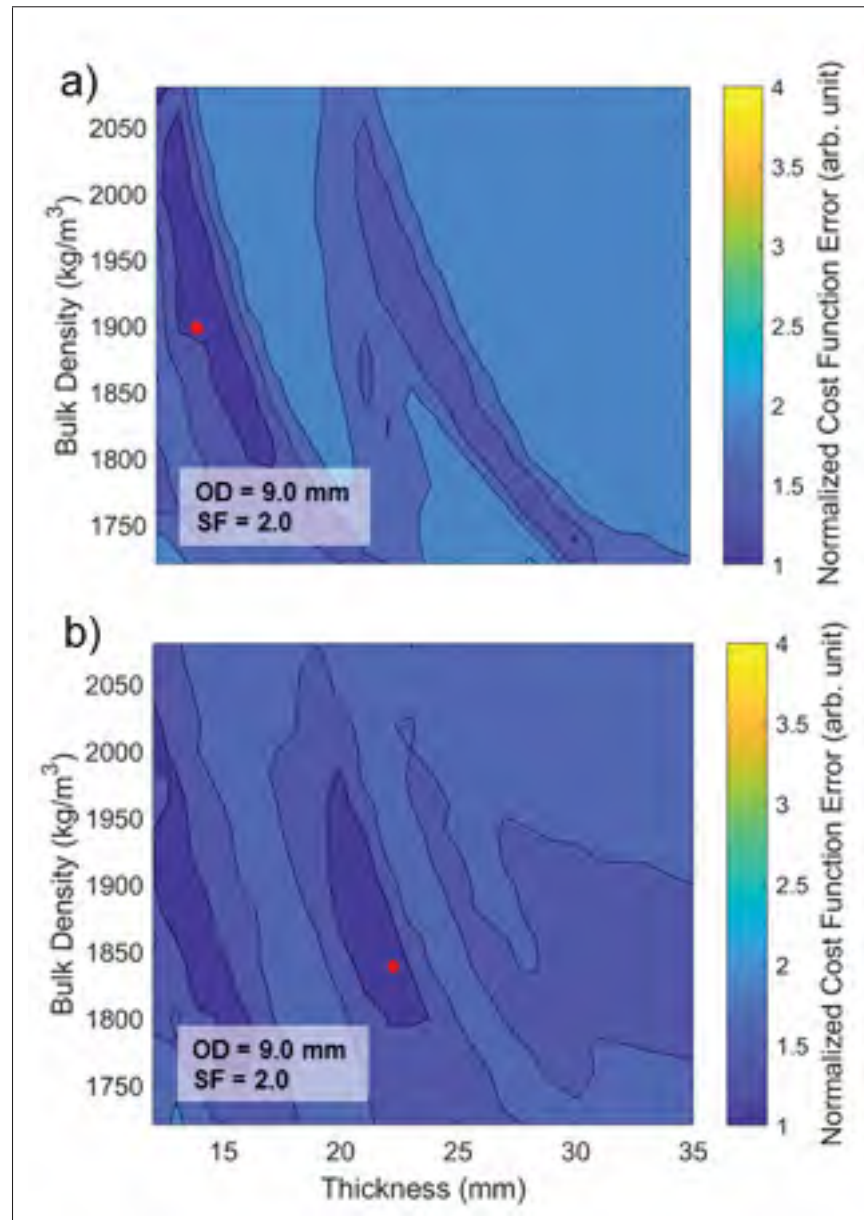


Figure 4.9 Normalized cost function grid obtained on: a) Sample # 5, second acquisition and b) Sample # 5, third acquisition.

1 and # 2 are slightly less degraded when compared to samples # 3, # 4 and # 5. Despite the lack of a parameter for performing a direct comparison against the predicted density, the evolution of the predicted values over the samples was found to be in agreement with the evolution of the average voxel values and the respective ages of the donors (see Figure 4.10). The estimated resolution associated with the density measurements was around $\pm 30 \text{ kg/m}^3$.

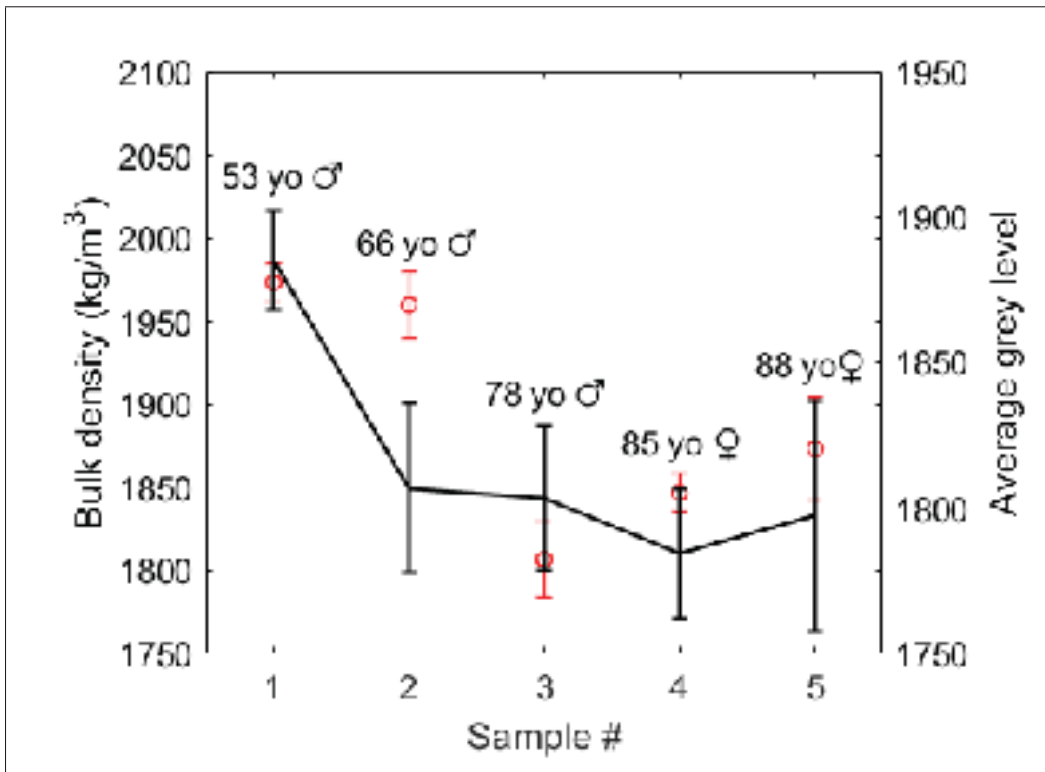


Figure 4.10 Mean and standard deviation obtained for density (red circles), varying from samples # 1 to # 5, along with the reference average voxel values measured from the CT images (black solid lines).

4.3.3 Estimated thickness

Figure 4.11 shows the comparison between the estimated thickness (red circles) and the reference values (black solid lines). Similarly to the density, the predicted and reference thicknesses can be interpreted as an equivalent thicknesses of the cortical layer associated with the whole middle diaphysis volume. As observed, an excellent agreement was observed between the predicted and reference thickness. The relative difference between the predicted and reference values varied between 4.2% and 9.8%, remaining around the order of magnitude of the reference standard deviations for all the samples, except for # 5. The estimated resolution accounted for the thickness measurements on sample # 1 to # 4 was around ± 0.15 mm. The higher standard deviation obtained for sample # 5 was associated with the presence of a second

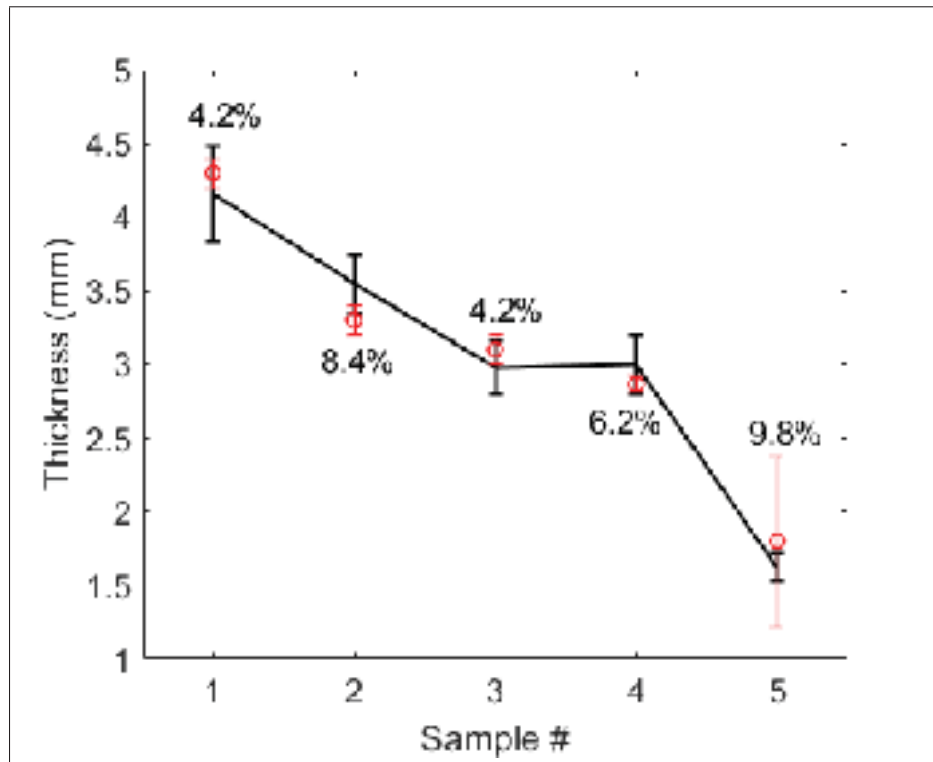


Figure 4.11 Mean and standard deviation obtained for thickness (red circles) varying from sample # 1 to # 5 along with the reference values measured from the CT images (black solid lines).

minimum region in the cost function grid (Figure 4.9b), which caused the optimal solutions to alternate between the two local minimum regions.

4.3.4 Estimated bone-like shape

Figure 4.12 shows the estimated bone-like shape (white dotted lines) overlaid onto a cross-sectional CT slice taken from the middle of the VOI. For each sample, the estimated bone-like shape was drawn using the mean values obtained for the three geometrical parameters (thickness, outer diameter and shape factor). A remarkable agreement was found between the predicated bone-like geometry and the cross-sectional images. Instead of a simple thickness estimation (seen in Figure 4.11), the bone-like model was able to predict other geometrical features related to the bone shape that were clearly different among the samples. For instance,

the external diameter observed for the male samples (# 1, # 2 and # 3) was higher than those for female samples (# 4 and # 5): the bone-like model predicted an outer diameter of 13 mm for the male samples (# 1, # 2 and # 3), while for the females samples (# 4 and # 5, respectively), it was 11 mm and 9 mm. Furthermore, the external shape of the bone observed in the cross-sectional images was found to be slightly different from sample to sample. The model predicted a shape factor of 2.0 for samples # 2 and # 5 and of 1.6 for the other samples, which appears to be in agreement with the CT images. The estimated bone-like geometry can be seen as an equivalent cross-sectional geometry associated with the whole middle diaphysis. Such an estimation goes beyond a simple localized thickness measurement and has the potential to provide additional information regarding the risk of fracture.

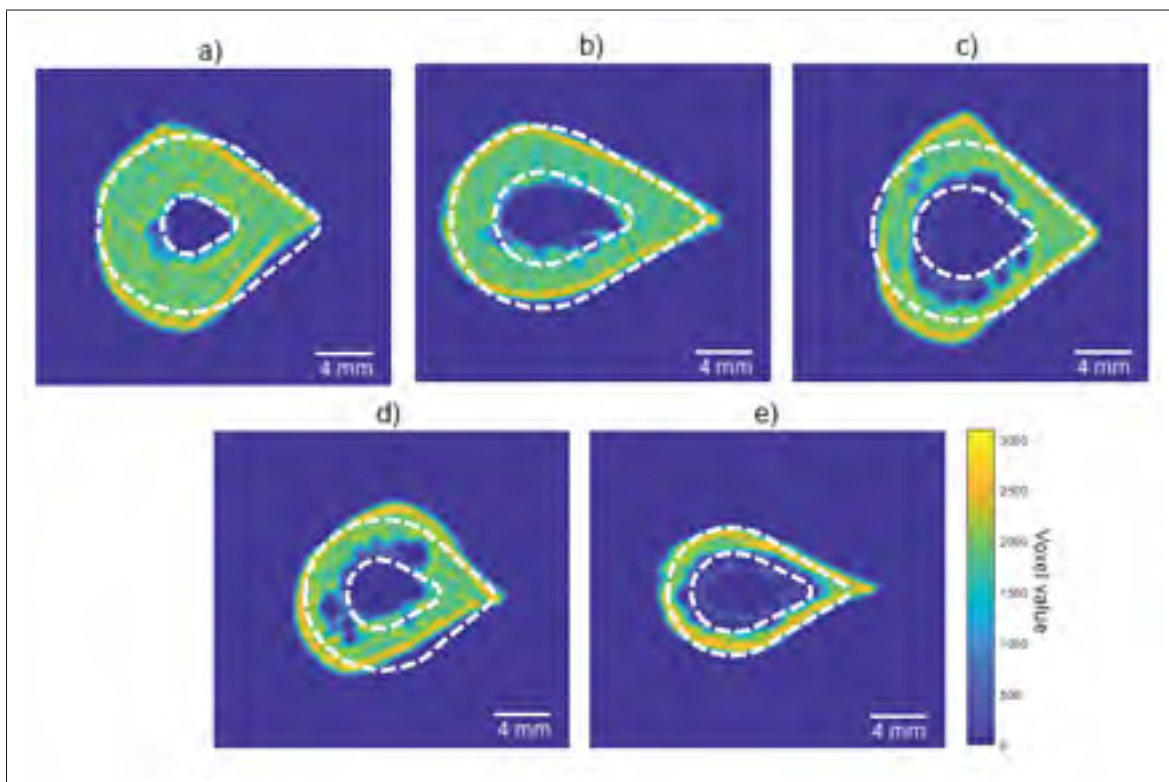


Figure 4.12 Estimated bone-like shape (white dotted lines), along with cross-sectional CT slice taken from the middle of the VOI for: a) Sample # 1; b) Sample # 2; c) Sample # 3; d) Sample # 4, and e) Sample # 5.

4.4 Conclusions

In this study, the inverse characterization of five radius samples was performed at low frequencies ($<60\text{kHz}$). Four parameters (bulk density, thickness, outer diameter and shape factor) were estimated by systematically fitting the experimental data with simulated modes. In general, the proposed bone-like model was able to match most of the amplitude in the experimental dispersion curves through a combination of several high excitability mode segments.

Strong agreements were observed between the estimated density and thickness and their respective reference values obtained from CT images. However, because of a lack of a direct comparison parameter, only the thickness was directly validated against reference values, and the error was always under 10%.

For sample # 5, a considerable misfit between the experimental amplitude and the simulated modes was found, which drastically increased the uncertainty associated with the thickness assessment. This would appear to be related to the highly aged condition associated with sample # 5 (88 year old female), which weakens the reverberation from the endosteal edge and subsequently limits the generation of the ultrasonic guided wave modes. This problem could potentially be addressed by adding the bone-marrow inside the cortical bone model.

Besides the thickness and density, the bone-like model introduced in this study was able to retrieve additional geometrical information associated with the cortical bone shape. Furthermore, the proposed low-frequency axial transmission configuration was able to infer equivalent bone properties associated with a much larger cortical volume when compared to the conventional inversion techniques using higher frequencies.

Finally, the proposed inverse method has the potential to improve the assessment of the risk of fracture. However, the actual clinical relevance of assessing larger cortical volume and extra geometrical parameters is outside the scope of the present paper, and needs to be further investigated.

4.5 Originality of the proposed work

The novelty of this study lies in the implementation of a more comprehensive cortical bone waveguide model than the typically plate and cylinder models reported in the literature. The model was used to study the propagation of ultrasonic guided waves in a waveguide with an irregular, heterogeneous, multi-layered cross-section and transversally isotropic viscoelastic material properties. Such a combination of cortical bone features has never been reported in the literature when modeling cortical bone as a waveguide. Furthermore, notwithstanding the remarkable progress achieved over the past few years on the understanding of ultrasonic guided wave phenomena in cortical bone, the physical interaction between low frequencies ultrasonic guided waves and the cortical bone structure remains unexplored. Hence, the proposed SAFE model was used to investigate, for the first time, the potential of ultrasonic guided waves in assessing small variations in the intracortical bone properties at very low frequencies (<85 kHz). The proposed low frequencies configuration has the potential to assess a much larger cortical volume when compared to higher frequencies typically reported in the literature, e.g. 400-2000 kHz. Finally, a parameterized bone-like model was used to perform the inverse characterization of the cortical bone properties in the middle 1/3 diaphysis. The originality of the proposed inverse method lies in its comprehensibility when simulating the cortical shape as well as on the consideration of the excitability curves to determine the most relevant modes when fitting the experimental data. The results from this thesis will be potentially used to define the parameters and instrumentation of a pilot clinical study on the detection of osteoporosis.

CONCLUSION AND RECOMMENDATIONS

In this study, a comprehensive and computationally efficient cortical bone model was implemented using the SAFE method. The model combined different cortical bone features such as an irregular, heterogeneous and multi-layered cross-section and transversally isotropic viscoelastic material properties. The method was successfully applied in the context of axial transmission in bone to investigate the feasibility of FAS to monitor degradation of intracortical properties at low-frequency. A first journal paper (Chapter 2) was published on this topic in April 2017 in the Journal of Acoustical Society of America (JASA); a high impact factor journal in the field of acoustic. The calculated FAS velocity was shown to be associated with the velocity of the mode with the highest amplitude contribution. However, due to the change between the modes with the greatest contribution, the FAS velocity was shown to be a poor discriminator of intracortical bone properties.

To address this limitation, a time-spatial frequency analysis technique instead of the FAS velocity was investigated using an array of receivers. The effect of intracortical bone properties on the phase velocity and cut-off frequency of low-frequency ultrasonic guided wave modes was then determined for different excitation positions on the bone surface. Furthermore, the individual contribution of each viscoelastic coefficients and of the density were evaluated separately. The excitability and sensitivity of the excited modes were shown to vary according to the frequency and the position of excitation on the bone surface. A second journal paper (Chapter 3) was submitted on this topic in July 2018 to JASA and is currently under final revisions. The phase velocity showed maximum sensitivity at 45 kHz, which would appear to be associated with the peak of energy (power flow) concentrated in the endosteal region at this frequency. The cut-off frequency was only slightly affected by the position of excitation, but strongly by the frequency of excitation. A maximum sensitivity was achieved for the first cut-off frequency at approximately 20 kHz. Thus, by selecting an adequate frequency and position

of excitation, the low-frequency axial transmission was shown to be a promising method for assessing intracortical bone properties.

In order to validate that, an autonomous model-based optimization routine to perform the inverse characterization of the cortical bone properties was successfully implemented. A parameterized bone-like model was used to perform the inverse characterization of five radius samples at low frequency (<60 kHz). A third journal paper (Chapter 4) was recently submitted to IEEE Transactions on Ultrasonics, Ferroelectrics and Frequency Control; the journal has a high impact factor and it is a reference regarding new and improved clinical ultrasound techniques in medicine. The proposed bone-like model was able to match most of the amplitude in the experimental dispersion curves by a combination of several high excitability mode segments. A good to excellent agreement was found between the estimated density and thickness and their respective reference values obtained from CT images. Furthermore, the bone-like model was able to retrieve additional geometrical information associated to cortical shape. The proposed low-frequency axial transmission configuration was able to interrogate equivalent bone properties associated to a much larger cortical volume when compared to the conventional inversion techniques using higher frequency.

As a global conclusion, the proposed axial transmission configuration combined with a novel inversion procedure has the potential to increase the detectability of early stages of osteoporosis as well as improve the assessment of the risk of fracture. However, the actual clinical relevance of assessing larger cortical volume and extra geometrical parameters was outside the scope of this work and should to be further investigated. The results available could be used to define the parameters and instrumentation of a pilot clinical study on the detection of osteoporosis. Furthermore, the methodology implemented in this project was successfully extended to other applications. The methodology was adapted to perform the inverse characterization of a stiffener bonded line using an appropriated SAFE geometry and model parameters. This study was

presented at the 45th Annual Review of Progress in Quantitative Nondestructive Evaluation (Burlington, Vermont, US) in July 2018 and reported as conference paper (Appendix II).

Finally, as a recommendation, the development of a customized SAFE solver code using parallel graphics processing unit (GPU) computation to reduce the computational time to solve the inverse problem would be very useful. In summary, this would allow increasing the complexity of SAFE model and/or adding more model parameters in the analysis. In this context, it is strongly recommended the implementation of bone marrow on the inversion model and also the soft-tissue when dealing with in-vivo measurements.

Furthermore, the fabrication of a linear probe array that reproduces the axial transmission configuration applied in the experiments on third manuscript (chapter 2) is recommended.

Finally, an in-vivo study involving a large number of samples combined with reliable reference technique (e.g. HR-pQCT) is also recommended. This would provide a statistical support for the findings raised in this thesis, specifically in the third manuscript (chapter 2).

APPENDIX I

AXIAL TRANSMISSION ASSESSMENT OF TRABECULAR BONE AT DISTAL RADIUS USING GUIDED WAVES

Daniel Pereira¹, Axelander Abid¹, Lucien Diotalevi¹, Julio Fernandes², Pierre Belanger¹

¹ Département de Génie Mécanique, École de Technologie Supérieure,
1100 Notre-Dame Ouest, Montréal, Québec, Canada H3C 1K3

² Centre de recherche l'Hôpital du Sacré-Coeur de Montréal, 5400 Boul Gouin O, Montreal,
Quebec, H4J1C5 Canada

Manuscript published in the Proceeding of the 170th Meeting of the Acoustical Society of America, Jacksonville, Florida, US, November 2016.
[<https://doi.org/10.1121/2.0000282>]

Abstract The diagnosis of osteoporosis at skeletal sites composed mainly of trabecular bone, such as the distal radius, can be considered clinically more relevant than cortical bone regions. Thus, the possibility to merge the potential of guided waves method to the clinical relevance of trabecular bone assessment is extremely motivating and has not yet been explored in details. Therefore, the objective of this paper is to investigate the feasibility of using ultrasonic guided waves to detect variation in the mechanical properties of trabecular bone at the distal radius using axial transmission. Finite elements simulations were performed using a three-dimensional (3D) model of a human radius. The simulated excitation was applied at the extremity of the bone, while the acquisition of the responses was performed by an array of receivers along the bone surface. The responses were compared to the numerical dispersion curves obtained using semi-analytical finite element method (SAFE). Finally, different trabecular bone properties were simulated in order to evaluate the effect on the propagation of the guided waves. The results showed that ultrasonic guided waves excited at the extremity and detected on the bone surface are feasible to detect changes in the properties of the trabecular bone.

Keywords: Ultrasonic guided waves, Intracortical, Low-frequency.

1. Introduction

Ultrasonic guided waves methods have been successfully applied in non-destructive testing (NDT) to characterize different classes of materials, including composite plates and complex structures Agostini *et al.* (2003); Chimenti (1997); Vallet *et al.* (2014). In the last decade, the methods have been extensively studied and adapted to cortical bone quality assessment (Talmant, 2011; Nicholson *et al.*, 2002). Similarly to pipes in the NDT field, long cortical bones such as the radius or tibia are suitable waveguides for the propagation of ultrasonic guided waves (Minonzio *et al.*, 2013). Each propagating mode interacts differently with the mechanical and geometrical aspects of the waveguide, and these multi-modal characteristics can be considered the main advantage of the method, once the sensitivity of the analysis can be improved through the selection of a desired group of modes in order to interrogate a specific region/parameter of the bone structure. Recent studies based on ultrasonic guided waves already showed considerable evidences that the multi-modal approach is more comprehensive and sensitive when compared to single velocity analysis (Ta *et al.*, 2006).

Most axial transmission devices are developed focusing on the assessment of the cortical region of the middle 1/3 of the radius, since cortical bone properties are affected by age-related bone reabsorption and osteoporosis (Rico, 1997). Furthermore, cortical bone accounts for the main portion of the skeleton, and it supports most of the load of the body (Laugier & Haiat, 2011). The cortical bone is a much more convenient waveguide, since it is essentially composed of a cortical shell filled with a bone marrow in a virtually constant cylinder-like geometry. For that reason, cylinder and plate models have been successfully used as a theoretical reference for inverse estimation of elastic and geometrical properties of the cortical bone (Ta *et al.*, 2009; Kang Il Lee, 2015). On the other hand, the diagnosis of osteoporosis at skeletal sites composed mainly of trabecular bone, such as the distal radius, is more clinically relevant (Muller *et al.*, 2008). Most of the distal radius fracture occurs about 3 cm from the end of the bone, in a region composed mainly of trabecular bone, where the osteoporotic changes are considered to occur first due to the higher surface to volume ratio (Langton & Njeh, 2008). Thus, the possibility to merge the potential of ultrasonic guided waves method to the clinical relevance of trabecular bone assessment is extremely motivating and has not yet been explored in detail.

In this paper, the feasibility of propagation of ultrasonic guided waves to assess the mechanical properties of trabecular bone at the distal radius was investigated in an axial transmission configuration. Due to the complexity of the distal region, finite elements (FE) simulations were performed using a 3D model built from a computed tomography of a human radius. The simulated excitation was transmitted to the radius using a longitudinal load applied to a small circular region at the extremity of the bone using an 8-cycle Hann windowed toneburst centered at 80 kHz. The acquisition of the responses was simulated using an array of 32 receivers positioned on the surface of the bone using two-dimensional fast Fourier transform (2D-FFT). The intensities of the 2D-FFT map were compared to the numerical dispersion curves obtained using the semi-analytical finite element (SAFE) method. Finally, 2D-FFTs maps were simulated for different trabecular bone properties in order to evaluate the sensitivity of the guided waves to the properties of trabecular bone. The results have shown that the excitation imposed at the extremity generates ultrasonic guided waves that can be identified by an array of receivers along the long bone. Furthermore, the propagating modes were sensitive to changes in the trabecular bone properties.

2. Methods

2.1 Finite-element method

Time domain FE simulations were performed in ABAQUS software using explicit analysis. The model was built using a 3D computed tomography of a human radius composed of two different parts: distal 1/3 of the radius, located at the end of the bone and composed of cortical and trabecular bone; and the middle 1/3 radius, located in the long bone and composed of cortical bone and bone marrow. The cortical and trabecular bone were modeled as viscoelastic isotropic material, while the bone marrow was modeled as a viscous fluid using the values shown in the Table I-1. To avoid reflections from the extremity, absorbing boundaries were added on the end of the model Drozd *et al.* (2007). The model was built using 2 mm tetragonal elements, respecting at least 7 elements per the smallest wavelength. The simulation was performed using time-step of 1e-8 seconds and total time of 0.001 seconds. A longitudinal

load was applied to a small circular region at the extremity of the bone using an 8-cycle Hann windowed toneburst centered at 80 kHz. The out-of-plane displacement was recorded by an array of 32 receivers equally displaced by 2 mm placed along the the bone in the axial direction and processed using 2D-FFT. Figure I-1a shows the excitation and acquisition setup applied in the FE simulations.

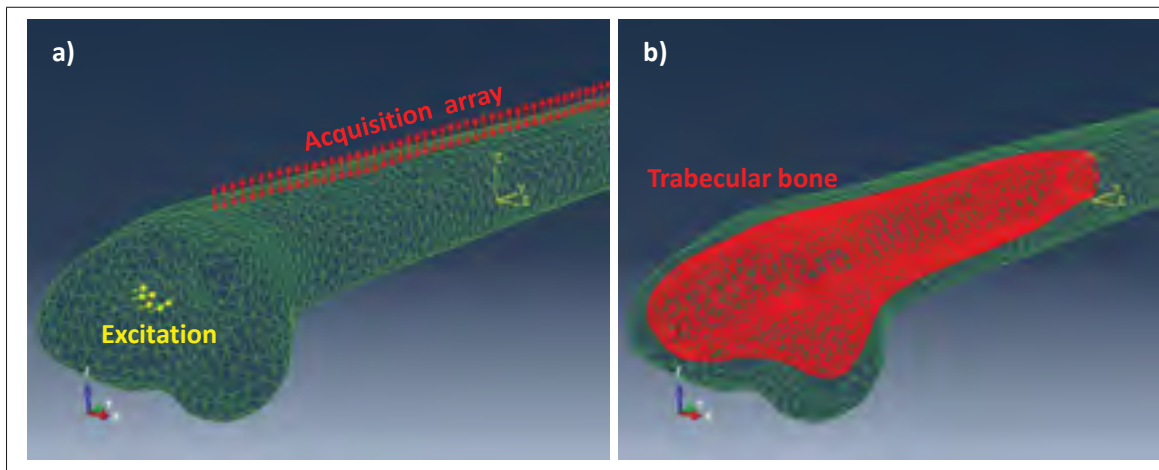


Figure-A I-1 FE model used in the simulations showing: a) the excitation and acquisition setup applied in the simulations and b) the trabecular bone located on the internal part of the distal 1/3 region.

Table-A I-1 Properties of the radius bone model used to perform the FE simulations.

Bone component	Density (kg/m ³)	E ^a (GPa)	K ^a (GPa)	Poisson ratio	Damping (s ⁻¹)
Cortical bone	1850	10	-	0.3	2e-7
Trabecular bone	1220	2	-	0.2	5e-7
Bone marrow	1000	-	2.2	-	0.5e-7

^a E and K are the Young's and Bulk modulus, respectively.

2.1.1 Sensitivity study

In order to evaluate the sensitivity of ultrasonic guided waves to the properties of trabecular bone, the FE simulations were performed using different values for density and Young's modulus while the other properties were kept constant as shown in Table I-2. Such an approach

constitutes a simple way of modeling early changes in trabecular bone due to osteoporosis. The 2D-FFT maps obtained for each simulations were compared qualitatively.

Table-A I-2 Properties of the trabecular bone used in the sensitivity study.

Bone component	Density (kg/m ³)	E (GPa)	Poisson's ratio	Damping (s ⁻¹)
Trabecular bone 1	1470	3.87	0.2	5e-7
Trabecular bone 2	1420	3.25	0.2	5e-7
Trabecular bone 3	1370	2.63	0.2	5e-7
Trabecular bone 4	1320	2.00	0.2	5e-7
Trabecular bone 5	1270	1.37	0.2	5e-7
Trabecular bone 6	1220	0.75	0.2	5e-7

2.2 Semi-analytical finite-element method

The SAFE stimulations were performed using COMSOL Multiphysics software. A brief overview related to the theoretical background of the semi-analytical finite-element method will be provided here. A more comprehensive background can be found in standard textbooks (Mazzotti *et al.*, 2013; Fan *et al.*, 2008a).

The differential equations of motion for an anisotropic material can be defined using the formalism for eigenvalues problems by:

$$C_{ihjl} \frac{\partial^2 U_j}{\partial x_k \partial x_l} + I(C_{i3jh} + C_{ihj3}) \frac{\partial(kU_j)}{\partial x_k} - kC_{i3j3} (kU_j) + \rho \omega^2 \delta_{ij} U_j = 0 \quad (\text{A I-1})$$

where δ_{ij} is the Kronecker symbol and the subscripts $j=1, 2, 3$ and $h, l=1, 2$. The same formalism can be expressed using a partial differential equation in the finite element software:

$$\lambda^2 e_a \mathbf{u} - \lambda d_a \mathbf{u} + \nabla \cdot (-c \nabla \mathbf{u} - \alpha \mathbf{u} + \gamma) + \beta \cdot \nabla \mathbf{u} + a \mathbf{u} = 0 \quad (\text{A I-2})$$

where \mathbf{u} represents the variables to be determined. If one considers $\gamma=0$ and $e_a=0$, the coefficients c, α, β, a and d_a can be described in term of the Young's modulus E , the Poisson's

ratio ν , the density ρ and angular frequency ω in order to match with equation A I-1. A more detailed description and the definition of each coefficient can be found in the literature Predoi *et al.* (2007). Equation A I-1 can be solved for a certain angular frequency ω , resulting in an infinite number of complex wavenumbers k as the eigenvalue solutions of the equation. The dispersion can be obtained by selecting all the propagative modes among the wavenumber solutions for a desired number of frequencies. Figure I-2c shows a typical dispersion curve of the two waveguides obtained by the SAFE method.

2.2.1 Application to radius bone

The numerical dispersion curves of the radius bone waveguide were calculated in order to understand the responses obtained from the FE simulations. The boundaries of the waveguide were extracted from the same 3D model used in the previous step. Two different regions were selected for the SAFE simulations: the distal radius and long bone region as shown in the Figure I-2a and Figure I-2b, respectively. The cross-sections were meshed using triangular elements with a maximum size of 0.5 mm. Although the focus of this paper is the assessment of the trabecular bone, the simulation of the dispersion curves of the long bone region is also relevant since the signal will be received along the long bone. The bone materials were modeled using the same properties presented in Table I-1.

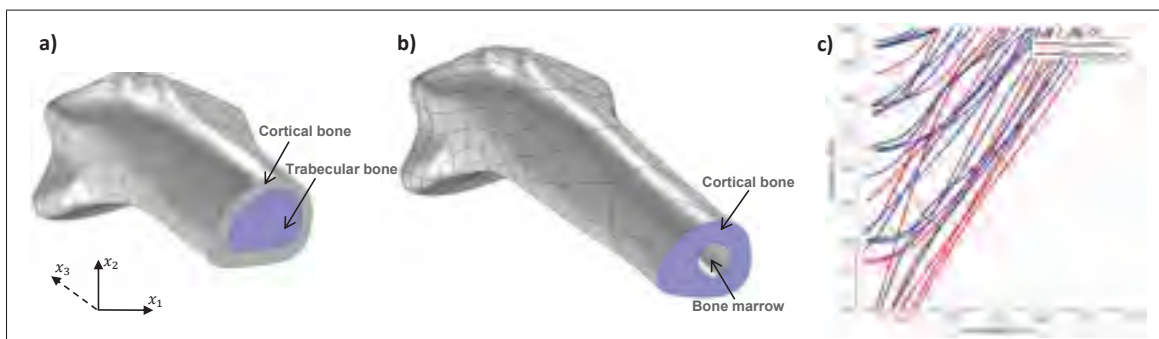


Figure-A I-2 a) Boundaries of the waveguide defined from different regions: a) Distal 1/3 radius and b) Middle 1/3 radius. c) Typical dispersion curves of the two waveguides obtained by the SAFE method.

3. Results and Discussion

3.1 Mode identification

Figure I-3a shows a snapshot of the out of plane displacement (z direction) obtained for the simulations using the properties in Table I-1. The time responses received at each receiver are shown in Figure I-3b while the obtained 2D-FFT map is shown in Figure I-3c. The continuous lines show the numerical dispersion curves computed for the two regions of the radius bone using the SAFE method. The results show that different modes in the frequency range between 50 kHz and 90 kHz are propagating in the radius waveguide since the amplitudes in the 2D-FFT map are consistent with the dispersion curves of the simulated modes.

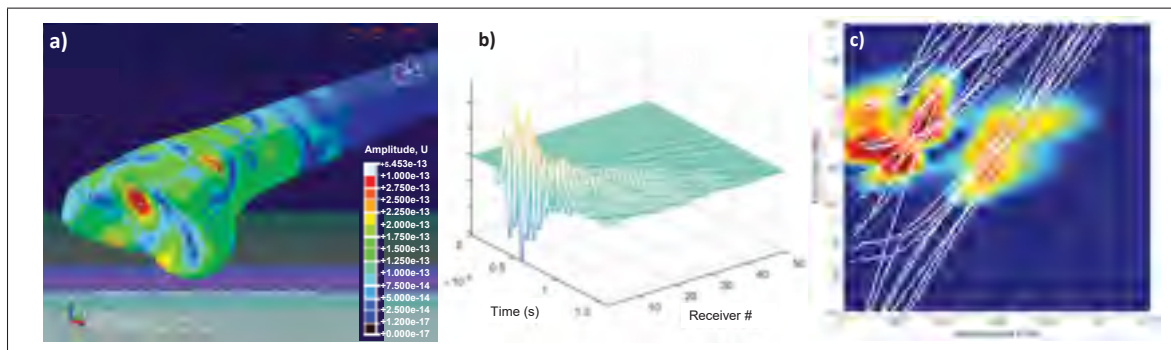


Figure-A I-3 Results related to the simulations using the properties in Table I-1. a) Snapshot of the out of plane displacement (z direction). b) Time responses received at each receiver, where #1 is the receiver located closer to the extremity where the excitation was performed. c) 2D-FFT map compared to the simulated dispersion curves.

3.2 Sensitivity study

Figure I-4 show the 2D-FFTs maps obtained by the simulations using different trabecular bone properties. A clear difference in the distribution of the intensities can be observed by comparing the different simulations. Such a qualitative approach suggests that ultrasonic guided waves are sensitive to the properties of trabecular bone. Further investigations need to be performed in order to quantify the results.

4. Conclusion

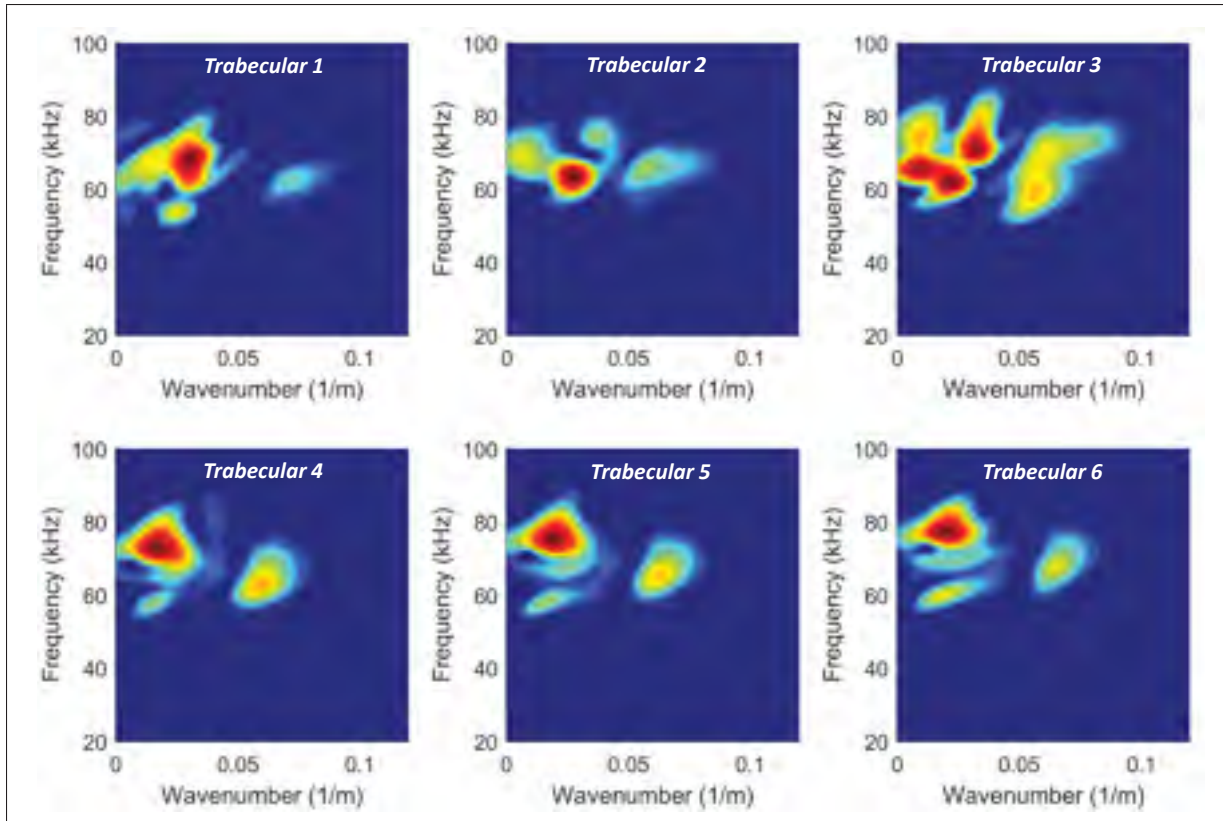


Figure-A I-4 2D-FFTs maps obtained by the simulations using different properties for the trabecular bone.

The feasibility of the ultrasonic guided waves method to assess the mechanical properties of trabecular bone at the distal radius was investigated using an axial transmission configuration. The results showed that different modes propagate in the radius waveguide when excited at the extremity of the distal region and received on the surface of the long bone. The propagating modes were sensitive to changes in the trabecular bone properties, and the method was shown to be sensitive to changes in the trabecular bone properties at the distal radius. However, future work needs to be performed using more realistic bone properties, and a quantitative approach needs to be considered to evaluate the changes observed in the propagation of the ultrasonic guided waves.

APPENDIX II

INVERSE CHARACTERIZATION OF ADHESIVE SHEAR MODULUS IN BONDED STIFFENERS USING ULTRASONIC GUIDED WAVES

Daniel Pereira^{1 4}, Julio Fernandes^{3 4}, Pierre Belanger^{1 4}

¹ Département de Génie Mécanique, École de Technologie Supérieure,
1100 Notre-Dame Ouest, Montréal, Québec, Canada H3C 1K3

³ Department of Surgery, Université de Montréal, 2900 Boulevard Edouard-Montpetit,
Montreal, Quebec, H3T1J4 Canada

⁴ Centre de recherche l'Hôpital du Sacré-Coeur de Montréal, 5400 Boul Gouin O, Montreal,
Quebec, H4J1C5 Canada

Manuscript submitted to the Proceedings of the 45th Annual Review of Progress in
Quantitative Nondestructive Evaluation, Burlington, Vermont, US, July 2018.

Abstract Adhesively bonded stiffeners are widely used in aerospace structures. A well-cured bond can increase structural stiffness, and, consequently, enhance the performance of the entire structure. The feasibility of ultrasonic feature-guided wave modes for the inspection of the bond line adhesion in difficult-to-access regions has been already investigated in the literature. However, due to the complexity of the guide wave phenomena in the bond line region, a more comprehensive methodology to identify the curing state remains an open issue. This work introduces a multi-mode and multi-frequency inverse method for the characterization of stiffener bonded line using Semi-Analytical Finite Element (SAFE). Experiments were conducted on a T-shaped stiffener bonded to an aluminum plate. The feature-guided modes were excited using a piezoelectric shear transducer and measured using a laser interferometer at several times along a period of four days. The experimental dispersion curves were computed from the measured data and then systematically compared to the numerical solutions obtained with the SAFE model. At each measurement, the shear modulus of the adhesive material could be estimated by iteratively minimizing the error between the experimental and numerical data. The results showed an abrupt increase in the shear modulus from the first to the second day, suggesting that the end of the curing processes was achieved. In general, the inverse scheme

presented in this work was shown to be very sensitive, being able to distinguish differences of 5% in the shear modulus.

1. Introduction

Composite materials can provide a much better strength-to-weight ratio than metal. Therefore, they have become a key substitute to produce critical components in different industrial field, such as aerospace, oil and gas and energy. In this context, adhesively bonded composite stiffeners are widely used to enhance the performance of the entire structure. For instance, a well-cured bond can provide the adhesion between a composite plate and an aluminum stiffener in order to increase structural stiffness. The feasibility of ultrasonic feature-guided wave modes for the inspection of the bond line adhesion of stiffeners has been already investigated in the literature using Semi-Analytical Finite Element (SAFE) method. However, due to the complexity of the guide wave phenomena in the bond line region, a more comprehensive methodology to classify the adhesion and curing state of the bond line remains an open issue. This work introduces a multi-mode and multi-frequency inverse method for the characterization of stiffener bonded line using Semi-Analytical Finite Element (SAFE) model.

The paper begins with the description of the experimental setup and the signal processing. The SAFE method is then briefly introduced. The finite element model and the inversion method are discussed. Results are then presented and discussed.

2. Experimental measurements and signal processing

The experimental data acquisition was performed by Zheng Fan (Nanyang Technological University) and Michel Castaings (Institut National Polytechnique de Bordeaux) and kindly shared with our group. In summary, the acquisition was conducted on a T-shaped stiffener bonded to an aluminum plate. A photo of the experimental setup as well as a typical dispersion curve are shown in Figure II-1. The feature-guided modes were excited using a piezoelectric shear transducer and measured using a laser interferometer at several times along a period of four days.

The detailed description of the experimental procedure can be found in a previously published paper (Fan *et al.*, 2013).

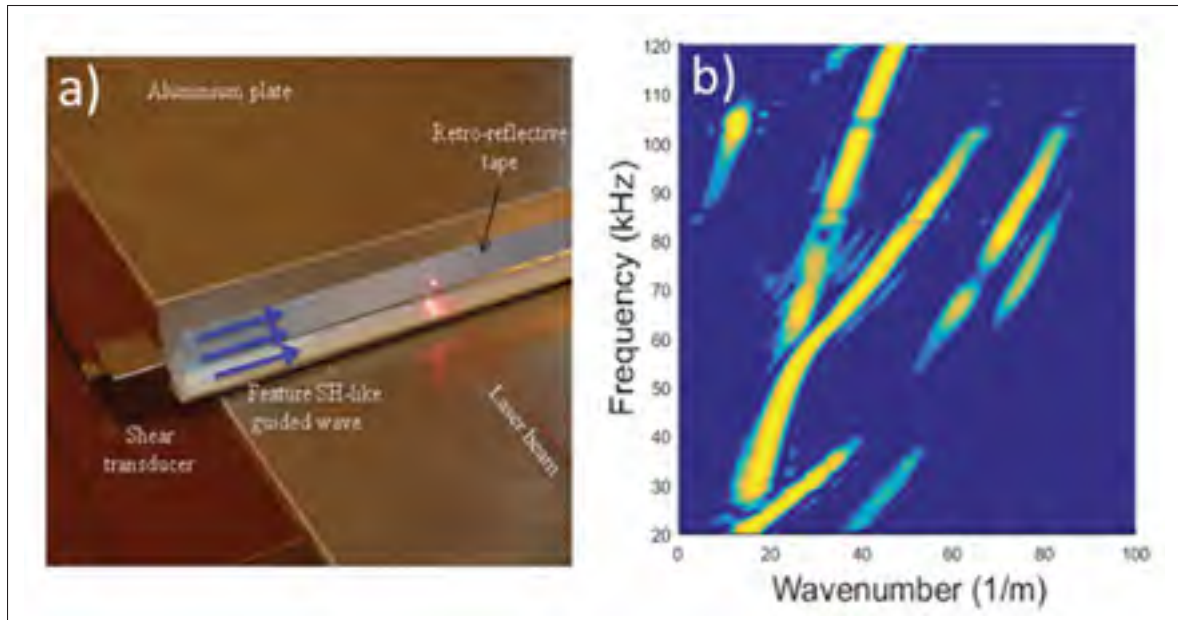


Figure-A II-1 a) The experimental setup used to perform the acquisition of the dispersion curves (adapted from Fan *et al.* (2013)). b) Typical dispersion curve obtained after processing the data using the 2D-FFT.

The experimental time domain signals were processed using the 2D-FFT in order to calculate the intensities of the propagating modes in the frequency-wavenumber diagram. The experimental dispersion curves were then systematically compared to the numerical solutions obtained with the SAFE model as described next.

3. Semi-analytical finite element method

The Semi-Analytical Finite Element (SAFE) has been extensively used to study uniform waveguides of arbitrary cross-sections (Hayashi *et al.*, 2003; Treysede & Frikha, 2008; Fan *et al.*, 2008b; Mazzotti *et al.*, 2013; Bartoli *et al.*, 2006). The main advantage of this method when compared to conventional finite element modeling is the fact that only the cross-section needs to be modeled and meshed (Predoi *et al.*, 2007). The waves are assumed to propagate harmonically in the axial direction (z direction) of the waveguide. The displacement vector can be

described by equation (A II-1), where k is the wavenumber and ω is the angular frequency and $i=1,2,3$.

$$u_g(x, y, z, t) = U_g(x, y) e^{-i(kz - \omega t)}, \quad i = \sqrt{-1} \quad (\text{A II-1})$$

Considering the mass density ρ and the elastic constants C_{ijkl} , the differential equations of motion for an anisotropic material can be defined using the formalism for eigenvalues problems by equation (A II-2), where the indices $j=1,2,3$ and $k, l=1,2$ and where δ_{ij} is the Kronecker symbol.

$$C_{ghjl} \frac{\partial^2 U_j}{\partial x_h \partial x_l} + i(C_{g3jl} + C_{ghj3}) \frac{\partial(kU_j)}{\partial x_h} - kC_{g3j3} (kU_j) + \rho \omega^2 \delta_{gj} U_j = 0, \quad (\text{A II-2})$$

In a commercial finite element software, the same formalism can be expressed by equation (A II-3), where u represents the variables to be determined. Comparing the two formalism and considering $\gamma=0$ and $e_a=0$, the coefficients c , α , β , a and d_a in equation (A II-3), can be defined in term of stiffness properties, ρ and ω in order to match to the equation (A II-2).

$$\lambda^2 e_a u - \lambda d_a u + \nabla \cdot (-c \nabla u - \alpha u + \gamma) + \beta \cdot \nabla u + a u = 0 \quad (\text{A II-3})$$

The detailed description of the coefficient used in this study is given by Predoi *et al.* (2007). Thus, equation (A II-3) can be solved for a certain angular frequency ω resulting in an infinite number of complex wavenumber k as the eigenvalues solutions of the equation.

3.1 Stiffener model

In this study, a T-shaped aluminum stiffener coupled to an aluminum plate by an adhesive layer (Figure II-2a)) was implemented as a forward model to match the experimental dispersion curves. In short, an equivalent plate-adhesive-stiffener geometry and material properties

(Figure II-1b)) was used in order to reproduce the experimental configuration (Figure II-1a)). The thickness (0.5 mm) and density (1040 kg/m^3) of the adhesive layer were kept constant in order to limit the size of the inverse problem and, therefore, reduce the computational time. The adhesive shear modulus (C_{66}) was set as the unknown parameter to be optimized.

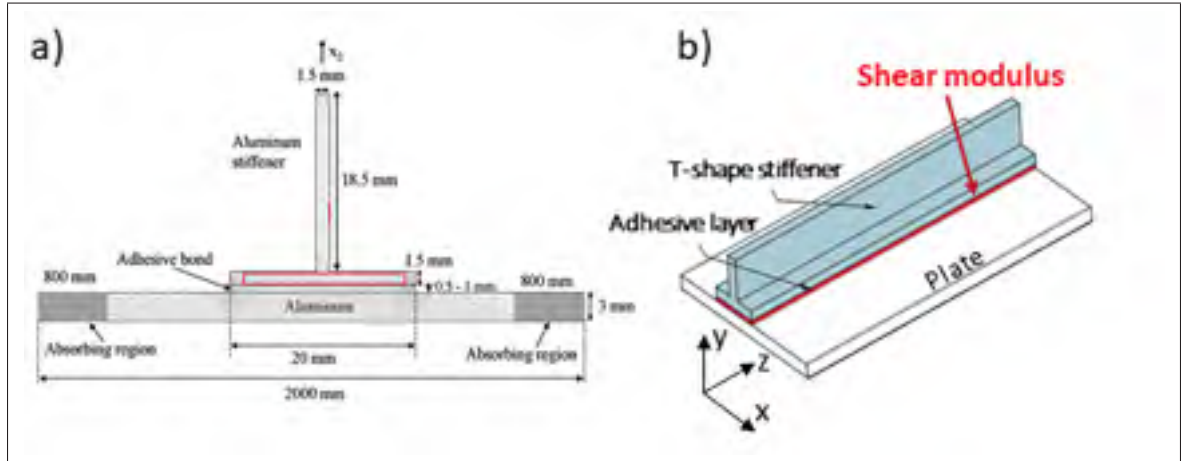


Figure-A II-2 a) T-shaped aluminum stiffener coupled to an aluminum plate by an adhesive layer; b) Forward model geometry (adapted from)

3.2 Modal excitability

For the longitudinal direction (z) the modal excitability associated to the n^{th} mode (E_n) and responsible for the displacement in the shear direction (x) can be estimated based on the shear displacement at the surface of the excitation region $u_{x(e)}$ (red rectangle in Figure II-2b) and the acquisition region $u_{x(a)}$ (red line in Figure II-2b) using the equation (A II-4), where P is the power flow associated with the mode shape.

$$E_n = \frac{ik\omega}{8} \left(\frac{u_{x(e)}^* u_{x(a)}}{P} \right) \quad (\text{A II-4})$$

Figure II-3 shows (a) the solutions to the SAFE simulation of the bonded stiffener and (b) the associated modal excitability. Figure II-3c shows the same SAFE solutions as (a) but after

applying a threshold to keep only the modes with the highest excitability. In Figure II-3c the SAFE solutions are overlaid onto an experimental dispersion curve.

4. Inversion scheme

For each measurement, the mechanical condition associated with the bond line can be defined by choosing an appropriate shear modulus for the adhesive material. Such a model-based inverse approach requires the implementation of a cost function into an optimization procedure to find the optimal value for the shear modulus. The following subsections describe the cost function and the optimization routine using a genetic algorithm employed in this study.

4.1 Cost function

In this study, the misfit for each simulated mode is defined at each frequency by the product between the modal excitability and the amplitude observed experimentally, where E_n denotes the modal excitability associated to n^{th} mode and $A(k_n)$ denotes the experimental amplitude observed at the wavenumber (k_n) associated to the n^{th} mode.

$$J = - \sum_{f=f_s:f_e} \sum_{n=1:M} E(k_n) \cdot A(k_n) \quad (\text{A II-5})$$

4.2 Genetic algorithm

The inverse problem assumes that the condition of any given condition in the bonded line can be estimated by optimization of the shear modulus (C_{66}). Genetic algorithm (GA) are commonly adopted as an alternative to solve this inverse problem by running a limited number of cases. The GA optimization technique is based on survival competition mechanisms between the members of a population defined from natural selection and genetics rules. In contrast to gradient-based optimization techniques, it has the advantage of finding the global minimum without the need for an accurate initial guess for the model parameters. Furthermore, the

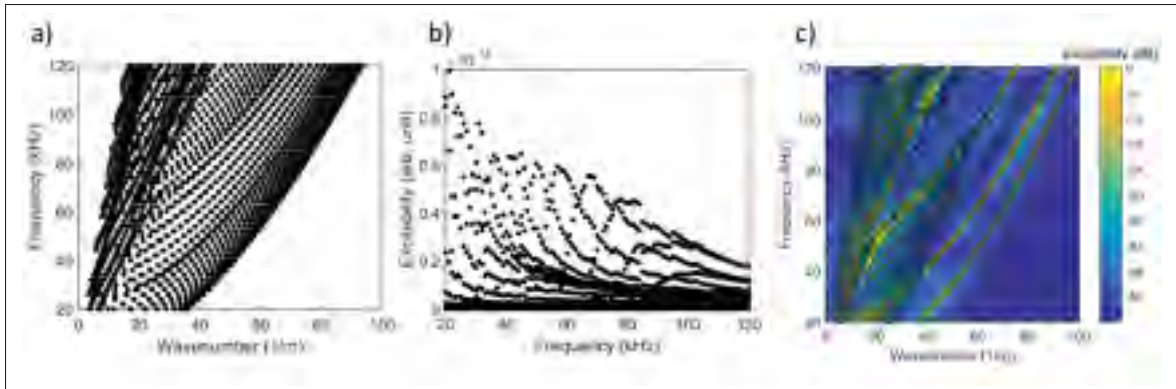


Figure-A II-3 a) Typically solutions of the SAFE simulation for the bonded stiffener. b) The associated modal excitability computed using the equation (A II-4). c) The highest excitability modes (same SAFE solutions as (a) but after applying a threshold) overlaid onto an experimental dispersion curve.

optimization mechanisms allow performing the search in parallel, which is of particular interest when using a relatively expensive model-based routine such as the SAFE method.

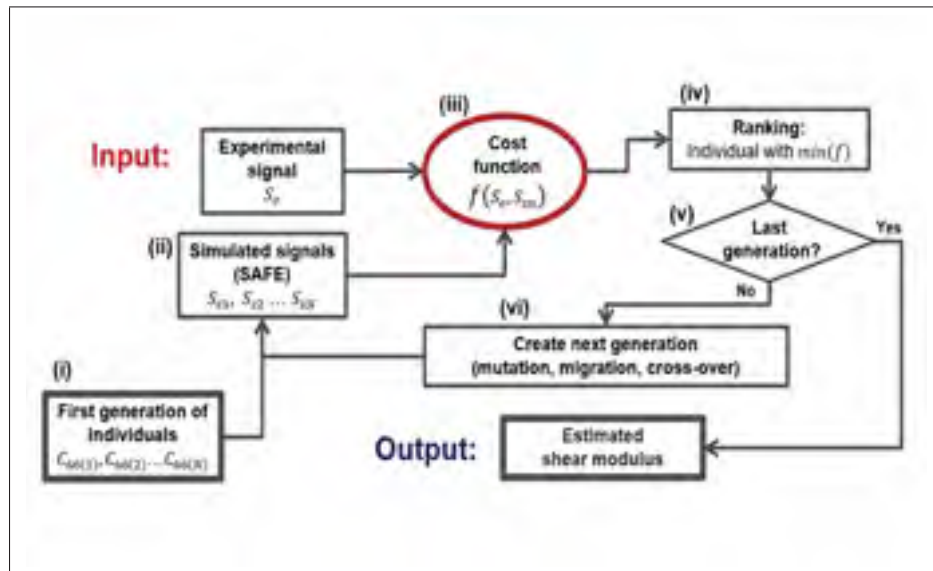


Figure-A II-4 Flowchart of the GA operations used to solve a model-based inverse problem.

The basic idea of solving a model-based inverse problem using GA is summarized as a flowchart in Figure II-4 and described in more details in the following steps:

- I. An initial population of N individuals with randomly generated values for C_{66} (restricted to the constraints in Table II-1) is created.
- II. The shear modulus $C_{66(n)}$ associated to each individual n is transmitted to the model solver so as N simulated data are computed (S_{s1}, S_{s2}, S_{sN})
- III. The objective function J (equation (A II-5)) is then evaluated against the experimental data (S_e) for each of the simulated data (S_{sn}).
- IV. The individuals are ranked according to the value obtained for $J(S_e, S_{sn})$.
- V. The stopping criterion of the GA scheme is checked (maximum number of generation, in this paper). If this criterion is satisfied, the individual with the minimum $J(S_e, S_{sn})$ is returned as the winner providing the estimated shear modulus.
- VI. If not, a new generation is created by applying genetic operators to the individuals of the previous generation based on the ranking. The algorithm restarts from step (ii) and the procedure continues until the stopping criterion is reached.

Table-A II-1 Setting for the genetic algorithm optimization procedure.

Properties	Range	Step
C_{66} (MPa)	1 - 1000	2
Frequency (kHz)	20 - 120	2
Number of individuals	20	
Number of generations	10	

5. Results and discussion

Figure II-5 shows the experimental data with the SAFE solution overlaid (circles) computed using the optimal shear modulus for three different times of acquisition (initial, intermediate and final stages). As observed, a remarkable agreement was found between the experimental data and the SAFE model for all three stages. Most of the experimental data were matched by a combination of several high excitability modes segments ($E_n > -30\text{dB}$).

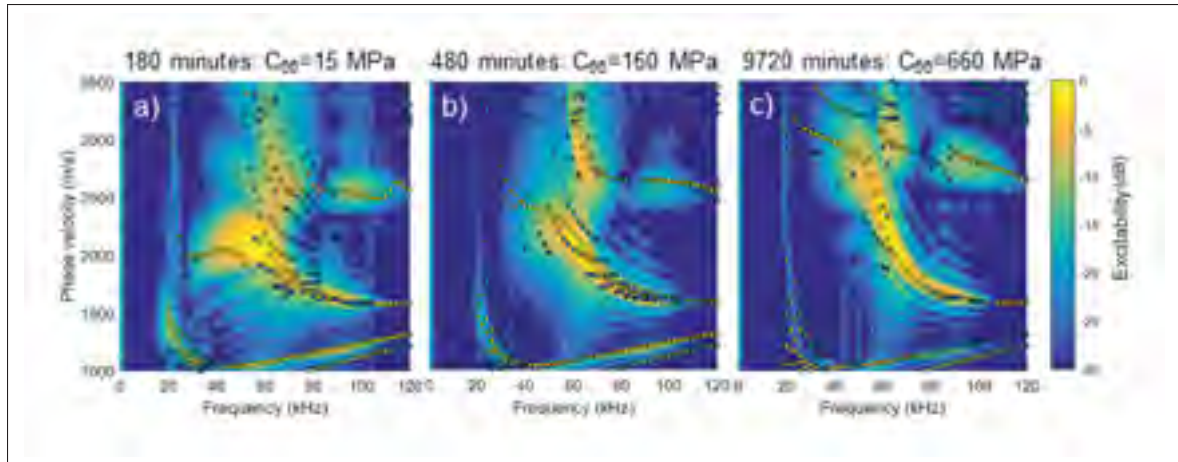


Figure-A II-5 Experimental dispersion curves along with the SAFE solution (circles) computed using the optimal shear modulus for three different stages of acquisition: a) initial, b) intermediate and c) final.

Figure II-6 shows the predicted shear modulus varying along four days of acquisition. The shear modulus was found to be varying between 8 MPa and 660 MPa. An abrupt increase in the shear modulus was observed from 400 minutes to 1150 minutes, which is in accordance with the expected time for the transition to the glassy state (dotted line in Figure II-6) of the resin applied in this work (DGEBA-PAMAM) (Budzik *et al.*, 2012). Thus, we can assume that the method was able to monitor the curing process by monitoring variations in the mechanical properties of the adhesive layer.

6. Conclusion

An inverse routine using a SAFE model was successfully implemented to determine the shear modulus of a stiffener bond line. The excitability curves played a key role in determining the most relevant modes. The results showed an abrupt increase in the shear modulus from the first to the second day, suggesting that the end of the curing processes was achieved. In general, the inverse scheme presented in this work was shown to be very sensitive, being able to distinguish variation in the shear modulus of the order of 10 MPa. The method is now ready to be tested on *in-situ* stiffener bonded structures. Furthermore, the inverse procedure introduced in this work can be considered for other applications.

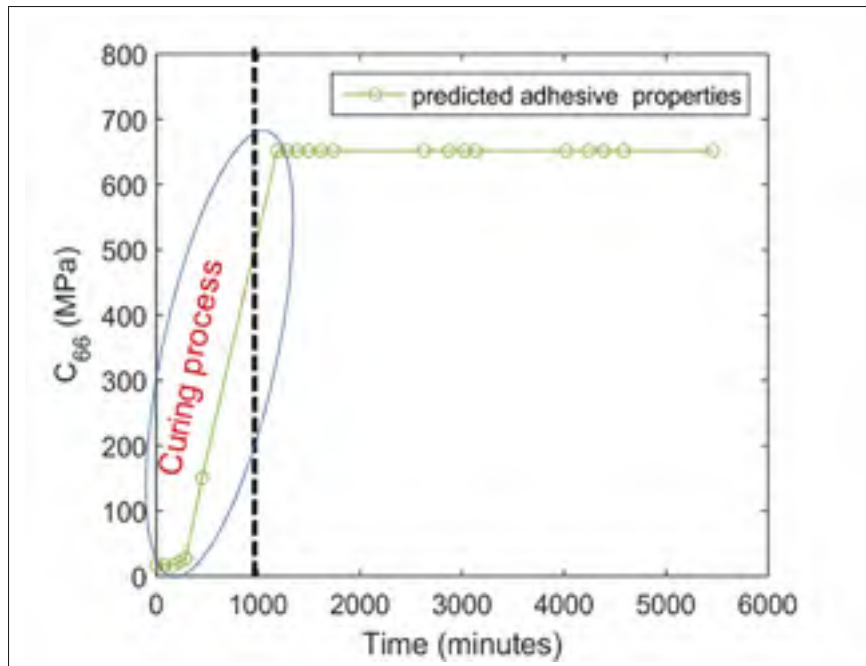


Figure-A II-6 Predicted shear modulus varying along four days of acquisition.

7. Acknowledgments

Special acknowledgment to Zheng Fan and Michel Castaings for providing the experimental data used in this study as well as their useful insights regarding the problem.

BIBLIOGRAPHY

- (1991). *Consensus development conference: prophylaxis and treatment of osteoporosis* (Report n°1). Elsevier. Consulted at [https://doi.org/10.1016/0002-9343\(91\)90512-V](https://doi.org/10.1016/0002-9343(91)90512-V).
- (1994). *Assessment of fracture risk and its application to screening for postmenopausal osteoporosis. Report of a WHO Study Group*. Consulted at <http://www.who.int/iris/handle/10665/39142>.
- (2004). *Bone Health and Osteoporosis: A Report of the Surgeon General*. Consulted at <http://www.ncbi.nlm.nih.gov/books/NBK45513/>.
- Agostini, V., Delsanto, P. P., Genesio, I. & Olivero, D. (2003). Simulation of Lamb wave propagation for the characterization of complex structures. *IEEE Trans Ultrason Ferroelectr Freq Control*, 50(4), 441-8. Consulted at <http://dx.doi.org/>.
- Alleyne, D. N. & Cawley, P. (1990, Dec). A 2-dimensional Fourier transform method for the quantitative measurement of Lamb modes. *Ultrasonics Symposium, 1990. Proceedings., IEEE 1990*, pp. 1143-1146 vol.2. doi: 10.1109/ULTSYM.1990.171541.
- Barkmann, R., Kantorovich, E., Singal, C., Hans, D., Genant, H. K., Heller, M. & Glüer, C.-C. (2000). A New Method for Quantitative Ultrasound Measurements at Multiple Skeletal Sites. *Journal of Clinical Densitometry*, 3(1), 1 - 7. doi: <http://dx.doi.org/10.1385/JCD:3:1:001>.
- Bartoli, I., Marzani, A., Matt, H., Lanza di Scalea, F. & Viola, E. (2006). Modeling wave propagation in damped waveguides of arbitrary cross-section. *Health Monitoring and Smart Nondestructive Evaluation of Structural and Biological Systems V*, 6177, 92-103. doi: [doi:10.1117/12.640032](https://doi.org/10.1117/12.640032).
- Bessette, L., Ste-Marie, L. G., Jean, S., Davison, K. S., Beaulieu, M., Baranci, M., Bessant, J. & Brown, J. P. (2008). The care gap in diagnosis and treatment of women with a fragility fracture. *Osteoporos Int*, 19(1), 79-86. doi: [10.1007/s00198-007-0426-9](https://doi.org/10.1007/s00198-007-0426-9).
- Bochud, N., Vallet, Q., Bala, Y., Follet, H., Minonzio, J.-G. & Laugier, P. (2016). Genetic algorithms-based inversion of multimode guided waves for cortical bone characterization. *Physics in Medicine & Biology*, 61(19), 6953. Consulted at <http://stacks.iop.org/0031-9155/61/i=19/a=6953>.
- Bochud, N., Vallet, Q., Minonzio, J.-G. & Laugier, P. (2017). Predicting bone strength with ultrasonic guided waves. *Scientific Reports*, 7, 43628 EP -. Consulted at <http://dx.doi.org/10.1038/srep43628>. Article.
- Bossy, E. & Talmant, M. (2015). 2D Simulation of the Axial Transmission Technique on a Cortical Bone Plate. 69-76. doi: [10.1007/978-1-4419-8606-1_9](https://doi.org/10.1007/978-1-4419-8606-1_9).

- Bossy, E., Talmant, M. & Laugier, P. (2002). Effect of bone cortical thickness on velocity measurements using ultrasonic axial transmission: A 2D simulation study. *The Journal of the Acoustical Society of America*, 112(1), 297-307. doi: <http://dx.doi.org/10.1121/1.1480836>.
- Bossy, E., Talmant, M. & Laugier, P. (2004). Three-dimensional simulations of ultrasonic axial transmission velocity measurement on cortical bone models. *The Journal of the Acoustical Society of America*, 115(5), 2314-2324. doi: <http://dx.doi.org/10.1121/1.1689960>.
- Breban, S., Padilla, F., Fujisawa, Y., Mano, I., Matsukawa, M., Benhamou, C. L., Otani, T., Laugier, P. & Chappard, C. (2010). Trabecular and cortical bone separately assessed at radius with a new ultrasound device, in a young adult population with various physical activities. 46, 1620-5. doi: 10.1016/j.bone.2010.03.005.
- Budzik, M. K., Mascaro, B., Jumel, J., Castaings, M. & Shanahan, M. (2012). Monitoring of Crosslinking of a DGEBA-PAMAM Adhesive using Mechanical and Ultrasound Techniques. *International Journal of Adhesion and Adhesives*, 35, 120-128. doi: 10.1016/j.ijadhadh.2012.02.009.
- Burt, L. A., Macdonald, H. M., Hanley, D. A. & Boyd, S. K. (2014). Bone microarchitecture and strength of the radius and tibia in a reference population of young adults: an HR-pQCT study. *Arch Osteoporos*, 9(1), 183. doi: 10.1007/s11657-014-0183-2.
- Castellazzi, G., De Marchi, L., Krysl, P. & Marzani, A. (2013). *Quantitative simulation of wave propagation in a human leg to support the ultrasonic noninvasive assessment of human bones*, 8695, 86952G-86952G-10. doi: 10.1117/12.2009592.
- Cavani, F., Giavaresi, G., Fini, M., Bertoni, L., de Terlizzi, F., Barkmann, R. & Cane, V. (2008). Influence of density, elasticity, and structure on ultrasound transmission through trabecular bone cylinders. *IEEE Trans Ultrason Ferroelectr Freq Control*, 55(7), 1465-72. doi: 10.1109/tuffc.2008.821.
- Cheeke, J. D. N. (2012). *Fundamentals and Applications of Ultrasonic Waves, Second Edition*. CRC Press.
- Chen, J. & Su, Z. (2014). On ultrasound waves guided by bones with coupled soft tissues: A mechanism study and in vitro calibration. *Ultrasonics*, 54(5), 1186 - 1196. doi: <https://doi.org/10.1016/j.ultras.2013.08.002>.
- Chimenti, D. E. (1997). Guided Waves in Plates and Their Use in Materials Characterization. *Applied Mechanics Reviews*, 50(5), 247-284. doi: 10.1115/1.3101707.
- Collin, R. E. (1990). *Field Theory of Guided Waves*. Wiley-IEEE Press.
- Damilakis, J., Adams, J. E., Guglielmi, G. & Link, T. M. (2010). Radiation exposure in X-ray-based imaging techniques used in osteoporosis. In *Eur Radiol* (vol. 20, pp. 2707-14). doi: 10.1007/s00330-010-1845-0.

- Dempster, D. W. (2011). Osteoporosis and the burden of osteoporosis-related fractures. *Am J Manag Care*, 17 Suppl 6, S164-9. Consulted at <http://dx.doi.org/>.
- DG, S., WS, B., MC, N. & et al. (1991). Which fractures are associated with low appendicular bone mass in elderly women? *Annals of Internal Medicine*, 115(11), 837-842. doi: 10.7326/0003-4819-115-11-837.
- Drozdz, M., Skelton, E., Craster, R. V. & Lowe, M. J. S. (2007). Modeling Bulk and Guided Waves in Unbounded Elastic Media Using Absorbing Layers in Commercial Finite Element Packages. *AIP Conference Proceedings*, 894(1), 87-94. doi: <http://dx.doi.org/10.1063/1.2717958>.
- Egorov, V., Tatarinov, A., Sarvazyan, N., Wood, R., Magidenko, L., Amin, S., Khosla, S., Ruh, R. J., Ruh, J. M. & Sarvazyan, A. (2014). Osteoporosis detection in postmenopausal women using axial transmission multi-frequency bone ultrasonometer: Clinical findings. *Ultrasonics*, 54(5), 1170 - 1177. doi: <https://doi.org/10.1016/j.ultras.2013.08.017>.
- Eisman, J. A., Bogoch, E. R., Dell, R., Harrington, J. T., McKinney, R. E., J., McLellan, A., Mitchell, P. J., Silverman, S., Singleton, R. & Siris, E. (2012). Making the first fracture the last fracture: ASBMR task force report on secondary fracture prevention. *J Bone Miner Res*, 27(10), 2039-46. doi: 10.1002/jbmr.1698.
- Engelke, K., Libanati, C., Liu, Y., Wang, H., Austin, M., Fuerst, T., Stampa, B., Timm, W. & Genant, H. K. (2009). Quantitative computed tomography (QCT) of the forearm using general purpose spiral whole-body CT scanners: accuracy, precision and comparison with dual-energy X-ray absorptiometry (DXA). *Bone*, 45(1), 110-8. doi: 10.1016/j.bone.2009.03.669.
- Fan, Z., Lowe, M. J. S., Castaings, M. & Bacon, C. (2008a). Torsional waves propagation along a waveguide of arbitrary cross section immersed in a perfect fluid. *The Journal of the Acoustical Society of America*, 124(4), 2002-2010. doi: <http://dx.doi.org/10.1121/1.2968677>.
- Fan, Z., Lowe, M. J. S., Castaings, M. & Bacon, C. (2008b). Prediction of the Propagation and Leakage of Torsional Waves in a Waveguide of Arbitrary Cross-Section Immersed in a Fluid. *Review of Progress in Quantitative Nondestructive Evaluation*, 975, 1567-1574. doi: 10.1063/1.2902623.
- Fan, Z., Lowe, M. J. S., Castaings, M. & Bacon, C. (2008c). Torsional waves propagation along a waveguide of arbitrary cross section immersed in a perfect fluid. *The Journal of the Acoustical Society of America*, 124(4), 2002-2010. doi: 10.1121/1.2968677.
- Fan, Z., Castaings, M., Lowe, M., Biateau, C. & Fromme, P. (2013). Feature-guided waves for monitoring adhesive shear modulus in bonded stiffeners. *NDT and E International*, 54, 96 - 102. doi: <https://doi.org/10.1016/j.ndteint.2012.12.006>.

- Foiret, J., Minonzio, J., Chappard, C., Talmant, M. & Laugier, P. (2014). Combined estimation of thickness and velocities using ultrasound guided waves: a pioneering study on in vitro cortical bone samples. *IEEE Transactions on Ultrasonics, Ferroelectrics, and Frequency Control*, 61(9), 1478-1488. doi: 10.1109/TUFFC.2014.3062.
- Gavrić, L. (1995). Computation of propagative waves in free rail using a finite element technique. *Journal of Sound and Vibration*, 185(3), 531 - 543. doi: <http://dx.doi.org/10.1006/jsvi.1995.0398>.
- Gehlbach, S., Saag, K. G., Adachi, J. D., Hooven, F. H., Flahive, J., Boonen, S., Chapurlat, R. D., Compston, J. E., Cooper, C., Diez-Perez, A., Greenspan, S. L., LaCroix, A. Z., Netelenbos, J. C., Pfeilschifter, J., Rossini, M., Roux, C., Sambrook, P. N., Silverman, S., Siris, E. S., Watts, N. B. & Lindsay, R. (2012). Previous fractures at multiple sites increase the risk for subsequent fractures: the Global Longitudinal Study of Osteoporosis in Women. *J Bone Miner Res*, 27(3), 645-53. doi: 10.1002/jbmr.1476.
- Giangregorio, L., Papaioannou, A. & Zytaruk, N. (2006). Fragility Fractures and the Osteoporosis Care Gap: An International Phenomenon. *Seminars in Arthritis and Rheumatism*, 35(5), 293-305. doi: 10.1016/j.semarthrit.2005.11.001.
- Gluer, C. (2008). A new quality of bone ultrasound research. *IEEE Transactions on Ultrasonics, Ferroelectrics, and Frequency Control*, 55(7), 1524-1528. doi: 10.1109/TUFFC.2008.828.
- Gluer, C. C. (1997). Quantitative Ultrasound Techniques for the Assessment of Osteoporosis: Expert Agreement on Current Status. *Journal of Bone and Mineral Research*, 12(8), 1280-1288. doi: 10.1359/jbmr.1997.12.8.1280.
- Government of Canada, P. H. A. o. C. (2010). What is the impact of osteoporosis in Canada and what are Canadians doing to maintain healthy bones? Consulted at <http://www.phac-aspc.gc.ca/cd-mc/osteoporosis-osteoporose/>.
- Griffith, J. F. & Genant, H. K. (2011). New Imaging Modalities in Bone. In *Curr Rheumatol Rep* (vol. 13, pp. 241-50). doi: 10.1007/s11926-011-0174-x.
- Haba, Y., Skripitz, R., Lindner, T., Köckerling, M., Fritsche, A., Mittelmeier, W. & Bader, R. (2016). Bone Mineral Densities and Mechanical Properties of Retrieved Femoral Bone Samples in relation to Bone Mineral Densities Measured in the Respective Patients. *The Scientific World Journal*, 2012, 1-7.
- Haiat, G., Naili, S., Grimal, Q., Talmant, M., Desceliers, C. & Soize, C. (2009). Influence of a gradient of material properties on ultrasonic wave propagation in cortical bone: Application to axial transmission. *The Journal of the Acoustical Society of America*, 125(6), 4043-4052. doi: <http://dx.doi.org/10.1121/1.3117445>.
- Haiat, G., Naili, S., Ba Vu, M., Desceliers, C. & Soize, C. (2011). Equivalent contributing depth investigated by a lateral wave with axial transmission in viscoelastic

- cortical bone. *The Journal of the Acoustical Society of America*, 129(4), 114-120. doi: <http://dx.doi.org/10.1121/1.3554719>.
- Hans, D., Srivastav, S. K., Singal, C., Barkmann, R., Njeh, C. F., Kantorovich, E., Glüer, C. C. & Genant, H. K. (1999). Does Combining the Results from Multiple Bone Sites Measured by a New Quantitative Ultrasound Device Improve Discrimination of Hip Fracture? *Journal of Bone and Mineral Research*, 14(4), 644-651. doi: 10.1359/jbmr.1999.14.4.644.
- Hayashi, T., Song, W.-J. & Rose, J. L. (2003). Guided wave dispersion curves for a bar with an arbitrary cross-section, a rod and rail example. *Ultrasonics*, 41(3), 175 - 183. doi: [http://dx.doi.org/10.1016/S0041-624X\(03\)00097-0](http://dx.doi.org/10.1016/S0041-624X(03)00097-0).
- Hernlund, E., Svedbom, A., Ivergård, M., Compston, J., Cooper, C., Stenmark, J., McCloskey, E. V., Jönsson, B. & Kanis, J. A. (2013). Osteoporosis in the European Union: medical management, epidemiology and economic burden. *Archives of Osteoporosis*, 8(1), 136. doi: 10.1007/s11657-013-0136-1.
- Ioannidis, G., Flahive, J., Pickard, L., Papaioannou, A., Chapurlat, R. D., Saag, K. G., Silverman, S., Anderson, F. A., J., Gehlbach, S. H., Hooven, F. H., Boonen, S., Compston, J. E., Cooper, C., Diez-Perez, A., Greenspan, S. L., Lacroix, A. Z., Lindsay, R., Netelembos, J. C., Pfeilschifter, J., Rossini, M., Roux, C., Sambrook, P. N., Siris, E. S., Watts, N. B. & Adachi, J. D. (2013). Non-hip, non-spine fractures drive healthcare utilization following a fracture: the Global Longitudinal Study of Osteoporosis in Women (GLOW). *Osteoporosis International*, 24(1), 59-67. doi: 10.1007/s00198-012-1968-z.
- Jin, J., Quek, S. T. & Wang, Q. (2003). Analytical solution of excitation of Lamb waves in plates by inter-digital transducers. *Proceedings of the Royal Society of London A: Mathematical, Physical and Engineering Sciences*, 459(2033), 1117-1134. doi: 10.1098/rspa.2002.1071.
- Kang Il Lee, B. K. C. (2015). Propagation of Ultrasonic Guided Waves in an Acrylic Plate as a Cortical-bone-mimicking Phantom. *Journal of the Korean Physical Society*, 65(11), 1858-1862. doi: 10.3938/jkps.65.1858.
- Kanis, J. A. (1994). Assessment of fracture risk and its application to screening for postmenopausal osteoporosis: Synopsis of a WHO report. *Osteoporosis International*, 4(6), 368-381. doi: 10.1007/BF01622200.
- Kassou, K., Remram, Y., Laugier, P. & Minonzio, J.-G. (2017). Dispersion characteristics of the flexural wave assessed using low frequency (50-150kHz) point-contact transducers: A feasibility study on bone-mimicking phantoms. *Ultrasonics*, 81, 1-9. doi: 10.1016/j.ultras.2017.05.008.
- Kaufman, J. J. & Einhorn, T. A. (1993). Perspectives: Ultrasound assessment of bone. *Journal of Bone and Mineral Research*, 8(5), 517-525. doi: 10.1002/jbmr.5650080502.

- Kawalilak, C. E., Johnston, J. D., Olszynski, W. P. & Kontulainen, S. A. (2014). Characterizing microarchitectural changes at the distal radius and tibia in postmenopausal women using HR-pQCT. *Osteoporos Int*, 25(8), 2057-66. doi: 10.1007/s00198-014-2719-0.
- Kilappa, V., Moilanen, P., Xu, L., Nicholson, P. H. F., Timonen, J. & Cheng, S. (2011). Low-frequency axial ultrasound velocity correlates with bone mineral density and cortical thickness in the radius and tibia in pre- and postmenopausal women. *Osteoporosis International*, 22(4), 1103–1113. doi: 10.1007/s00198-010-1273-7.
- Kilappa, V., Moilanen, P., Salmi, A., Haeggstrom, E., Zhao, Z., Myllyla, R. & Timonen, J. (2015). Tailoring the excitation of fundamental flexural guide waves in coated bone by phase-delayed array: Two-dimensional simulations. *The Journal of the Acoustical Society of America*, 137(3), 1134-1143. doi: <http://dx.doi.org/10.1121/1.4908312>.
- Kumar, R. (1972). Dispersion of Axially Symmetric Waves in Empty and Fluid-Filled Cylindrical Shells. *Acta Acustica united with Acustica*, 27(6).
- Langton, C. M. & Njeh, C. F. (2008). The measurement of broadband ultrasonic attenuation in cancellous bone—a review of the science and technology. *IEEE Trans Ultrason Ferroelectr Freq Control*, 55(7), 1546-54. doi: 10.1109/tuffc.2008.831.
- Laugier, P. & Haiat, G. (2011). *Bone Quantitative Ultrasound*. Springer Netherlands. doi: 10.1007/978-94-007-0017-8.
- Lefebvre, F., Deblock, Y., Campistron, P., Ahite, D. & Fabre, J. J. (2002). Development of a new ultrasonic technique for bone and biomaterials in vitro characterization. *Journal of Biomedical Materials Research*, 63(4), 441-446. doi: 10.1002/jbm.10261.
- Li, N., Li, X.-m., Xu, L., Sun, W.-j., Cheng, X.-g. & Tian, W. (2013). Comparison of QCT and DXA: Osteoporosis Detection Rates in Postmenopausal Women. *International Journal of Endocrinology*, 2013. doi: pmid:23606843.
- Loveday, P. W. (2008). Simulation of piezoelectric excitation of guided waves using waveguide finite elements. *IEEE Transactions on Ultrasonics, Ferroelectrics, and Frequency Control*, 55(9), 2038-2045. doi: 10.1109/TUFFC.895.
- Lowe, M. J. S. (1995). Matrix techniques for modeling ultrasonic waves in multilayered media. *IEEE Transactions on Ultrasonics, Ferroelectrics, and Frequency Control*, 42(4), 525-542. doi: 10.1109/58.393096.
- MacLaughlin, E. J., Sleeper, R. B., McNatty, D. & Raehl, C. L. (2006). Management of Age-Related Osteoporosis and Prevention of Associated Fractures. *Ther Clin Risk Manag*, 2(3), 281-95. Consulted at <http://dx.doi.org/>.
- Mano, I., Horii, K., Matsukawa, M. & Otani, T. (2013). Assessment of Bone Quality by Quantitative Ultrasound Measurement. *Transactions of Japanese Society for Medical and Biological Engineering*, 51(Supplement), M-120-M-120. doi: 10.11239/jsmbe.51.M-120.

- Mazzotti, M., Bartoli, I., Marzani, A. & Viola, E. (2013). A coupled SAFE-2.5D {BEM} approach for the dispersion analysis of damped leaky guided waves in embedded waveguides of arbitrary cross-section. *Ultrasonics*, 53(7), 1227 - 1241. doi: <http://dx.doi.org/10.1016/j.ultras.2013.03.003>.
- Minonzio, J.-G., Bochud, N., Vallet, Q., Bala, Y., Ramiandrisoa, D., Follet, H., Mitton, D. & Laugier, P. (2018). Bone cortical thickness and porosity assessment using ultrasound guided waves: An ex vivo validation study. *Bone*, 116, 111 - 119. doi: <https://doi.org/10.1016/j.bone.2018.07.018>.
- Minonzio, J.-G., Talmant, M. & Laugier, P. (2010). Guided wave phase velocity measurement using multi-emitter and multi-receiver arrays in the axial transmission configuration. doi: [doi:10.1121/1.3377085](https://doi.org/10.1121/1.3377085).
- Minonzio, J.-G., Foiret, J., Talmant, M. & Laugier, P. (2013). Axial transmission measurements of guided modes on bone phantoms and in vitro human bone specimen. *The Journal of the Acoustical Society of America*, 133(5), 3584-3584. doi: <http://dx.doi.org/10.1121/1.4806601>.
- Minonzio, J.-G., Foiret, J., Moilanen, P., Pirhonen, J., Zhao, Z., Talmant, M., Timonen, J. & Laugier, P. (2015). A free plate model can predict guided modes propagating in tubular bone-mimicking phantoms. *The Journal of the Acoustical Society of America*, 137(1), EL98-EL104. doi: [10.1121/1.4903920](https://doi.org/10.1121/1.4903920).
- Moilanen, P., Nicholson, P., Kilappa, V., Cheng, S. & Timonen, J. (2006). Measuring guided waves in long bones: Modeling and experiments in free and immersed plates. *Ultrasound in Medicine and Biology*, 32(5), 709 - 719. doi: <https://doi.org/10.1016/j.ultrasmedbio.2006.02.1402>.
- Moilanen, P., Kilappa, V., Timonen, J., Salmi, A., Karppinen, P., Hæggström, E., Zhao, Z. & Myllylä, R. (2013, July). Photo-acoustic phase-delayed excitation of guided waves in coated bone phantoms. *2013 IEEE International Ultrasonics Symposium (IUS)*, pp. 2080-2083. doi: [10.1109/ULTSYM.2013.0531](https://doi.org/10.1109/ULTSYM.2013.0531).
- Moilanen, P., Nicholson, P. H., Kilappa, V., Cheng, S. & Timonen, J. (2007a). Assessment of the cortical bone thickness using ultrasonic guided waves: Modelling and in vitro study. *Ultrasound in Medicine & Biology*, 33(2), 254 - 262. doi: <http://dx.doi.org/10.1016/j.ultrasmedbio.2006.07.038>.
- Moilanen, P., Talmant, M., Nicholson, P. H. F., Cheng, S., Timonen, J. & Laugier, P. (2007b). Ultrasonically determined thickness of long cortical bones: Three-dimensional simulations of in vitro experiments. *The Journal of the Acoustical Society of America*, 122(4), 2439-2445. doi: <http://dx.doi.org/10.1121/1.2769619>.
- Moreau, L., Minonzio, J.-G., Talmant, M. & Laugier, P. (2014). Measuring the wavenumber of guided modes in waveguides with linearly varying thickness. *The Journal of the Acoustical Society of America*, 135(5), 2614-2624. doi: <http://dx.doi.org/10.1121/1.4869691>.

- Muller, M., Moilanen, P., Bossy, E., Nicholson, P., Kilappa, V., Timonen, J., Talmant, M., Cheng, S. & Laugier, P. (2005). Comparison of three ultrasonic axial transmission methods for bone assessment. *Ultrasound in Medicine & Biology*, 31(5), 633 - 642. doi: <http://dx.doi.org/10.1016/j.ultrasmedbio.2005.02.001>.
- Muller, M., Mitton, D., Moilanen, P., Bousson, V., Talmant, M. & Laugier, P. (2008). Prediction of bone mechanical properties using QUS and pQCT: study of the human distal radius. In *Med Eng Phys* (vol. 30, pp. 761-7). England. doi: 10.1016/j.medengphy.2007.08.006.
- Muller, M. E., Webber, C. E. & Bouxsein, M. L. (2003). Predicting the failure load of the distal radius. *Osteoporosis International*, 14(4), 345–352. doi: 10.1007/s00198-003-1380-9.
- Naili, S., Vu, M.-B., Grimal, Q., Talmant, M., Desceliers, C., Soize, C. & Haiat, G. (2010). Influence of viscoelastic and viscous absorption on ultrasonic wave propagation in cortical bone: Application to axial transmission. *The Journal of the Acoustical Society of America*, 127(4), 2622-2634. doi: <http://dx.doi.org/10.1121/1.3353091>.
- Nguyen, V.-H. & Naili, S. (2014). Semi-analytical solution of transient plane waves transmitted through a transversely isotropic poroelastic plate immersed in fluid. *Journal of Engineering Mathematics*, 86(1), 125-138. doi: 10.1007/s10665-013-9654-5.
- Nguyen, V.-H., Tran, T. N. H. T., Sacchi, M. D., Naili, S. & Le, L. H. (2017). Computing dispersion curves of elastic/viscoelastic transversely-isotropic bone plates coupled with soft tissue and marrow using semi-analytical finite element (SAFE) method. *Computers in biology and medicine*, 87, 371—381. doi: 10.1016/j.combiomed.2017.06.001.
- Nicholson, P. H. F. (2008). Ultrasound and the biomechanical competence of bone. *IEEE Transactions on Ultrasonics, Ferroelectrics, and Frequency Control*, 55(7), 1539-1545. doi: 10.1109/TUFFC.2008.830.
- Nicholson, P. H. F., Moilanen, P., Kärkkäinen, T., Timonen, J. & Cheng, S. (2002). Guided ultrasonic waves in long bones: modelling, experiment and in vivo application. *Physiological Measurement*, 23(4), 755.
- Oyen, J., Rohde, G. E., Hochberg, M., Johnsen, V. & Haugeberg, G. (2010). Low-energy distal radius fractures in middle-aged and elderly women-seasonal variations, prevalence of osteoporosis, and associates with fractures. *Osteoporos Int*, 21(7), 1247-55. doi: 10.1007/s00198-009-1065-0.
- Padegimas, E. M. & Osei, D. A. (2013). Evaluation and treatment of osteoporotic distal radius fracture in the elderly patient. *Current Reviews in Musculoskeletal Medicine*, 6(1), 41–46. doi: 10.1007/s12178-012-9153-8.
- Papaioannou, A., Giangregorio, L., Kvern, B., Boulos, P., Ioannidis, G. & Adachi, J. (2004). The osteoporosis care gap in Canada. *BMC Musculoskeletal Disorders*, 5(1), 1. doi: 10.1186/1471-2474-5-11.

- Pavlakovic, B. & Lowe, M. (1999). A General Purpose Approach to Calculating the Longitudinal and Flexural Modes of Multi-Layered, Embedded, Transversely Isotropic Cylinders. In Thompson, D. O. & Chimenti, D. E. (Eds.), *Review of Progress in Quantitative Non-destructive Evaluation: Volume 18A–18B* (pp. 239-246). Boston, MA: Springer US.
- Pavlakovic, B., Lowe, M., Alleyne, D. & Cawley, P. (1997). Disperse: A General Purpose Program for Creating Dispersion Curves. 185–192. doi: 10.1007/978-1-4615-5947-4_24.
- Pereira, D., Haiat, G., Fernandes, J. & Belanger, P. (2017). Simulation of acoustic guided wave propagation in cortical bone using a semi-analytical finite element method. *The Journal of the Acoustical Society of America*, 141(4), 2538-2547. doi: 10.1121/1.4979695.
- Predoi, M. V., Castaings, M., Hosten, B. & Bacon, C. (2007). Wave propagation along transversely periodic structures. *The Journal of the Acoustical Society of America*, 121(4), 1935-1944. doi: <http://dx.doi.org/10.1121/1.2534256>.
- Protopappas, V. C., Kourtis, I. C., Kourtis, L. C., Malizos, K. N., Massalas, C. V. & Fotiadis, D. I. (2007). Three-dimensional finite element modeling of guided ultrasound wave propagation in intact and healing long bones. *The Journal of the Acoustical Society of America*, 121(6), 3907-3921. doi: <http://dx.doi.org/10.1121/1.2354067>.
- Rachner, T. D., Khosla, S. & Hofbauer, L. C. (2011). Osteoporosis: now and the future. *The Lancet*, 377(9773), 1276-1287. doi: 10.1016/S0140-6736(10)62349-5.
- Rico, H. (1997). The Therapy of Osteoporosis and the Importance of Cortical Bone. *Calcified Tissue International*, 61(6), 431–432. doi: 10.1007/s002239900361.
- Ritzel, H., Amling, M., Pösl, M., Hahn, M. & Delling, G. (1997). The Thickness of Human Vertebral Cortical Bone and its Changes in Aging and Osteoporosis: A Histomorphometric Analysis of the Complete Spinal Column from Thirty-Seven Autopsy Specimens. *Journal of Bone and Mineral Research*, 12(1), 89–95. doi: 10.1359/jbmr.1997.12.1.89.
- Rose, J. L. (2014). *Ultrasonic Guided Waves in Solid Media*. CAMBRIDGE UNIV PR. doi: 9781107048959.
- Rozental, T. D., Deschamps, L. N., Taylor, A., Earp, B., Zurakowski, D., Day, C. S. & Bouxsein, M. L. (2013). Premenopausal Women with a Distal Radial Fracture Have Deteriorated Trabecular Bone Density and Morphology Compared with Controls without a Fracture. *The Journal of Bone & Joint Surgery*, 95(7), 633–642. doi: 10.2106/JBJS.L.00588.
- Sajjan, S. G., Barrett-Connor, E., McHorney, C. A., Miller, P. D., Sen, S. S. & Siris, E. (2012). Rib fracture as a predictor of future fractures in young and older postmenopausal women: National Osteoporosis Risk Assessment (NORA). *Osteoporos Int*, 23(3), 821-8. doi: 10.1007/s00198-011-1757-0.

- Sansalone, V., Naili, S., Bousson, V., Bergot, C., Peyrin, F., Zarka, J., Laredo, J. & Haiat, G. (2010). Determination of the heterogeneous anisotropic elastic properties of human femoral bone: From nanoscopic to organ scale. *Journal of Biomechanics*, 43(10), 1857 - 1863. doi: <http://dx.doi.org/10.1016/j.jbiomech.2010.03.034>.
- Sarvazyan, A., Tatarinov, A., Egorov, V., Airapetian, S., Kurtenok, V. & Gatt, C. J. (2009). Application of the dual-frequency ultrasonometer for osteoporosis detection. *Ultrasonics*, 49(3), 331 - 337. doi: <https://doi.org/10.1016/j.ultras.2008.10.003>.
- Sasso, M., Haiat, G., Talmant, M., Laugier, P. & Naili, S. (2008). Singular value decomposition-based wave extraction in axial transmission: application to cortical bone ultrasonic characterization. *IEEE Trans Ultrason Ferroelectr Freq Control*, 55(6), 1328-32. doi: 10.1109/tuffc.2008.795.
- Sasso, M., Talmant, M., Haiat, G., Naili, S. & Laugier, P. (2009). Analysis of the most energetic late arrival in axially transmitted signals in cortical bone. *IEEE Trans Ultrason Ferroelectr Freq Control*, 56(11), 2463-70. doi: 10.1109/tuffc.2009.1333.
- Sawka, A. M., Thabane, L., Papaioannou, A., Gafni, A., Ioannidis, G., Papadimitropoulos, E. A., Hopman, W. M., Cranney, A., Hanley, D. A., Pickard, L. & Adachi, J. D. (2005). Health-related quality of life measurements in elderly Canadians with osteoporosis compared to other chronic medical conditions: a population-based study from the Canadian Multicentre Osteoporosis Study (CaMos). *Osteoporos Int*, 16(12), 1836-40. doi: 10.1007/s00198-005-1949-6.
- Sievanen, H., Cheng, S., Ollikainen, S. & Uusi-Rasi, K. (2001). Ultrasound velocity and cortical bone characteristics in vivo. *Osteoporos Int*, 12(5), 399-405. doi: 10.1007/s001980170109.
- Stegman, M. R., Heaney, R. P., Travers-Gustafson, D. & Leist, J. (1995). Cortical ultrasound velocity as an indicator of bone status. *Osteoporosis International*, 5(5), 349-353. doi: 10.1007/BF01622257.
- Stein, E. M., Rosete, F., Young, P., Kamanda-Kosseh, M., McMahon, D. J., Luo, G., Kaufman, J. J., Shane, E. & Siffert, R. S. (2013). Clinical Assessment of the 1/3 Radius Using a New Desktop Ultrasonic Bone Densitometer. *Ultrasound in Medicine and Biology*, 39(3), 388-395. doi: 10.1016/j.ultrasmedbio.2012.09.024.
- Strom, O., Borgstrom, F., Kanis, J. A., Compston, J., Cooper, C., McCloskey, E. V. & Jonsson, B. (2011). Osteoporosis: burden, health care provision and opportunities in the EU: a report prepared in collaboration with the International Osteoporosis Foundation (IOF) and the European Federation of Pharmaceutical Industry Associations (EFPIA). *Arch Osteoporos*, 6(1-2), 59-155. doi: 10.1007/s11657-011-0060-1.
- Ta, D., Wang, W., Wang, Y., Le, L. H. & Zhou, Y. (2009). Measurement of the dispersion and attenuation of cylindrical ultrasonic guided waves in long bone. 35, 641-52. doi: 10.1016/j.ultrasmedbio.2008.10.007.

- Ta, D. A., Huang, K., Wang, W. Q., Wang, Y. Y. & Le, L. H. (2006). Identification and analysis of multimode guided waves in tibia cortical bone. 44 Suppl 1, e279-84. doi: 10.1016/j.ultras.2006.06.013.
- Talmant, M. (2011). Guided Waves in Cortical Bone. 147-179. doi: 10.1007/978-94-007-0017-8_7.
- Talmant, M., Kolta, S., Roux, C., Haguenaer, D., Vedel, I., Cassou, B., Bossy, E. & Laugier, P. (2009). In vivo performance evaluation of bi-directional ultrasonic axial transmission for cortical bone assessment. 35, 912-9. doi: 10.1016/j.ultrasmedbio.2008.12.008.
- Tarride, J. E., Hopkins, R. B., Leslie, W. D., Morin, S., Adachi, J. D., Papaioannou, A., Bessette, L., Brown, J. P. & Goeree, R. (2012). The burden of illness of osteoporosis in Canada. *Osteoporos Int*, 23(11), 2591-600. doi: 10.1007/s00198-012-1931-z.
- Tatarinov, A., Sarvazyan, N. & Sarvazyan, A. (2005). Use of multiple acoustic wave modes for assessment of long bones: Model study. *Ultrasonics*, 43(8), 672 - 680. doi: <http://dx.doi.org/10.1016/j.ultras.2005.03.004>.
- Thakare, D. R., Abid, A., Pereira, D., Fernandes, J., Belanger, P. & Rajagopal, P. (2017). Semi-analytical finite-element modeling approach for guided wave assessment of mechanical degradation in bones. *International Biomechanics*, 4(1), 17-27. doi: 10.1080/23335432.2017.1319295.
- Tran, T. N. H. T., Le, L. H., Nguyen, V. H., Nguyen, K. C. T. & Sacchi, M. D. (2015, Oct). Sensitivity analysis of leaky Lamb modes to the thickness and material properties of cortical bone with soft tissue: A semi-analytical finite element based simulation study. *Ultrasonics Symposium (IUS), 2015 IEEE International*, pp. 1-4. doi: 10.1109/ULTSYM.2015.0510.
- Treysse, F. & Frikha, A. (2008). A semianalytical finite element method for elastic guided waves propagating in helical structures. *The Journal of the Acoustical Society of America*, 123(5), 3841-3841. doi: <http://dx.doi.org/10.1121/1.2935645>.
- V. V. Volovoi, D. H. Hodges, V. L. B. & Sutyry, V. G. (1998). Dynamic dispersion curves for non-homogeneous, anisotropic beams with cross-sections of arbitrary geometry. *Journal of Sound and Vibration - J Sound Vib*, 215(5). doi: 10.1006/jsvi.1998.1682.
- Vallet, Q., Minonzio, J.-G., Chappard, C., Talmant, M. & Laugier, P. (2014). Towards cortical bone biomarkers using measurement of guided waves at the forearm. *Journal of Orthopaedic Translation*, 2(4), 238. doi: 10.1016/j.jot.2014.07.077.
- Vavva, M. G., Protopappas, V. C., Gergidis, L. N., Charalambopoulos, A., Fotiadis, D. I. & Polyzos, D. (2009). Velocity dispersion of guided waves propagating in a free gradient elastic plate: Application to cortical bone. *The Journal of the Acoustical Society of America*, 125(5), 3414-3427. doi: <http://dx.doi.org/10.1121/1.3110203>.

- Vu, M.-B. & Nguyen-Sy, T. (2018). On the effective anisotropic elastic properties of porous hydroxyapatite, porous collagen, and cortical bone: A homogenization scheme with percolation threshold concept. *Mathematics and Mechanics of Solids*, 1-12. doi: 10.1177/1081286518769961.
- Wilcox, P. D., Lowe, M. J. S. & Cawley, P. (2001). Mode and Transducer Selection for Long Range Lamb Wave Inspection. *Journal of Intelligent Material Systems and Structures*, 12(8), 553-565. doi: 10.1177/10453890122145348.
- Wilcox, P. D., Lowe, M. J. S. & Cawley, P. (2005). The excitation and detection of Lamb waves with planar coil electromagnetic acoustic transducers. *IEEE Transactions on Ultrasonics, Ferroelectrics, and Frequency Control*, 52(12), 2370-2383. doi: 10.1109/TUFFC.2005.1563281.
- Xu, K., Ta, D. & Wang, W. (2010). Multiridge-based analysis for separating individual modes from multimodal guided wave signals in long bones. *IEEE Trans Ultrason Ferroelectr Freq Control*, 57(11), 2480-90. doi: 10.1109/tuffc.2010.1714.
- Xu, K., Minonzio, J. G., Ta, D., Hu, B., Wang, W. & Laugier, P. (2016). Sparse SVD Method for High-Resolution Extraction of the Dispersion Curves of Ultrasonic Guided Waves. *IEEE Transactions on Ultrasonics, Ferroelectrics, and Frequency Control*, 63(10), 1514-1524. doi: 10.1109/TUFFC.2016.2592688.
- Yeh, C.-H. & Yang, C.-H. (2011). Characterization of mechanical and geometrical properties of a tube with axial and circumferential guided waves. *Ultrasonics*, 51(4), 472 - 479. doi: <https://doi.org/10.1016/j.ultras.2010.11.013>.
- ZhengGang Zhang, KaiLiang Xu, D. T. & Wang, W. (2013). Joint spectrogram segmentation and ridge-extraction method for separating multimodal guided waves in long bones. *Science China Physics, Mechanics and Astronomy*, 56(7). doi: 10.1007/s11433-013-5110-9.
- Zhu, T. Y., Griffith, J. F., Qin, L., Hung, V. W., Fong, T. N., Au, S. K., Li, M., Lam, Y. Y., Wong, C. K., Kwok, A. W., Leung, P. C., Li, E. K. & Tam, L. S. (2014). Alterations of bone density, microstructure, and strength of the distal radius in male patients with rheumatoid arthritis: a case-control study with HR-pQCT. *J Bone Miner Res*, 29(9), 2118-29. doi: 10.1002/jbmr.2221.